# Direct numerical simulations of nucleation and collapse of bubbles attached to walls

Mandeep Saini

THÈSE DE DOCTORAT
SORBONNE UNIVERSITE

École doctrale n° 391: Sciences mécaniques, acoustique, électronique et robotique de Paris

réalisée à

Institut Jean le Rond ∂'Alembert

pour obtenir le grade de

Docteur de Sorbonne Université

présentée par

Mandeep SAINI

Sujet de thèse

# Direct Numerical simulations of nucleation and collapse of bubbles attached to wall

Jury composé de

| | |
|---|---|
| Dr. Fabian DENNER | Rapporteur |
| Dr. Eric GONCALVES | Rapporteur |
| Dr. Outti SUPPONEN | Examinatrice |
| Dr. Arnaud ANTKOWIAK | Examinateur |
| Dr. Michel ARRIGONI | Invité |
| Dr. Stéphane ZALESKI | Co-encadrant |
| Dr. Daniel FUSTER | Directeur de thèse |

"Science knows no country, because knowledge belongs to humanity, and is the torch which illuminates the world"

*— Louis Pasteur*

# Acknowledgments

The world has changed 360 degrees over past three years because of corona virus pandemic, what has been constant throughout this time is the enormous support and teaching that I have received from my supervisor *Dr. Daniel Fuster*. I can not imagine myself going through this journey without his everlasting guidance and direction. I am grateful for the patience that he has kept to understand and clarify my ambiguities. *Prof. Stephané Zaleski* has been an inspiration who I have always looked up to, its his motivation and enthusiasm that has kept me going through most difficult phases. He has lead by example to inculcate the qualities of hard work, thrive for the utmost excellence and unparalleled quest for knowledge and understanding science. I learned immeasurably from *Prof. Detlef Lohse* on how to think creatively, clearly and have fun while doing science. His conviction has given me immense confidence in myself and skills that I have acquired over the due course of my PhD. I am indebted to *Dr. Michel Arrigoni* for his generous aid to host us in ENSTA Brest, and for arranging and conducting the experimental campaigns as well as allowing us to use laser facilities. I am glad to have received constant feedback and guidance from *Dr. Fabian Denner*. I am also pleased to have the opportunity to present and discuss my work to highly proficient researchers *Prof. Eric Goncalves*, *Dr. Arnaud Antkowiak* and *Dr. Outti Supponen*. I want to convey appreciation to *Dr. Ganesh Natarajan* for introducing me to CFD in his course, mentoring my masters thesis, and motivating to opt for career in research.

I sincerely acknowledge European Union (EU) for funding my PhD under the MSCA-ITN grant agreement number 813766, and the project named Ultrasound Cavitation in sOft Matter (UCOM).

I am also thankful to my colleagues and friends: *Youssef Saade* who has supported me immensely through research and discussions during my stay in Enschede, *Yash Kulkarni* for insightful discourses related to fluid mechanics and contact lines, *Ahmed Basil Kottilingal* for his kind help with code developments, *Dr. Erwan Tanne* and *Julien Clanche* for their kind help with the experiments at Brest. *Dr. Désir André*, *Dr. Leonardo Chirco*, *Dr. Cesar Pairetti*, *Dr. Sagar Pal*, *Dr. Adrien Rohfritsch* and *Dr. Augustin Guibaud* have also helped me at different stages. I am also glad to have received administrative help for *Simona Otarasanu* and *Evelyne Mignon*, and technical support from informaticians *Pascal Ray* and *Patrick Cao*. I have also been fortunate to have joy and emotional support from *Jyoti*, *Balveer Singh*, *Prachi Shrivastava* and *Anambar Chaudhary*. Last but not least, I want to express my extreme gratitude for my family for their enduring belief, implacable encouragement and unprecedented love.

# Resume

Cavitation bubbles appear in numerous applications among several disciplines, yet the interaction between the cavitaiton bubbles and their surroundings is not well understood. In this work, we comprehensively study the process of nucleation and collapse of bubbles in contact with rigid wall that leads to complex interaction between the bubble, the wall and the surrounding media. We focus on the heterogeneous nucleation where the bubbles are known to generate from the small unstable gas nuclei that can be trapped in the solid impurities. We assume that these nuclei have spherical cap shape and examine their stability using the quasi-static theory in the limiting conditions of contact line motion i.e. pinning and free movement. We show that the stability of bubbles depend on the behavior of contact line and that the pinning effect stabilizes the gas nuclei. We use direct numerical simulations with a Navier-slip model to study the dynamics of nucleating bubbles and to resolve the visco-capillary effects close to the wall. The numerical simulations reveal the appearance of a microlayer that grows at an asymptotic value in the limit of large capillary numbers (of order one) for Ohnesorge numbers much smaller than unity. In the second part, we focus on the characterization of the collapse of spherical cap shaped bubbles. We show that the dynamic response of a spherical cap bubble in contact with a rigid wall depends on the effective contact angle at the instant prior to collapse. This parameter allows us to discriminate between two regimes in which the mechanisms of interaction between the collapsing bubble and its surrounding medium differ markedly: When the contact angle is smaller than 90 degrees a classical jet directed towards the wall is observed whereas if the initial contact angle is larger than 90 degrees an annular re-entrant jet parallel to the wall appears. We show that this change of behavior can be explained using the impulse potential flow theory for small times which shows the presence of a singularity on the initial acceleration of contact line when the contact angle is larger than 90 degrees. In some circumstances, numerical and experimental results show that the collapse of flat bubbles can eventually lead to the formation of a vortex ring that unexpectedly induces long-range effects. We use the energy conservation equation to characterize the kinetic energy of liquid jets formed during the non-spherical collapse of bubbles in contact with the rigid wall. Depending upon the bubble shape, some amount of this kinetic energy can remain residual in the liquid bulk at the instant of minimum volume penalizing the maximum gas pressures at this instant. We show that this penalization effect becomes increasingly important as the pressure difference driving the collapse increases. In the last part, we study the problem of multiple cavitation bubbles nucleating and collapsing in the contact with a rigid wall. We discuss the asymmetry caused by the pressure pulse as a function of effective speed of sound in the liquid phase. We hypothesize that the asymmetry is caused by the finite speed of sound effects which result from the fact that the tiny bubble fragments remain inside the liquid bulk in the subsequent cavitation experiments. These results can find direct application in the control and optimization of techniques based on the cavitation as well as understanding of naturally occurring phenomenon where cavitation bubbles appear.

# Resumé

Les bulles issues du phénomène de cavitation apparaissent dans d'innombrables applications dans de différents domaines. Toutefois, leur interaction avec le milieu environnant n'est pas bien comprise. Dans ce travail, nous étudions de manière approfondie le processus de nucléation et d'effondrement des bulles en contact avec une paroi rigide, conduisant à une interaction complexe entre la bulle, la paroi et le milieu environnant. Nous nous concentrons sur la nucléation hétérogène. Dans ce processus, les bulles sont générées à partir de petites poches instables de gaz potentiellement piégées dans les impuretés du solide. Nous supposons que ces poches ont la forme d'une calotte sphérique et nous examinons leur stabilité grâce à la théorie quasi-statique dans le cadre de la dynamique de la ligne de contact, à savoir le pincement et le libre déplacement. Nous montrons que la stabilité des bulles dépend du comportement de la ligne triple de contact et que le pincement stabilise les poches de gaz. Nous utilisons des simulations numériques directes pour étudier la dynamique de la nucléation des bulles et pour déterminer les effets visco-capillaires au voisinage de la paroi. Les simulations numériques révèlent que la croissance de cette dernière tend vers une valeur asymptotique pour de grands nombres capillaires lorsque le nombre d'Ohnesorge est plus petit que l'unité. Il est intéressant de noter que la valeur asymptotique de la vitesse adimensionnelle de la ligne de contact varie avec le cube de l'angle de contact, ce qui est en accord avec la théorie de Cox-Voinov. Dans la partie suivante, nous concentrons sur le phénomène d'effondrement des bulles en forme de calotte sphérique. Nous montrons que la réponse dynamique d'une bulle en forme de calotte sphérique en contact avec une paroi rigide dépend de l'angle de contact effectif à l'instant précédant l'effondrement. Ce paramètre nous permet de distinguer deux régimes dans lesquels les mécanismes d'interaction entre la bulle qui s'effondre et le milieu qui l'entoure sont très différents : lorsque l'angle de contact est inférieur à 90 degrés, un jet classique dirigé vers la paroi est observé tandis que pour un angle de contact initial supérieur à 90 degrés, un jet annulaire rentrant parallèle à la paroi apparaît. Nous montrons que ce changement de comportement peut être expliqué en utilisant la théorie de l'écoulement potentiel impulsionnel pour les petits temps qui montre la présence d'une singularité lors de l'accélération initiale de la ligne de contact quand l'angle de contact est supérieur à 90 degrés. Dans certains cas, les résultats numériques et expérimentaux révèlent que l'effondrement des bulles plates peut éventuellement mener à la formation d'un anneau tourbillonnaire qui induit de manière inattendue des effets à longue distance. Nous utilisons l'équation de conservation de l'énergie pour caractériser l'énergie cinétique des jets de liquide formés pendant l'effondrement de bulles non-sphériques en contact avec la paroi rigide. Selon la forme de la bulle, une petite quantité d'énergie cinétique demeure dans la phase liquide lorsqu'on atteint le volume minimal, et pénalise donc la pression maximale de gaz à cet instant. Dans la dernière partie, nous étudions le problème de la nucléation et de l'effondrement de multiples bulles de cavitation au contact d'une paroi rigide. Nous discutons de l'asymétrie résultant de l'impulsion de pression en fonction de la vitesse du son dans la phase liquide. Nous supposons que cette asymétrie est causée par la vitesse finie des effets sonores, qui résulte du fait que de minuscules bulles restent à l'intérieur de la phase liquide lors des successives expériences de cavitation.

# Contents


1 Introduction 1
- 1.1 Relevance of bubble dynamics and cavitation . . . 1
- 1.2 Motivation and background of current study . . . 3
  - 1.2.1 Ultrasound cavitation . . . 3
  - 1.2.2 Laser generated bubbles . . . 4
  - 1.2.3 Understanding of cavitation and current gaps . . . 6
- 1.3 Manuscript outline . . . 8
- 1.4 Journals and conferences . . . 10

2 Governing equations and Numerical methods 11
- 2.1 Governing equations . . . 11
- 2.2 Numerical method . . . 13
  - 2.2.1 Interface representation . . . 13
  - 2.2.2 Advection step . . . 13
  - 2.2.3 Prediction step . . . 14
  - 2.2.4 Projection step . . . 15
- 2.3 Numerical model for moving contact lines . . . 19
- 2.4 Energy conservation for a gas bubble in a weakly compressible liquid . . . 21
- 2.5 Relevant non-dimensional numbers . . . 24

3 Heterogeneous bubble nucleation 27
- 3.1 Nucleation threshold . . . 28
  - 3.1.1 Theoretical predictions of the bubble nucleation threshold . . . 28
  - 3.1.2 Numerical predictions of the nucleation threshold . . . 31
  - 3.1.3 Finite pulse duration effects . . . 36
- 3.2 Unstable bubble growth and microlayer formation . . . 38
  - 3.2.1 Theoretical description of microlayer . . . 39
  - 3.2.2 Direct numerical simulations . . . 41
  - 3.2.3 Structure of Microlayer . . . 49

4 Bubble collapse 53
- 4.1 Problem setup . . . 54
- 4.2 Short time dynamics . . . 54
  - 4.2.1 Potential flow solution . . . 55
  - 4.2.2 Viscous correction . . . 59
- 4.3 Long time dynamics . . . 61
  - 4.3.1 Peak gas pressures and jetting during the collapse of a bubble . . . 62

4.3.2 Experimental comparison . . . . . 68
4.3.3 Finite Reynolds number effects . . . . . 71

5 Multibubble cavitation 73
5.1 Setup . . . . . 75
5.2 Bubble pair . . . . . 76
5.2.1 Description of Asymmetric behavior . . . . . 77
5.2.2 Effect of effective speed of sound . . . . . 77
5.2.3 Effect of the size of nuclei . . . . . 81
5.3 Multiple bubbles setup . . . . . 82
5.3.1 Five bubbles in a line . . . . . 82
5.3.2 Cluster of bubbles . . . . . 83

6 Conclusions and future perspectives 87

Bibliography 91

# List of Figures


1.1 The range of scales of bubble size and diverse fields where bubble dynamics and cavitation find applications. Some examples of bubble shapes at different scales is also shown in the bottom row taken from references [1, 7, 8] . . . . . 2

1.2 The figures are reproduced from the study of Bremond et. al. [55] $(a)$ The front and top view of a typical cavitation bubble nucleating from the pit and collapsing in the contact with a rigid wall are shown in upper and lower row respectively. $(b)$ The pressure waveform generated from the piezoelectric transducer averaged over 50 cycles. $(c)$ The bubble response represented by the equivalent bubble radius obtained from experiments and from Rayleigh–Plesset (RP) model . . . 4

1.3 The experimental images of bubble collapse taken from Suponnen et. al. [1], the scale given in each figure is equal to 1mm length. $(a)$ The momentum focusing in to high speed liquid jets that are generated during the non-spherical bubble collapse. $(b)$ The experimental visualization of the emission of shock waves that are generated during the bubble collapse. . . . . 5

1.4 The top view of bubbles nucleating in the liquid bath due to the laser impact on the opposite side of aluminum plate obtained using setup shown in reference [66]. 6

1.5 The bubble size and driving pressure considered in different chapters . . . . . 9

2.1 The algorithm for all-Mach solver . . . . . 18

2.2 $(a)$ The radius of curvature at end of simulation for different angles of contact where analytical results are obtained from Laplace equation and mass conservation $(b)$ The interface shape at end of simulation for various angles of contact . 20

2.3 The control volumes for gas and liquid considered at a particular instant to write the energy conservation principle. . . . . 21

2.4 The setup for studying bubble dynamic problems, at equilibrium position $p_\infty = p_{L,0}$, for expansion $p_\infty < p_{L,0}$ and for collapse $p_\infty > p_{L,0}$ . . . . . 25

3.1 The schematic diagram for the different scenario of how a nucleus can respond to the ultrasound pressure drop. These three cases will discussed in detail in this chapter. . . . . 27

3.2 The non-dimensional Laplace pressure and second derivative in non-dimensional potential energy w.r.t bubble volume is plotted against radius of bubble for quasi-static expansion of a spherical bubble and representative case of $1/\sigma^* = 0.32$. . 29

3.3 The critical pressure drop required for unstable growth of spherical cap shaped air bubbles in contact with rigid wall and in water at normal temperature and pressure conditions. The critical pressure drop predicted from minima of equation 3.10 (colormap) is shown for several bubble shapes and size are characterized by radius of curvature $R_{c,0}$ and contact angle $\alpha_0$. An isobar for $p_{cr} = -2$MPa is also shown with the black curve. The bubbles in panel $(a)$ are subjected to free slip boundary condition whereas in panel $(b)$ are subjected to pinning boundary condition for motion of contact line. . . . . 31

3.4 $(a)$ The numerical setup for the single bubble expansion liquid bulk $(b)$ Radius evolution for spherical bubble exposed to pressure slightly more than and less than the critical pressure in the case $1/\sigma^* = 0.32$ $(c)$ The numerical prediction of critical pressure drop for transition form stable to unstable behavior shown for different bubble sizes characterized by $\sigma^*$ . . . . . 33

3.5 $(a)$ The numerical setup for simulations for expansion of bubbles attached to wall. $(b)$ The evolution of dimensionless bubble volume for representative bubble with $\alpha = 150^\circ$ and $R_{c,0}\sigma/p_{L,0} = 1.4$ for different pressure drops compared the critical pressure drop $p_\infty/p_{cr}$ shown in legend. $(c)$ The numerical predictions of critical pressure drop for bubbles with different contact angles, the unstable bubbles are shown with red points where as the stable ones with green, black dash line corresponds to critical pressure drop predicted from equation 3.10. 34

3.6 $(a)$ Isobars for critical pressure drop of $p_{cr}/p_{L,0} = -0.86$ for bubbles subjected to the two limiting boundary conditions for motion of contact line, the red point is chosen as representative of intermediate region where the stability of bubble depends on the boundary condition. $(b)$ The DNS results for evolution of bubble volume for a bubble from intermediate region (red point in figure 3.6$a$) subjected critical pressure drop and the limiting boundary conditions. . . . . 35

3.7 The comparison is drawn between same bubble $(p_{L.0}R_{c,0}/\sigma = 1.4, \alpha = 2\pi/3)$ subjected to same pressure drop but different limiting boundary conditions. $(a)$ The evolution of Laplace pressure with the bubble volume obtained from the DNS shown with the thick lines and the dashed line is obtained from the quasi-static theory. $(b)$ The interface contours obtained from DNS at various instances of time where left half is the case of pinning boundary condition and right half is the case of free slip boundary condition. . . . . 35

3.8 $(a)$ Setup for studying bubble expansion from Gaussian pressure perturbation $(b)$ Max radius plotted against $F_R$ for several pressure amplitude for different $p_\infty/p_{cr}$ shown with the colormap $(c)$ Bubble population active for cavitation depending upon the initial bubble radius and the two limiting criterion posed by surface tension forces (equation 3.5) and finite pulse duration. . . . . 37

3.9 The figure shows the bubble shape in the regime where the microlayer forms during the bubble expansion, zoom in the intermediate scale is shown in the bottom right panel and zoomed in view of the smallest scale is also shown in bottom left panel. . . . . 39

3.10 Schematic illustration of the interface close to wall approximated as the thin film often used to model the dynamics of interface at the intermediate length scale. . 39

3.11 Results for bubble expansion in the case of $\alpha = 90°$,$Oh = 0.037$,$\lambda_{num}/R_{c,0} = 0.01$ and varying *Ca*. $(a)$ The evolution of non-dimensional equivalent bubble radius $R = (V/V_0)^{1/3}$ for different capillary numbers (color-map). $(b)$ The interface contours for different non-dimensional times shown with the color-map $(c)$ The interface shapes re-scaled with the characteristic velocity $U_c t/R_{c,0}$ in the normal direction . . . . . 42

3.12 The definition of relevant points on the bubble interface that are used for describing the bubble expansion and formation of microlayer . . . . . 43

3.13 Results for bubble expansion in the case of $\alpha = 90°$,$Oh = 0.037$,$\lambda_{num}/R_{c,0} = 0.01$ and varying *Ca*. This figure characterize the motion of the interface using three points defined in figure 3.12. $(a)$ The velocity of axial point defined as $\frac{1}{U_c}\frac{dh}{dt}$ $(b)$ The velocity of contact point defined as $\frac{1}{U_c}\frac{dc}{dt}$ $(c)$ The velocity of the point corresponding to $c_{max}$ defined as $\frac{1}{U_c}\frac{dc_{max}}{dt}$ . . . . . 43

3.14 Results for bubble expansion in the case of $\alpha = 90°$,$Oh = 0.037$,$\lambda_{num}/R_{c,0} = 0.01$ and varying *Ca*. The zoomed-in view of the evolution of bubble interface close to the wall, each panel corresponds to different capillary numbers *Ca* represented with the colormap. In each of the panel, the interface evolves from left to right and each lines corresponds to different non-dimensional time. The non-dimensional time $tU_c/R_{c,0}$ interval between the curves in each panel is $0.408$ therefore contours in each panel are shown at $tU_c/R_{c,0} \in \{0, 0.41, 0.82, 1.22, 1.63, 2.04, 2.44\}$ . . . . . 44

3.15 Results for bubble expansion in the case of $\alpha = 90°$,$Oh = 0.037$,$\lambda_{num}/R_{c,0} = 0.01$ and varying *Ca*. $(a)$ The non-dimensional velocity of three interface points defined in figure 3.12 at non-dimensional time $tU_c/R_c = 1.22$ is shown for different values of capillary numbers. $(b)$ The evolution contact line capillary number $Ca(u_{CL}) = \frac{\mu u_{CL}}{\sigma}$ for different values of capillary numbers (color-map). $(c)$ Local capillary numbers for three interface points defined in figure 3.12 at non-dimensional time $tU_c/R_c = 1.22$ is shown for different values of global capillary numbers. The dotted line is $Ca = Ca_{local}$ and the solid is fitting using harmonic averaging i.e. $\frac{1}{\frac{1}{Ca}+\frac{1}{Ca_\infty}}$ . . . . . 45

3.16 Results for bubble expansion in the case of $\alpha = 90°$,$Oh = 0.037$,$\lambda_{num}/R_{c,0} = 0.01$ and varying *Ca*. The minimum value of apparent angle defined as the angle between the tangent to the interface and the radial axis $r$ at a given microlayer thickness $(h_f)$. . . . . 46

3.17 Results for bubble expansion in the case of $Oh = 0.037$,$\lambda_{num}/R_{c,0} = 0.01$ and varying *Ca* as well as $\alpha$. The effect of contact angle on the asymptotic growth regime of microlayer $(a)$ The numerical results (circles) for contact line capillary number $Ca(u_{CL})$ as a function of global capillary number *Ca*, the dashed lines show the fitting curves obtained using $Ca = \frac{1}{\frac{1}{Ca}+\frac{1}{Ca_\infty}}$ for different contact angle boundary conditions (color-map). $(b)$ The fitting parameter $Ca_\infty$ that represents the global capillary number for asymptotic microlayer growth is plotted as a function of $\alpha$, along with the fitted curve $\propto \alpha^3$ (dashed line). . . . . 47

3.18 Results for bubble expansion in the case of $\alpha = 90°$,$Ca = 0.57$,$\lambda_{num}\rho\sigma/\mu^2 = 0.00012$ and varying $Oh$. The effect of Ohnesorge number on the microlayer formation at constant $Ca$. $(a)$ The velocity of three important interfacial points is plotted as a function of Ohnesorge number. $(b)$ The evolution of minimum interface slope is shown for different Ohnesorge numbers (colormap) . . . . . 48

3.19 The non-dimensional velocity difference between interface point $c_m$ and the contact line is shown in the phase map of $Oh$-$Ca$ plane. The shaded region corresponds to the stable region as predicted by equation 3.21, the solid color lines are isolines for different values $(u_{c_m} - u_{CL})/U_c$ calculated from the numerically obtained values (points). The bubble evolution is also shown for three representation cases marked as $(a)$,$(b)$ and $(c)$ with the color code representing the bubble interface at different times. . . . . 49

3.20 Results for for bubble expansion in the case of $\alpha = 90°$,$Oh = 0.037$, $Ca = 1.4$ and varying $\lambda_{num}/R_{c,0}$. The effect of slip length on the microlayer formation regime. $(a)$ the velocity of three important interfacial points is plotted as a function of non-dimensional slip-length. $(b)$ The evolution of the minimum interface slope for various slip-length (color-map) . . . . . 50

3.21 Results for for bubble expansion in the case of $\alpha = 90°$,$Oh = 0.0327$,$\lambda_{num}/R_{c,0} = 0.01$ and $Ca = 1.4$. The interface shape obtained from the direct numerical simulations (black cross) and the models proposed for interface shape are also shown with thick lines in $(a)$ linear scale $(b)$ log-log scale. . . . . 50

4.1 The collapse dynamics of a spherical cap bubble in contact with rigid wall explained in terms of 3 time scale $(a)$ the short time scale which is much smaller than the bubble collapse time scales $(b)$ The time scales comparable with the bubble collapse time scale $(c)$ The time scales much larger than the collapse time scales 53

4.2 The setup for the problem where the bubble shape is spherical cap. The coordinate system used in describing the flow field i.e. $(r_w, \theta_w)$ centered at wall and $(r_s, \theta_s)$ centered at the contact point are also shown. . . . . 55

4.3 $(a)$ Isocontours of the magnitude acceleration for bubble with contact angle $\alpha = 2\pi/3$: The left half isocontours are obtained from free surface model and in the right half isocontours obtained from DNS at infinite Reynolds. $(b)$ Non-dimensional acceleration magnitude along the wall obtained for same case using the free surface model. . . . . 56

4.4 $(a)$ Non-dimensional acceleration magnitude, $|\mathbf{a}_I|/a_0$ along the interface parameterized using the angle $\theta_w$ (measured in the counter-clockwise direction from the point of contact of wall and the axis of symmetry) for $\alpha = \frac{\pi}{3}, \frac{\pi}{2}, \frac{2}{3}\pi, \frac{3}{4}\pi$. Dots represent the numerical solution from free surface model and the thick lines are predictions using equation 4.5 evaluated at the interface. $(b)$ Exponent $b_0$ and coefficient $C_0$ obtained from fitting the pressure gradient obtained from the free surface model along the wall for different $\alpha$. $(c)$ Non-dimensional averaged interface acceleration magnitude as a function of the contact angle using different methods: analytical expression given by equation 4.7 (blue line), the solution from the free surface model (yellow line), the DNS solution of the Euler equations (black crosses), and the DNS solution of the Navier–Stokes solver for $Re = 100$ (red crosses). . . . . 57

4.5 $(a)$ The numerical setup for DNS $(b)$ Results from the DNS for $\alpha = 2\pi/3$ and $Re = 100$. Time averaged interface acceleration in direction parallel to the wall, $a_{r,I} = u_{r,I}/t$, as a function of the distance from the wall at 5 different times (in color where $tU_c/R_{c,0} \in [7.27 \cdot 10^{-5}, 3.6 \cdot 10^{-4}]$). For reference we include the potential flow solution given by equation 4.5 evaluated at the interface (solid black line). The inset represents a zoom into the viscous boundary layer generated close to the wall. . . . . 59

4.6 The grid convergence of viscous solution $(a)$ The evolution of velocity of contact line is plotted for different grid-size. $(b)$ The evolution of jet velocity is plotted for various grid size. . . . . 60

4.7 $(a)$ Evolution of jet velocity for different contact angles from (dots) DNS and (solid lines) fitting using Eq. 4.8. $(b)$ Exponent $q$ from DNS fitting and predictions of Eq. 4.9. . . . . 61

4.8 we show the vorticity in color map and velocity vectors obtained from DNS after short time short time ($\frac{tU_c}{R_c} = 0.11$) for $Re = 1000$ and $(a)$ $\alpha = 2\pi/3$ and $(b)$ $\alpha = 5\pi/12$. . . . . 63

4.9 The grid convergence is demonstrated for a representative case $p_\infty/p_{g,0} = 8$, $Re = \infty$, $We = \infty$ $(a)$ Non-dimensional kinetic energy $(b)$ Average bubble pressure $(c)$ The bubble shapes for different driving pressures and smallest possible grid size as obtained from DNS using setup from figure 4.5$a$. . . . . 64

4.10 The DNS results for collapse of bubbles with different $\alpha$ and for $p_\infty/p_{g,0} = 8$,$Re = \infty$, $We = \infty$. The top row shows the evolution of bubble shapes contours for $(a)$ $\alpha = 0$ $(b)$ $\alpha = \pi/3$ $(c)$ $\alpha = \pi/2$ $(d)$ $\alpha = 2/3\pi$. The snapshot of bubble at the instant of minimum volume is given in bottom row where the interface is shown with black curve ,the kinetic energy in liquid phase is shown with linear color map in right half and the velocity vectors in left half for $(e)$ $\alpha = 0$ $(f)$ $\alpha = \pi/3$ $(g)$ $\alpha = \pi/3$ $(h)$ $\alpha = 2/3\pi$ . . . . . 65

4.11 The DNS results for $p_\infty/p_{g,0} = 8$,$Re = \infty$, $We = \infty$ and varying contact angle. $(a)$ Non dimensional equivalent radius of the bubble. $(b)$ The non-dimensional collapse time is plotted as function of $\alpha$. $(c)$ The temporal evolution of the dimensionless kinetic energy integrated over liquid control volume. $(d)$ The residual kinetic energy at the instant of minimum volume for different $\alpha$. 66

4.12 The DNS results for $p_\infty/p_{g,0} = 8$,$Re = \infty$, $We = \infty$ and varying contact angle. $(a)$ The evolution of kinetic energy with the bubble volume is shown along with equation 4.10 taking $\Phi_D = 0$. $(b)$ The maximum pressure is plotted for various values of $\alpha$ as obtained from DNS (red curve), we also the solution of equation 4.12 assuming $\Phi_D = 0$, the blue curve is obtained by calculating the integral of kinetic energy form DNS and black line is obtained assuming $E_{k,R} = 0$. 67

4.13 The DNS results for varying $p_\infty/p_{g,0} = 8$,$Re = \infty$, $We = \infty$ and different contact angle. $(a)$ The residual liquid kinetic energy at the instant of minimum volume is plotted for various $\alpha$ (colormap) and $p_\infty/p_{g,0}$. $(b)$ The maximum pressure is plotted as a function of $p_\infty/p_{g,0}$ for different alpha (colormap), the black curve corresponds to equation 4.12 assuming $\Phi_D = 0$, $E_{k,R} = 0$ . . . . 68

4.14 Experimental setup used to create flat bubbles. . . . . 69

4.15 The snapshots of bubble shape are shown for the two representative cases, the numerical bubble shapes shown with red curves are overlaid at same times and scaled to same length as in experiments. $(a)$ Case where $\alpha > \pi/2$, each snapshots are taken every $0.1$ms $(b)$ Case where $\alpha < \pi/2$, each snapshots are taken every $0.125$ms. . . . . 70

4.16 $(a)$ Bubble interface in black curve and the vorticity field in the colormap as obtained from DNS is shown at (consecutively from left to right) $\frac{tU_c}{R_c} = 0, 0.19, 0.3, 0.81, 1.00, 1.45, 1.95, 4.90$. The results are plotted for $\alpha = 2\pi/3$ and $Re = \infty$ $(b)$ The visualization of liquid flow field obtained by adding dye at the bottom of tank resulting from collapse of bubble is shown at every 2.5ms. $(c)$ Interaction of vortex ring with the free surface as observed from the experiments. . . . . 71

4.17 The DNS results for $p_\infty/p_{g,0} = 10$, varying $Re$, varying $We$ and varying contact angle. $(a)$ Peak of the non-dimensional velocity as a function of Reynolds number for an air bubble at $p_0 = 0.1$ atm collapsing in water at atmospheric pressure. $(b)$ Interface contours as a function of the Reynolds number at the instant of minimum radius. $(c)$ The critical Reynolds for appearance of jet opposite to the wall is shown as a function of contact angle, (red squares) are the points where the jet appear opposite to the wall and (green circles) corresponds to the points where the jet parallel to wall does not appear. . . . . 72

5.1 The top view of multiple cavitation bubbles nucleating from pits ($4\mu$m diameter) and collapsing in contact with the rigid wall. $(a)$ A pair of bubbles nucleating from two pits separated by a distance of $200\mu$m and $400\mu$m is shown in left and right panel respectively. The snapshots from top to bottom rows in both columns belong subsequently to time, $t(\mu s) \in \{5, 8, 13, 17, 22, 23, 24\}$. $(b)$ A cluster of thirty seven bubbles nucleating from the pits drilled in a hexagonal arrangement having a pitch distance of $200\mu$m. The snapshots are numbered from $1 - 6$ which correspond to time, $t(\mu s) \in \{4, 9, 17, 31, 38, 44\}$. The figure is adopted from experiments of Bremond et. al. [55, 176]. . . . . 74

5.2 $(a)$ The simplified 2D schematic of the problem where the initial nuclei (shown with circles) of radius $R_{c,0}$ are separated by a distance $d$ and exposed to a 1D pressure pulse of amplitude $\Delta p = 15$MPa and a characteristic length $(L_p)$ (defined from the pulse duration $(T_p)$ given from hydrophone measurements). The direction of wave propagation is shown with red arrow. $(b)$ The 3D computational setup used in current study where the projected color-map corresponds to the initial pressure field taken from the experiments (reference [176]). A zoomed-in view of initial nuclei and the projection of the numerical grid on the bottom boundary of the domain are shown in the inset figure. . . . . 76

5.3 In this figure, we compare the numerical results for two different values of effective speed of sound i.e. $c_e = 1500$m/s and $c_e = 500\mathrm{m}/s$. The bubble pair is evolving from hemispherical nuclei of size $20\mu$m and $\lambda_{num} = 5\mu$m. In panel $(a)$ and $(b)$, the top view of the bubble shape and pressure field are displayed subsequently from top to bottom at time, $t(\mu\mathrm{s}) \in \{0, 3.5, 8.7, 13, 22, 23, 24\}$. $(a)$ When the separation distance between the nuclei equals to $200\mu$m with $c_e$ equal to 1500m/s on left and $c_e$ equal to 500m/s on right. $(b)$ When the separation distance between the nuclei equal to $400\mu$m with $c_e$ equal to 1500m/s on left and $c_e$ equal to 500m/s on right. $(c)$ A particular snapshot showing the definition of the asymmetry parameter $\mathcal{A}_y$ defined as shift of the bubble centroid in $y$ direction. $(d)$ The time-evolution of $\mathcal{A}_y$ obtained from the numerical simulations for all the cases discussed in figure 5.3 $a$ and $b$ is presented along with its comparison with experimental data, the error bars are equal to the one pixel size $(1.53\mu$m) in the experiment snapshots. . . . . 78

5.4 Effect of effective speed of sound on the asymmetry for a particular case where bubbles are evolving from a pair of hemispherical nuclei of size $20\mu$m each, separated by a distance of $200\mu$m and $\lambda_{num} = 5\mu$m. $(a)$ The time evolution of $\mathcal{A}_y$ is shown as a function of the effective speed of sound in liquid (colormap), alongside the experimentally obtained values (black crosses). The experimental bubble shapes overlaid with their numerical counterpart (red dots) at $t = 22\mu$s and $23\mu$s are illustrated in the inset figure. $(b)$ The evolution of non-dimensional $\mathcal{A}_y$ obtained using the scaling predicted from equation 5.3 for different $c_e$ (color scale) $(c)$ The max value of the asymmetry parameter (max$(\mathcal{A}_y)$) is plotted as function of the effective speed of sound along with the experimental point (black cross) where its $c_e$ is obtained by matching max$(\mathcal{A}_y)$ with the numerical data. A fit of overall data (dashed line) is also plotted to show max$(\mathcal{A}_y)$ decays like $c_e^{-1}$ as predicted by equation 5.3. $(d)$ The bubble shapes at the instant of max$(\mathcal{A}_y)$ in figure are shown for different effective speed of sound in the liquid. $(e)$ The semi-transparent bubble shapes are shown to visualize the jet generated during the last stages of collapse whose direction is highlighted with red arrows. . . . . 79

5.5 $(a)$ The decrease in the effective speed of sound for a mixture of liquid and dispersed gas is shown as function of the volume fraction of the gas phase ($\alpha_g$ given by the equation 5.4), the point obtained by matching $\mathcal{A}_y$ from experiments and numerical simulations is also drawn with black cross. $(b)$ The variation of max($\mathcal{A}_y$) with the volume fraction of the dispersed gas phase calculated from the effective speed of sound using equation 5.4. $(c)$ The tiny fragmented bubbles seen during the cavitation experiments are highlighted with red circles along with the big bubbles nucleating from the pits for the case of two pits and five pits on left and right respectively. . . . . 80

5.6 The numerical results for the particular case where the effective speed of sound is assumed to be 333m/s, $\lambda_{num} = 5\mu$m, $d = 200\mu$m and varying $R_{c,0}$. $(a)$ The time evolution of parameter $\mathcal{A}_y$ is shown for different size of initial nuclei depicted with the colormap. A zoomed-in view around the max($\mathcal{A}_y$) is also shown in the inset figure. $(b)$ The value of max($\mathcal{A}_y$) corresponding to the maximum in figure 5.6$a$ is plotted as a function of the size of the nuclei. . . . . 81

5.7 $(a)$ The top view of the five bubbles in straight line configuration, as discussed in reference [55]. The numerical results are shown in left panel, where the bubble expands from 20$\mu$m hemispherical nuclei, $\lambda_{num} = 5\mu$m and the effective speed of sound is assumed to be 667m$/s$. The experimental bubble shapes are also shown in the right panel. In both columns, each row from from top to bottom correspond to time $t(\mu s) \in \{4, 9, 15, 21, 24, 28\}$. $(b)$ The evolution of asymmetry parameter obtained from the numerical simulations (solid line) and the experiments (cross), the error bar is equal to one pixel size (i.e. $1.53\mu$m) in the experiment snapshots. . . . . 83

5.8 $(a)$ Top view of the cluster of 37 bubbles in hexagonal arrangement expanding from 20$\mu$m hemispherical nuclei,$\lambda_{num} = 5\mu$m. Assumed effective speed of sound is 1480m$/s$, isobars are shown with colormap and the panels are numbered $1-6$ at time $t(\mu s) \in \{3, 20, 28, 42, 52, 55\}$. $(b)$ The evolution of asymmetry parameter obtained from the numerical simulations (solid line) and the experiments (cross) are also shown. . . . . 84

5.9 The time evolution of parameter $\mathcal{A}_y$ is shown for varying values of numerical slip length for the bubble pair case. . . . . 85

6.1 Expansion and collapse of bubble in contact with rigid wall. The snapshots 1-8 are numbered in increasing time. . . . . 89

# List of Tables

3.1 Non-dimensional parameters used for simulations of spherical bubble expansion 32
3.2 The dimensionless parameters for predicting thresholds of bubbles attached to wall . . . . . 34

# 1 Introduction

Cavitation is an important physics problem which spans over various disciplines of engineering and science. It is the phenomenon of appearance and collapse of vapor/gas cavities in liquid phase caused by pressure changes. The collapse can consequently release an enormous amount of energy focused in a small volume, in the form of high speed liquid jets, shockwaves, rebounds of remaining vapor/gas cavities and sometimes even light emissions [1, 2, 3, 4, 5]. Cavitation is distinguished from boiling as in former the liquid is sub-cooled and the dynamics is primarily governed by liquid inertia whereas in latter the liquid is super-heated and the latent heat flow controls the bubble dynamics [6]. In this manuscript, we discuss the several fundamental aspects of bubble nucleation and collapse. Our results may find applications in several fields related to cavitation and bubble dynamics.

## 1.1 Relevance of bubble dynamics and cavitation

Bubble dynamics plays a key role in plethora of industrial, engineering, geo-physical, biomedical processes and several others. These applications extend over several scales of bubble sizes from nanometers to a few meters. Some of these processes along with the scales of bubble size are enlisted in figure 1.1. We also show the images of three bubbles of approximate size of a few microns, a few millimeters and 1 meter taken from reference [1, 7, 8]. Here, we briefly review these applications in order to indicate the relevance of studying bubble dynamics and cavitation.

Very large bubbles ($\mathcal{O} \sim$ m) are found in applications that are related to naval and defense sector. For example, the phenomenon of underwater explosion has been studied in detail for its relevance in the sub-marine warfare. In these explosions, meter sized bubbles can appear and release an enormous amount of energy during the collapse which can be extremely dangerous for offshore structures [8, 9]. Kedrinskii [10] showed in detail the interaction of collapsing bubbles and a free surface in underwater explosions. He studied the effect of the depth of explosion and the bubble size. Large bubbles are also generated to create sound signals from seismic airguns which are used for geo-physical explorations [11, 12, 13]. Another exciting application involving large bubbles is supercavitation. In supercavitation, the torpedoes and underwater bullets are designed in such a way that their body remains encapsulated inside a large bubble such that these move in air instead of water reducing the skin friction drag. This phenomenon of supercavitation is explained in detail by several researchers [14, 15, 16].

Intermediate size bubbles ($\mathcal{O} \sim$ mm) are found in industrial and engineering applications. Laser induced bubbles are often produced in this range to study the phenomenon of bubble collapse and cavitation damage. An industrial application of intermediate sized bubbles is cavitation shot peening. In this process, the collapse of bubbles near the solid surface cause mechanical stress loading and plastic deformation which results in superior surface hardness [17, 18]. Cavitation

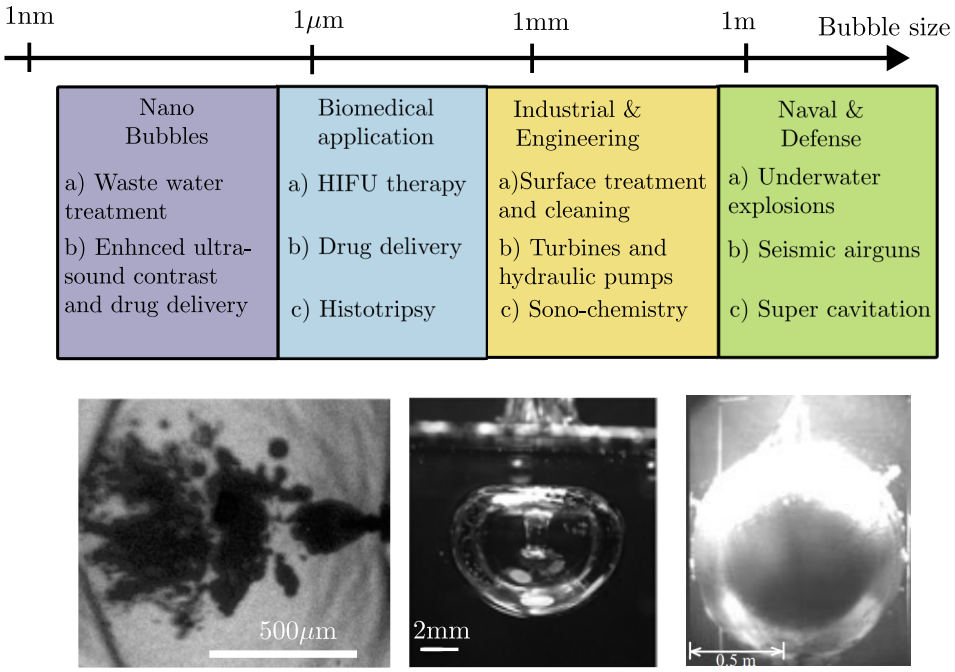


Figure 1.1: The range of scales of bubble size and diverse fields where bubble dynamics and cavitation find applications. Some examples of bubble shapes at different scales is also shown in the bottom row taken from references [1, 7, 8]

shot peening is superior to traditional shot peening methods as it results in comparatively lesser surface roughness. The bubbles collapsing in the vicinity of a wall can also derive strong shear flows which can cause local cleaning action [19, 20]. Ohl et. al. [19] measured the averaged radial velocity (responsible for cleaning action) at different stages of bubble collapse and showed that large velocities are developed only for a small time periods comparable to the bubble collapse time scales. During the collapse of these bubbles, the temperature and pressure can also momentarily reach to very high values, this high energy has been used to catalyze or alter some chemical reactions [21, 22]. Additionally, the bubbles of intermediate size appear in the low pressure regions in turbines, pumps and other flow devices which is undesirable because it enhances the erosion. This has been extensively studied experimentally [23, 24, 25] as well as numerically [26, 27, 28, 29].

Micron sized bubbles ($\mathcal{O} \sim \mu$m) have proved an ample potential in biomedical applications. Bubbles can either appear naturally in biological systems such as cracking sound in joints, traumatic brain injury (see references [30, 31]) or they are injected artificially to fulfill a specific purpose eg. drug delivery, high contrast ultrasound imaging etc (see reference [32, 33, 34]). A fascinating and challenging application of micron sized bubbles is targeted drug delivery. In this process, microbubbles of size similar to red blood cells ($7 - 8\mu$m) are generated and injected in to the blood streams. These bubbles are stabilized with lipid coatings as they will circulate in the blood vessels before reaching target location. Furthermore, these bubbles are made from the insoluble per-fluoro-carbon gases to enhance their lifetime even more. The drugs are either

incorporated inside or onto the shell of microbubbles which are sonicated at target location to administer the drugs [35]. In the same application of drug delivery, the controlled damage from the microbubble cavitation can also be used for disruption of biological membranes for targeting the drug, this operation is generally known as sonoporation [36, 37, 38]. There are several other extremely sophisticated biomedical techniques involving microbubbles for example noninvasive treatment with high intensity focussed ultrasound (HIFU) and histotrpisy for lesion of tumor cells and breaking of kidney stones, both these processes use damage caused by cavitation bubbles as an important mechanism [39, 40, 41, 42]. All these techniques are highly complicated and new frontiers are being achieved regularly with new and innovative ideas (see references [43, 44, 45]) and there is huge scope for many more.

Nanometric sized bubbles ($\mathcal{O} \sim$ nm) are most recently discovered and debated as for so small bubbles the Laplace pressures inside the bubbles is extremely high thus their existence is counter-intuitive [46, 47, 48]. Borkent et. al. [46] showed that these bubbles can be extremely stable even under enormous tensions of the order of $-6\mathrm{M}Pa$. The physics and application potential of nanobubbles are yet to be fully discovered, some studies show that they can be potentially better suited for aforementioned medical applications [45, 49, 50]. The nanobubbles have charged surfaces and these rise very slowly (owing to Brownian motion) through the liquid therefore these are shown to have superior mass transfer properties making them suitable for processes like water treatment and froth-flotation [51, 52, 53, 54].

Clearly the applications of bubbles spans over various disciplines and range of length and time scales, therefore the fundamental understanding of the behavior of cavitation bubble and its interaction with the surroundings is extremely relevant.

## 1.2 Motivation and background of current study

This research is part of the European commission project called ultrasound cavitation in soft materials abbreviated as UCOM. In this project, we focus on the interaction of bubbles formed in ultrasound cavitation with soft biological materials with a motivation to gain better control over the application concerning the biomedical fields. The project is a collaboration among 8 universities across the Europe and funding 15 PhDs divided broadly in to following work packages: Fundamental bubble collapse studies, bubble soft matter interactions and macroscopic cavitation in tissues/tissue mimicking materials. The scope of current study lies in the first work package that aims to understand the fundamentals of bubble nucleation, collapse and its interaction with the surrounding media. In this section, we introduce some bubble collapse studies available in literature and indicate the identified gaps with an intend to lay the foundation for current study.

### 1.2.1 Ultrasound cavitation

We describe the phenomenology of a single cavitation bubble by taking an example from a study of Bremond et. al. [55]. In their study, the nuclei is created artificially by drilling micron sized hole ($4\mu$m diameter) in a silicon plate, this plate is then submerged in to a large water tank and sonicated using a piezoelectric transducer (typically used in biomedical applications). A pressure signal recorded by hydrophone in their experiments is shown in figure 1.2*b*. The response of the air trapped in nuclei to the pressure pulse (captured by high speed imaging) is shown in figure 1.2*a*

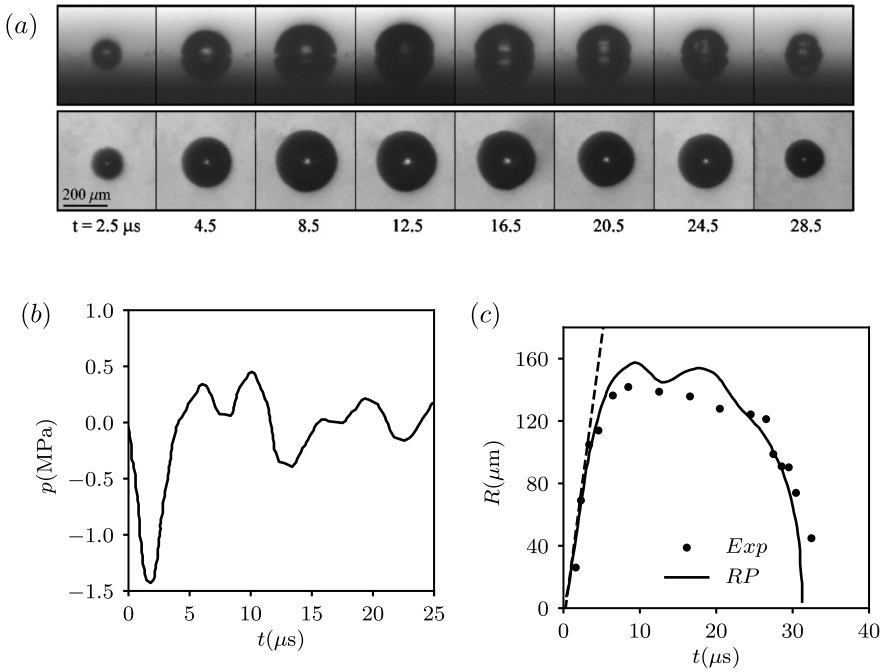


Figure 1.2: The figures are reproduced from the study of Bremond et. al. [55] $(a)$ The front and top view of a typical cavitation bubble nucleating from the pit and collapsing in the contact with a rigid wall are shown in upper and lower row respectively. $(b)$ The pressure waveform generated from the piezoelectric transducer averaged over 50 cycles. $(c)$ The bubble response represented by the equivalent bubble radius obtained from experiments and from Rayleigh–Plesset (RP) model

and summarized as following: As the air trapped in the nuclei experiences the drop in pressure, it undergoes a rapid expansion and reaches a maximum radius. This process is controlled by initial nuclei size and the amplitude and frequency of the pressure pulse. This first part of bubble cycle i.e. expansion from nuclei to maximum radius is referred to as nucleation in the current study. As the bubble reaches maximum volume a spatially varying pressure field is developed around the bubble as the pressure far from the bubble is at ambient value whereas inside the bubble the pressure is comparatively lower, therefore the gas inside the bubble undergoes a rapid compression until it reaches a minimum volume. The parameters influencing this process are the pressure inside the gas bubble at the instant of maximum volume, bubble size and the ambient pressure. This part of (i.e. rapid compression from maximum volume to minimum volume) bubble cycle is referred to as the collapse stage in the current study. This is followed by less stronger expansion and compression cycle until all the energy in bubble is dissipated and the thermodynamic equilibrium is achieved.

### 1.2.2 Laser generated bubbles

The collapse of bubbles is often studied unconnected from the nucleation by using the lasers to produce bubbles [1, 56, 57, 58, 59]. This process is related to several complicated mechanisms and a variety of energy transfers processes [60]. The mechanisms associated with the collapse of such

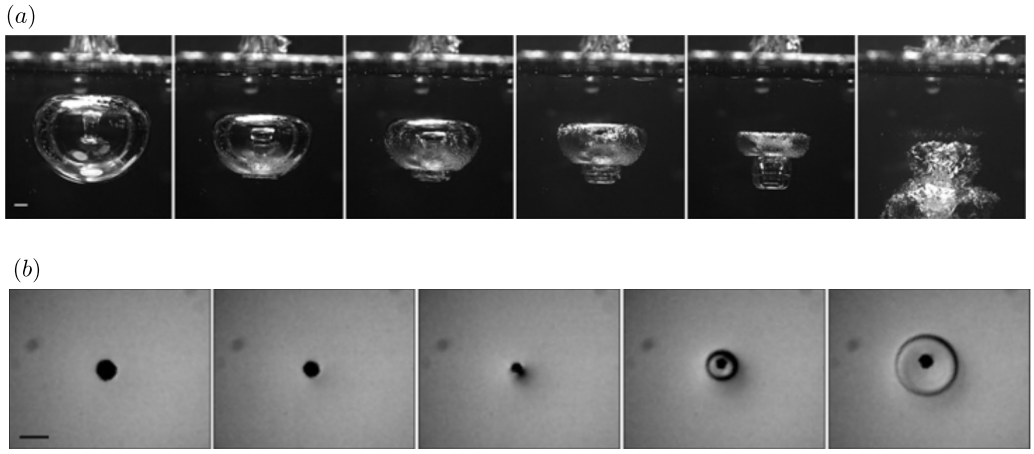


Figure 1.3: The experimental images of bubble collapse taken from Suponnen et. al. [1], the scale given in each figure is equal to 1mm length. $(a)$ The momentum focusing in to high speed liquid jets that are generated during the non-spherical bubble collapse. $(b)$ The experimental visualization of the emission of shock waves that are generated during the bubble collapse.

bubbles is illustrated in the figure 1.3 with images taken from the study of Supponen et. al. [2]. During the collapse a bubble undergoes complex non-spherical topological changes and generate liquid jets where the liquid momentum is focused, thus a part of the bubble energy is converted in to the kinetic energy of liquid. Another part of bubble energy is converted in to the internal energy of surrounding liquid in the form of shock waves generated during the collapse. The figure 1.3$b$ shows the shock-wave generating from the spherical collapse (see references [61, 62]). However, the waves generated from the collapse of non-spherical bubbles is not understood yet because an intricate pattern of shock waves and acoustic waves can occur as shown by Supponen et. al. [56]. During the intense collapse the temperature inside the bubbles rises to very large values being responsible for the light emission as comprehensively discussed and reviewed in references [3, 4, 63, 64]. Some of the bubble energy is also converted into chemical, mechanical and thermal energy. Finally, the leftover energy results into the next expansion and collapse cycle referred to as rebound cycle [65].

In the current study, we present some experimental results from our collaboration with Dr. Michel Arrigoni's group in ENSTA Brest. The setup used is similar to Bourguille et. al. [66]. This is an alternative approach to generate the bubbles from a laser, where an aluminum plate is kept at the bottom of the liquid tank and the laser is impacts the outer face of the plate instead of a direct focusing in to the liquid similar to the classical studies. The laser impact induces the cavitation on the opposite face of the aluminum plate inside the liquid bath which is recorded using the high speed imaging. The details of the experimental procedure and the setup will be shown in chapter 4. In figure 1.4, we show the top view of bubbles in one of these experiments at different instants of time. A number of bubbles nucleate in contact with the aluminum plate, these bubble merge and coalesce with each other to form a big bubble as seen in snapshot 3, which then collapses in contact with the rigid wall. The collapse is again accompanied with the complicated processes described above. The mechanism and hydrodynamics of the generation of these bubbles is yet

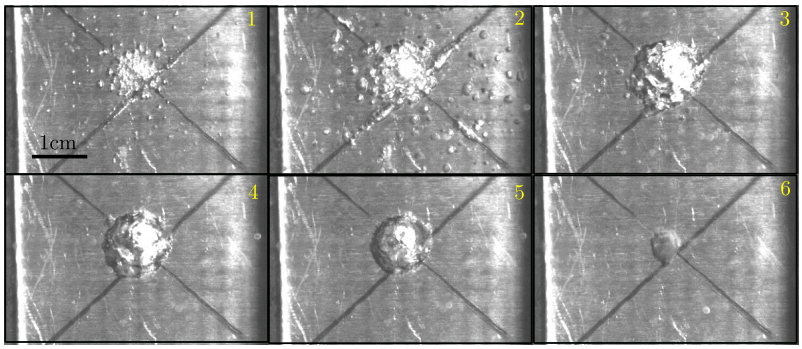


Figure 1.4: The top view of bubbles nucleating in the liquid bath due to the laser impact on the opposite side of aluminum plate obtained using setup shown in reference [66].

to be fully understood, which differs significantly from classical laser induced bubbles formed by directly focusing the laser in liquid discussed above.

### 1.2.3 Understanding of cavitation and current gaps

The first formal study to understand the phenomenon of the cavitation can be found in the seminal article of lord Rayleigh published in 1917 [67]. He derived and solved an ordinary differential equation to relate the evolution of bubble radius with the changes in far field pressure in case of the spherically symmetric gaseous bubble collapsing in an infinite mass of liquid. This study was motivated by the understanding of cavitation damage. Over the last century, since 1917 the researchers have tried to answer several questions to broaden the understanding of cavitation. Some of these can be identified to be: In which situations does the cavitation bubbles appear? How does these bubbles interact with the surroundings? What is the mechanism of damage caused by the collapse of these bubbles? Can we control, predict and utilize the cavitation phenomenon? Now, we briefly discuss how far we have reached to answer these questions, what is the current understanding and gaps related to the two fundamental aspects of cavitation i.e. bubble nucleation and bubble collapse.

#### Heterogeneous bubble nucleation

The studies of the nucleation of bubbles and the underlying factors important for the generation of bubbles began with the influential work of Harvey [68, 69]. He aimed to explain the decompression sickness among the aviators during the world-war at intermediate altitudes in the absence of pressurized chambers. He hypothesized that small mass of gases (nuclei) can stick to hydrophobic surfaces or surface impurities, and when the pressure difference exceeds the surface tension the nuclei may become unstable. However, he did not perform the calculations for the critical pressures beyond which these nuclei will become unstable. He also showed several other phenomenon in which these nuclei could grow to large bubbles namely dissolution of excess gas from the bulk similar to effervescence in the soda bottle, passage of intense sound waves, local drop in hydrodynamics pressure due to constriction in pipe flows. These ideas laid the foundation for the theory of heterogeneous nucleation. Several researchers attempted to measure the threshold

beyond which noticeable cavitation activity occurs but the unified view was always lacking[70, 71, 72]. Apfel [73] provided a unified view and discussed the importance of several parameters such as crevice size, surface properties, surface tension etc. He concluded that these previous experimental results can not be considered as accurate quantitative predictions as one will always fail to precisely know the shape, size and wettability of the motes used in the experiments. Crum [74] showed that the experimental threshold could be predicted well from stability theory using an approximation for the wetting which gives the equilibrium contact angle and one fitting parameter i.e. the pit angle. Atchley & Prosperetti [75] gave a more generalized and complete theoretical model for predictions of cavitation thresholds for the spherical cap shaped bubbles evolving in conical shaped crevices for quasi-static bubble evolution. Neppiras & Noltingk [76] and Holland & Apfel [77] discussed the effect of frequency of pressure wave on the stability of the spherical bubbles. Chappel et. al. [78] show the effect of geometry of pit on the prediction of nucleation threshold from quasi-static theory. Fuster et. al. [79] discussed the stability of bubbly liquids from energy approach and discussed the relation of stability with cavitation inception. Borkent et. al. [80] created micron-sized pits in the silicon wafers with advanced machining operations which act as well controlled nuclei and showed that the theoretically predicted cavitation thresholds from quasi-static theory represent well the experimentally observed thresholds. They also show that the mechanism of jetting during the collapse which lead to deactivation of nuclei for following pressure cycle.

Most of the studies mentioned above have been focused on the prediction of nucleation threshold for air bubbles and water. There are several works motivated from the biomedical applications that predict the nucleation threshold for non-Newtonian fluids that mimic blood and tissues [81, 82, 83, 84]. There are also a few in-vivo studies of the cavitation [85, 86]. Clearly the problem of nucleation is complicated as a lot of factors are convoluted and hard to control separately. The problem of bubble nucleation has less often been studied using the Computational Fluid Dynamics (CFD) tools which can be convenient in such situations with enormous number of control parameters. Moreover, the numerical simulations can provide clues about the quantities and flow-fields which are difficult to measure in the experiments. We aim to understand the the influence of characteristics of wall, shape of the nuclei, the amplitude as well as frequency of pressure forcing and motion of contact line on the process of bubble nucleation and the resulting bubble shapes. This is presented in detail in the third chapter.

### Bubble collapse

Most of the studies investigate the collapse of bubbles unconnected to the nucleation phase. These are focused on the consequences of the collapse of a gas/vapor cavity that has already reached a given volume and shape. These studies are generally aimed towards the understanding of the destructive potential of the cavitation bubbles and their interaction with the surroundings. There is a plethora of literature dedicated to the collapse of bubbles highlighting it's significance. The collapse problem studied by Lord Rayleigh is an idealized one as the bubble collapse is rarely spherically symmetric and the asymmetry is commonly caused by the presence of boundary near or in contact with the collapsing bubble that results in to high speed liquid jets. It is well known that the jets formed during the collapse of bubbles in the presence of a nearby wall are directed towards the wall and that the characteristics of these jets can be described well using the scaling laws given

by [87] and [2]. The collapse of bubbles close to a rigid wall is generally modeled with the kelvin impulse theory as for such a case the Kelvin impulse remain conserved if the external forces are absent and the bubble remains simply connected [88, 89, 90]. These models are unable to predict correct bubble dynamics when the distance between bubble and wall approaches to bubble size ($h/R_0 \sim \mathcal{O}(1)$) because the bubble deformation is more and more significant this fact limits the applicability of such model for collapse of bubbles in contact with wall.

The investigations on the collapse of a bubble initially attached to a wall are reported less often therefore many aspects remain unexplored. Naude & Ellis [91] discuss the collapse of bubble initially in contact with wall by writing the higher order perturbation solutions to potential flow model. They also show the collapse dynamics of such bubbles experimentally by producing bubbles with electric spark in the liquid close to wall. Hupfeld et. al. [58] presented experimental results for laser induced bubbles using ultra-high speed photography in the high capillary number regimes. They study both expansion and collapse phase in several liquids to understand the effect of viscosity on the growth, collapse and bubble shapes including liquid microlayer and contact line evolution. Both Naude & Ellis and Hupfeld show that during the collapse the jet is directed towards the solid whereas Li et. al. [92] show that the jet can be directed in opposite direction when a collapsing bubble is in contact with a spherical solid particle. Similar problem is studied numerically by Lechner et.al. [93], who also include the effect of bubble expansion and the liquid microlayer that results in to different nature of bubble collapse and jetting. This problem has also been briefly discussed in numerical studies of Lauer et. al. and Koukouvinis et. al. [94, 95] who observe the change in jetting behavior as a function of bubble shape but they do not show jets opposite to the wall. Reuter et. al. [96] speculate the appearance of a jet parallel to the wall during the secondary collapse and consequently the generation of vortex ring, although no direct experimental observation is reported. In chapter 4, we numerically, experimentally and theoretically study the problem of collapse of bubbles in contact with rigid wall as a function of the properties of wall and understand the change in jetting behavior. We also characterize the liquid jets direction and the strength in terms of the kinetic energy accumulated in them at the instant of minimum radius.

## 1.3 Manuscript outline

This manuscript is organized in 6 chapters, the brief outline of the contents of each chapter is as follows:

In chapter 2, we present the governing equations for a generic two-phase compressible flow problem. We detail out the intricate details of the numerical method that we use to perform the numerical simulations and describe the Navier-slip model used to model the contact line. We also derive basic thermodynamic relations that must be satisfied during the expansion/collapse of bubbles using the first law of thermodynamics. The non-dimensional numbers relevant for the problem of expansion/collapse of bubbles are also introduced at the end of this chapter.

In chapter 3, we discuss the numerical and theoretical results for the estimation of the heterogeneous nucleation threshold for spherical cap nuclei attached to a wall. We understand the dependence of nucleation threshold on the behavior of contact line by discussing the two extreme conditions of freely moving contact line and pinned contact line. We also discuss the finite pulse

duration effects on the explosive growth of spherical bubbles. Then, we describe the dynamics of microlayer formation when the bubbles nucleate under a pressure much lower than the critical threshold using a Navier-slip model for the contact line motion. We show several aspects of the microlayer formation and growth which is governed by visco-capillary effects close to the wall.

In chapter 4, we focus on describing the collapse dynamics of spherical cap bubbles in contact with a rigid wall. We use an inviscid impulse theory to predict the acceleration of the bubble interface at very short times which reveals that the acceleration at the contact line is singular for certain bubble shapes. Using direct numerical simulations, we clarify the effect of viscosity at short times and discuss the collapse dynamics at longer times. The influence of non-spherical effects on the peak gas pressures reached during the collapse are also discussed using DNS and the fundamental energy relations obtained in Chapter 2. Then, we directly compare the numerical results with experiments for the collapse of bubbles attached to a wall and understand the phenomenon of jetting. We show that in some special circumstances, these jets can lead to the formation of a vortex ring that induces long range effects caused by a cavitation bubble.

In chapter 5, we revisit the problem of multi-bubble cavitation using three-dimensional numerical simulations. We study the case of bubble pairs, five bubbles in a line and a cluster of thirty seven bubbles in an hexagonal arrangement. In particular, we investigate the asymmetry during the expansion and collapse phase in these cases. Numerical simulations reveal that much smaller speed of sound is required to accurately reproduce the dynamics of the bubbles observed in the experiments. For a particular example of bubble pair, we show that the asymmetry scales well with the Bjerknes forces in the expansion phase, and is affected by Rayleigh–Taylor instabilities during the collapse phase. We also discuss the effect of the size of nuclei on the asymmetry for this particular case. In the end, we present the dynamics of the expansion and collapse of multiple bubbles.

In chapter 6, we give the concluding remarks and the future perspectives of current work.

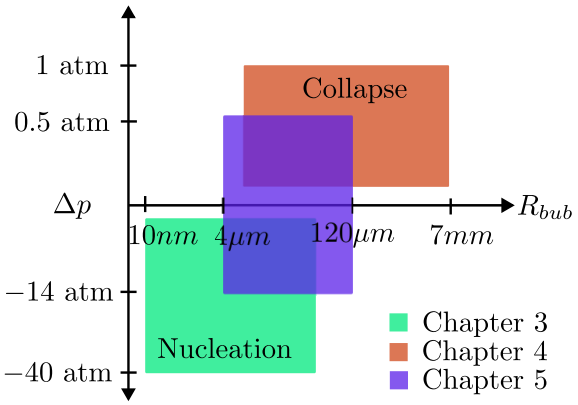


Figure 1.5: The bubble size and driving pressure considered in different chapters

In figure 1.5, we pictorially depict the length scales of bubbles and scales of driving pressure (difference in pressure inside the bubble and the liquid pressure) that is studied in the chapters mentioned above. In the nucleation problem, we consider the nuclei of nanometer to few microns in size subjected to very high tensions. In the collapse problem, we focused mainly on the

millimeter size bubbles collapsing under the action of atmospheric pressure. In the multibubble cavitation, these scales corresponds to previous experiments of Bremond et. al. [55]. There the pressure is as low as $-14$MPa and the bubbles are micrometer in size.

## 1.4 Journals and conferences

There is a journal article that is already published from the current work three others are in the progress.

- Saini, M., Tanne, E., Arrigoni, M., Zaleski, S., & Fuster, D. (2022). "On the dynamics of a collapsing bubble in contact with a rigid wall". Journal of Fluid Mechanics, 948, A45.[97]
- Saini Mandeep, Saade Youssef, Fuster Daniel, & Lohse Detlef. "Finite speed of sound effects on asymmetry in multibubble cavitation."(In prepration)
- Saini, Mandeep, Zaleski Stephane and Fuster Daniel. "Dynamics of microlayer formation in hetrogeneous bubble nucleation: Numerical study with slip model" (In prepration)
- Saini, Mandeep, Zaleski Stephane and Fuster Daniel. "Non-spherical effects during the collapse of bubble in contact with wall" (In planning)

The part of current work is also presented to the fluid mechanics community during following conferences

- Saini, Mandeep, Zaleski Stephane and Fuster Daniel. "Direct numerical simulation of heterogeneous bubble nucleation" 11th International Cavitation Symposium (CAV2021), 2021. [98].
- M Saini, D Fuster. "Singularity influences jet direction during the collapse of bubbles in contact with walls". APS Division of Fluid Dynamics Meeting Abstracts, H21. 010
- D Fuster, M Saini, E Tanne, M Arrigoni. "Contact line singularity triggers far field perturbations during bubble collapse" APS Division of Fluid Dynamics Meeting Abstracts, P21. 001
- M Saini, D Fuster. "Viscous and capillary effects on the dynamics of sub-micron bubbles attached to walls" Nanobubble production 7, 37

# 2 Governing equations and Numerical methods

In this chapter, we present the basic governing equations and the numerical method used to solve these equations. We write the differential form of the compressible Navier–Stokes for a generic two-component system. These are integrated numerically using the finite volume method and the all-Mach formulation generalized for two-phase flows by Fuster et. al. [99]. The solver is available as a part of the state of the art Basilisk partial differential equation solver, that uses the quad/oct tree grid structure which makes it apt for problems involving multiple length scales [100, 101]. The interface between the two fluids is represented by the volume of fluid (VOF) method [102]. The conservative quantities are consistently advected along with a geometric VOF, and we also consider effect of both viscosity and surface tension. This solver has been used to describe the bubble dynamics in several problems [103, 104]. We also discuss the modeling of the contact line using the Navier-slip model intrinsic to volume of fluids methods. The integral form of the energy conservation equation is presented for a system of a gas bubble of arbitrary shape expanding/collapsing in a weakly compressible liquid to aid the interpretation of DNS results. Finally, we show the relevant non-dimensional numbers that we have used in the next chapters to discuss the results.

## 2.1 Governing equations

The fundamental equations of mass, momentum and energy conservation govern the fluid flow dynamics in each component. In the absence of mass transfer these equations can be written for two-component ($i \in \{1, 2\}$) setup as following

$$\frac{\partial \rho_i}{\partial t} + \boldsymbol{\nabla} \cdot (\rho_i \mathbf{u}_i) = 0, \tag{2.1}$$

$$\frac{\partial \rho_i \mathbf{u}_i}{\partial t} + \boldsymbol{\nabla} \cdot (\rho_i \mathbf{u}_i \mathbf{u}_i) = -\boldsymbol{\nabla} p_i + \boldsymbol{\nabla} \cdot \boldsymbol{\tau}_i, \tag{2.2}$$

$$\frac{\partial (\rho_i E_i)}{\partial t} + \boldsymbol{\nabla} \cdot (\rho_i E_i \mathbf{u}_i) = -\boldsymbol{\nabla} \cdot (\mathbf{u}_i p_i) + \boldsymbol{\nabla} \cdot (\boldsymbol{\tau}_i \mathbf{u}_i), \tag{2.3}$$

where the subscript '$i$' represent the value of particular variable for $i^{th}$ component, other symbols have usual meaning, $\mathbf{u}$ is the velocity vector field, $\rho$ is the density, $p$ is the pressure field, $E$ is the total energy per unit volume which is defined as sum of internal energy and kinetic energy ($\rho_i e_i + \frac{1}{2}\rho_i \mathbf{u}_i \cdot \mathbf{u}_i$) and $\boldsymbol{\tau}_i = \mu_i(\boldsymbol{\nabla}\mathbf{u}_i + (\boldsymbol{\nabla}\mathbf{u}_i)^{\mathrm{T}} - \frac{2}{3}\boldsymbol{\nabla} \cdot \mathbf{u_i} I)$ is the viscous stress tensor.

The system of equations is closed by the equation of state for each component. We use stiffened gas equation of state (EOS) similar to Johnsen & Colonius and Cocchi et. al. [105, 106], given as

$$\rho_i e_i = \frac{p_i + \Gamma_i \Pi_i}{\Gamma_i - 1}, \tag{2.4}$$

where $\Gamma$ and $\Pi$ are empirical parameters, for water $\Gamma = 5.5$ and $\Pi = 4921$ bar and for an ideal gas $\Gamma = \gamma$ and $\Pi = 0$. This defines the speed of sound as

$$c_i = \sqrt{\Gamma_i \frac{p_i + \Pi_i}{\rho_i}}. \tag{2.5}$$

Note that the stiffened gas EOS is an empirical equation which captures compressibility effects well for common liquids such as water but it suffers from inaccuracies when used to predict the thermal effects. Alternative EOS are also available in literature eg. Nobel–Abel-stiffened-gas (NASG) EOS, Gilmore–NASG etc [107, 108], and also available in the Basilisk solver [109].

The interface between the two immiscible fluids is mathematically represented by the heaviside function ($\mathcal{H}$) which takes value 1 in the reference component and 0 in the non-reference component [110]. The evolution of the interface is described by the advection equation

$$\frac{\partial \mathcal{H}}{\partial t} + \mathbf{u} \cdot \boldsymbol{\nabla} \mathcal{H} = 0, \tag{2.6}$$

where $\mathbf{u}$ is the average local velocity of the interface which is imposed to be equal to local fluid velocity. The interface conditions required to couple the motion of fluids in each component, in the absence of mass transfer effects these are as follows: the velocity is continuous across the interface such that $[[\mathbf{u}]] = 0$, where $[[.]]$ represent the jump in the particular quantity across the interface. The pressure in both the components is related by the Laplace equation

$$[[p]] = -\sigma\kappa + [[\mathbf{n}_I \cdot \boldsymbol{\tau} \cdot \mathbf{n}_I]], \tag{2.7}$$

where $\sigma$ is the surface-tension coefficient, $\kappa$ is the curvature of the interface and $\mathbf{n}_I$ is the unit vector normal to the interface. We also assume that there is no heat transfer across the interface so the normal derivative of internal energy remains continuous across the interface i.e. $[[\partial e/\partial n]] = 0$.

In the current formulation, we also solve for a pressure equation which leads to a time implicit method and removes the stringent acoustic Courant–Ferdrichs–Lewy (CFL) restriction [111]. This equation is derived from a general equation of state (see reference [62, 99]) and is given as

$$\frac{1}{\rho c^2}_{e,i} \frac{Dp_i}{Dt} = -\nabla \cdot \mathbf{u}_i + \frac{\beta_i \Phi_\nu}{\rho_i c_{p,i}}, \tag{2.8}$$

where we define $\frac{1}{\rho c^2}_{e,i} = \frac{\gamma_i}{\rho_i c_i^2} - \frac{\beta_i^2 T}{\rho_i c_{p,i}}$, $\gamma$ is the ratio of specific heats, $\beta$ is the thermal dilation coefficient, T is the temperature, $c_p$ is the specific heat measured at constant pressure, $\Phi_\nu = \boldsymbol{\tau} : \nabla \mathbf{u}$ is the viscous dissipation function. Note that for ideal gas $\beta = 1/T$ and for water $\gamma = 1$ & $\beta \approx 0$, therefore for these fluids we can approximate $\frac{1}{\rho c^2}_{e} \approx \frac{1}{\rho c^2}$ in such cases.

## 2.2 Numerical method

In this section, we discuss the details of numerical method used to integrate the equations described in previous section on the finite volume grids and in time. The framework of the numerical method is based on following choice of primitive variables: the density $\rho_i$, average momentum $\rho\mathbf{u}$, the total energy of each component $\rho_i E_i$ and volume fraction $C$. The viscosity $\mu_i$ and surface tension $\sigma$ are assumed to be constants. This choice of primitive variables leave the average pressure $p$ as an auxiliary variable. Note that since the density is the primitive variable whereas pressure is an auxiliary, the current method is a density based solver among the classical distinction of pressure and density based solvers [112, 113, 114]. The current formulation naturally recovers the standard projection methods in the incompressible limit (i.e. $c \to \infty$) of Navier–Stokes equations [115, 116].

### 2.2.1 Interface representation

The interface between the two fluids is represented by the VOF method which was first described by Hirt and Nicolas [102]. In this method, the integration of the heavyside function on the discrete volumes (cells) is approximated as the color function [110] given as

$$C_{i,j,k} \approx \frac{1}{\int_V dV} \int_V \mathcal{H}(x,y,z)dV, \tag{2.9}$$

were $i, j, k$ represent the indices that determine the location of the control volumes. $C$ takes value 0 or 1 far from the interface and an intermediate fractional value in the mixed cells (cells containing interface). To calculate the advection fluxes, we use the direction split method of Weymouth and Yue [117] which is proved to be fully conservative in the limit of incompressible flows. Therefore the advection equation for color function is given as

$$\frac{\partial C}{\partial t} + \boldsymbol{\nabla}\cdot(\mathbf{u}C) = C\,\boldsymbol{\nabla}\cdot\mathbf{u}. \tag{2.10}$$

The term on right hand side accounts for compressibility effects. Note that since the velocity is continuous across the interface it is convenient to define average velocity field i.e. $\mathbf{u}$ everywhere in the domain instead of $\mathbf{u}_i$ for each component. After solving equation 2.10, the interface is reconstructed from the color function field using piece wise linear interface construction (PLIC) in which the interface is represented as lines (in 2D) and planes (in 3D) in each control volume.

### 2.2.2 Advection step

In the beginning of each time integration step, we solve the advection equation for color function and other conservative quantities. We use first order forward Euler method for discretization of temporal term and divergence theorem to convert the volume integral into the surface integrals. Thus obtained semi-discrete form of equation 2.10 can be written as

$$\int_V \frac{C^{n+1} - C^n}{\Delta t} dV = -\int_S \mathbf{u}C d\mathbf{S} + \int_V C\,\boldsymbol{\nabla}\cdot\mathbf{u} dV \tag{2.11}$$

In the direction split method (see reference [117]) the discrete form of the advection equation takes following form

$$C^{n+1} = C^n - \sum_f F_c(u_f \Delta t/\Delta x, C) + \Delta t C^* \sum_f \nabla_f \mathbf{u}, \tag{2.12}$$

where subscript '$f$' refers to the value of particular quantity evaluated at the faces centers, $F_c$ is the net flux of the reference fluid out of the control volume of size $\Delta x \times \Delta x \times \Delta x$ (in 3D) evaluated geometrically and sequentially in all the direction, $C^*$ is a constant defined on the basis of cell center value of $C$.

To have a consistent formulation, we solve the advection equation for the conservative quantities simultaneously with the color function field using the direction split algorithm, therefore the discrete integral form of advection equation for conservative quantities can be written as

$$\mathbf{Y}^{(adv)} = \mathbf{Y}_c^n - \sum_f \mathbf{F}^{(adv)}(\Delta t u_f/\Delta x, C, \mathbf{Y}_c) \tag{2.13}$$

where $\mathbf{Y} = [C_i, C_i\rho_i, C_i\rho_i\mathbf{u}, C_i\rho_i E_i]^{\mathrm{T}}$ for $i \in \{1, 2\}$, $\mathbf{F}^{(adv)}$ is the vector of flux of the quantities $\mathbf{Y}$ across the face during $\Delta t$. The advection of conservative quantities is linked to the advection of the color function $C$, so the flux is expressed as $\mathbf{F}^{(adv)} = F_c(u_f \Delta t/\Delta x, C)\mathbf{F}_Y^{(adv)}$, where $F_c$ is already calculated equation 2.12 and the $\mathbf{F}_Y^{(adv)}$ is calculated using the second order accurate Bell–Colella–Glaz (BCG) scheme [116] given for reference component (subscript 1) as following

$$\mathbf{F}_Y^{(adv)} = \begin{cases} \mathbf{Y}_c + \frac{1}{2}\mathrm{sign}(u_f)\min\left(1, 1 - \mathrm{sign}(u_f)\frac{u_f \Delta t}{\Delta x}\right)\frac{\partial \mathbf{Y_c}}{\partial x}\Delta x, & \text{if } C > 0, \\ 0, & \text{otherwise.} \end{cases} \tag{2.14}$$

Naturally, for the non-reference component (subscript 2) the first condition in equation 3.1 changes $(1 - C) > 0$. The numerical scheme proposed above is fully conservative in the discrete framework, consistent in the flux calculation of the conservative quantities along with the color function and avoids numerical diffusion during this step. These properties are essential for numerical stability when two fluids have large density contrast such as air-water [118, 119, 120, 121]. Note that the equation 2.1 is an advection equation therefore equation 2.13 gives density field at the end of time-step $t + \Delta t$ whereas the momentum and energy are only provisional/intermediate fields that will be used to calculate the respective values at the $t + \Delta t$.

### 2.2.3 Prediction step

At the end of advection step, we calculate the average momentum using arithmetic averaging formula $\rho\mathbf{u} = \rho_1\mathbf{u}C + \rho_2\mathbf{u}(1 - C)$, and thereafter we solve for the equation of average momentum given as

$$\frac{\partial \rho\mathbf{u}}{\partial t} + \boldsymbol{\nabla}\cdot(\rho\mathbf{u}\mathbf{u}) = -\boldsymbol{\nabla}p + \boldsymbol{\nabla}\cdot\boldsymbol{\tau} + \mathbf{F}_\sigma, \tag{2.15}$$

where $\mathbf{F}_\sigma$ is the surface tension force. In this step, we find a prediction of velocity ($\mathbf{u}_p^{n+1}$) at $t + \Delta t$ using the advected momentum $\rho\mathbf{u}^{(adv)}$, surface-tension contribution at $\mathbf{F}_\sigma^{n+1}$ and pressure from previous time step $p^n$. We start by calculating the surface tension contribution at $n + 1^{th}$ time step. The surface tension force can be obtained using Frenet formula ($dt = \kappa\mathbf{n}ds$) for any curvilinear coordinate $s$, as following [110, 122]

$$\mathbf{F}_\sigma = \oint_A^B \sigma dt = \oint_s \sigma\kappa\mathbf{n}ds = \int_\Omega \sigma\kappa\mathbf{n}\delta_s, \tag{2.16}$$

where $\Omega$ is control volume intersected by interface at $A$, $B$, $\delta_s$ is surface Dirac function concentrated at the interface which can represented with the gradient of heavyside function $\boldsymbol{\nabla}\mathcal{H}(x - x_s)(y - y_s)$ where $x_s, y_s$ is the interface position. We use the volumetric formulation using Continuum Surface Model (CSF) model of Brackbill et. al. [123], where the gradient of heavyside function is numerically approximated with gradient of color function (gradient of eq 2.9) thus $\mathbf{F}_\sigma = \int_V \sigma\kappa\boldsymbol{\nabla}C$. To predict the curvature accurately, we use the height function method [122, 124, 125], which is proven to be well-balanced, meaning that, the steady equilibrium solution is recovered and the numerical spurious currents decay up to machine accuracy within viscous time scales. This method relies on the fact that in local coordinates curvature can be estimated as following

$$\kappa = \frac{h_y''}{(1 + h_y')^{3/2}}, \tag{2.17}$$

given that $h_y$ is discretely defined using the color function, one can obtain the curvature with high accuracy. As the surface tension contribution is time explicit, the time step is restricted by the time scale of the fastest capillary waves [126, 127], so for stability

$$\Delta t < \sqrt{\frac{(\rho_1 + \rho_2)\Delta^3}{4\pi\sigma}}. \tag{2.18}$$

Finally, we calculate the prediction for the velocity ($\mathbf{u}_p^{n+1}$) by solving full Navier–Stokes equation using the multigrid solver which is already implemented in Basilisk,

$$\frac{\mathbf{u}_P^{n+1} - \mathbf{u}^{(adv)}}{\Delta t} = -\frac{1}{\rho^{n+1}}(\boldsymbol{\nabla}p)^n + \frac{1}{\rho^{n+1}}\boldsymbol{\nabla}\cdot\Big(\mu\Big(\boldsymbol{\nabla}\mathbf{u}_P + (\boldsymbol{\nabla}\mathbf{u}_P)^T\Big)\Big)^{n+1} + \frac{1}{\rho^{n+1}}F_\sigma^{n+1}, \tag{2.19}$$

where, we use harmonic mean to define average viscosity ($\frac{1}{\mu} = \frac{C}{\mu_1} + \frac{1-C}{\mu_2}$) as it results in faster convergence of multigrid viscous solver, and arithmetic mean for density $\rho = C\rho_1 + (1 - C)\rho_2$.

### 2.2.4 Projection step

In this step, we solve the evolution equation of average pressure to obtain $p^{n+1}$ and finally the momentum $(\rho\mathbf{u})^{n+1}$. We define the average pressure using the arithmetic average i.e. $p = p_1C + p_2(1 - C)$. The average pressure obeys

$$\frac{1}{\rho c^2}_e \left( \frac{\partial p}{\partial t} + \mathbf{u} \cdot \boldsymbol{\nabla} p \right) = \boldsymbol{\nabla} \cdot \mathbf{u} + \frac{\beta_T \Phi_\nu}{\rho c_p}, \tag{2.20}$$

where we define the average for parameters of EOS using the arithmetic mean as

$$\frac{1}{\Gamma - 1} = \frac{C}{\Gamma_1 - 1} + \frac{1 - C}{\Gamma_2 - 1}, \tag{2.21}$$

$$\frac{\Gamma \Pi}{\Gamma - 1} = C \frac{\Gamma_1 \Pi_1}{\Gamma_1 - 1} + (1 - C) \frac{\Gamma_2 \Pi_2}{\Gamma_2 - 1}, \tag{2.22}$$

this further gives the effective speed of sound in the mixed cells ($0 < C < 1$) as

$$\frac{1}{\rho c^2}_e = \frac{\frac{1}{\Gamma - 1}}{p\left(\frac{1}{\Gamma - 1} + 1\right) + \frac{\Gamma \Pi}{\Gamma - 1}}. \tag{2.23}$$

In the current formulation, we have neglected the viscous dissipation term in the pressure equation for simplicity. Thus the semi-discrete form of pressure evolution equation obtained from equation 2.20 is given as

$$\frac{1}{\rho c^2}_e \left( \frac{p^{n+1} - p^n}{\Delta t} + \mathbf{u} \cdot \nabla p \right) = \nabla \cdot \mathbf{u}^{n+1}, \tag{2.24}$$

In order to simplify this equation we use the correction equation for the momentum

$$(\rho \mathbf{u})^{n+1} = (\rho \mathbf{u})^* - \Delta t \nabla p^{n+1}, \tag{2.25}$$

In the spirit of the projection step in classical incompressible formulation, we divide equation 2.25 by the average density $\rho = C\rho_1 + (1 - C)\rho_2$ and take the divergence of resulting equation to obtain

$$\nabla \cdot \mathbf{u}^{n+1} = -\nabla \cdot \left( \frac{\Delta t}{\rho} \nabla p \right) + \nabla \cdot \mathbf{u}^*, \tag{2.26}$$

where $\mathbf{u}^*$ is computed from the provisional velocity $\mathbf{u}_P^{n+1}$ obtained in previous section

$$\mathbf{u}^* = \mathbf{u}_P^{n+1} + \frac{\Delta t}{\rho^{n+1}} \nabla p^n. \tag{2.27}$$

After substitution of equation 2.26 into equation 2.24, we obtain an advection-diffusion-reaction equation for pressure as

$$\frac{1}{\rho c^2}_e \left( \frac{p^{n+1} - p^n}{\Delta t} + \mathbf{u} \cdot \nabla p \right) = -\nabla \cdot \left( \frac{\Delta t}{\rho} \nabla p \right) + \nabla \cdot \mathbf{u}^*, \tag{2.28}$$

Writing the semi-discrete advection equation for pressure to obtain advection pressure ($p^{(adv)}$)

$$\frac{p^{(adv)} - p^n}{\Delta t} = -\mathbf{u} \cdot \nabla p \tag{2.29}$$

we can substitute $p^{(adv)}$ into equation 2.28 to obtain

$$\frac{1}{\rho c^2}_e \frac{p^{n+1} - p^{(adv)}}{\Delta t} = -\nabla \cdot \left( \frac{\Delta t}{\rho} \nabla p \right)^{n+1} + \nabla \cdot \mathbf{u}^*. \tag{2.30}$$

This is an Helmholtz–Poisson equation, which in the incompressible limit $c_e \to \infty$ reduces to the standard Poisson equation solved in projection method for incompressible flows.

In practice, to solve for equation 2.29 we use the advected values of primitive variables and EOS to approximate $p^{(adv)}$ as [128]

$$p^{(adv)} \approx \rho E^{(adv)} - \frac{1}{2}\rho \mathbf{u} \cdot \mathbf{u}^{(adv)} - \frac{\Gamma \Pi}{\Gamma - 1}, \tag{2.31}$$

where we again use arithmetic averaging to write average energy

$$\rho E^{(adv)} = C\rho_1 E_1^{(adv)} + (1 - C)\rho_2 E_2^{(adv)},$$

and $1/2\rho\mathbf{u} \cdot \mathbf{u}^{(adv)}$ is obtained from the average density $\rho$ and advected momentum $\rho\mathbf{u}^{(adv)}$. Note that, using the EOS to predict $p^{(adv)}$ also couples the energy and momentum equations.

The value of $\rho c_e^2$ is computed using equation 2.23 leaving $p^{n+1}$ as the only unknown in equation 2.30, that is solved using the multigrid solver of Basilisk. Once $p^{n+1}$ is obtained, we compute $(\rho\mathbf{u})^{n+1}$ using equation 2.25. Finally, to obtain $(\rho_i E_i)^{n+1}$, we find the pressure for each fluid from the average pressure using the Laplace equation (equation 2.7) while neglecting the jump in pressure due to viscous stresses

$$p_1 = p + (1 - C)\sigma\kappa, \tag{2.32}$$
$$p_2 = p - C\sigma\kappa. \tag{2.33}$$

Thus we get the estimates of total energy at $n + 1^{th}$ time step for each component as

$$(\rho_i E_i)^{n+1} = (\rho_i E_i)^{(adv)} + \Delta t(-\nabla \cdot (\mathbf{u} p_i) + \nabla \cdot (\boldsymbol{\tau}_i \cdot \mathbf{u}))^{n+1}, \tag{2.34}$$

Once we have obtained the values of all the variables at $t + \Delta t$, we check if the stopping criteria for the simulation is reached, and otherwise we march to next time step. The complete algorithm is shown in figure 2.1. In the cases where we use adaptive mesh refinement, we refine and coarsen the mesh based on values of second order derivatives of certain quantities compared to the case specific thresholds before marching to next time step.

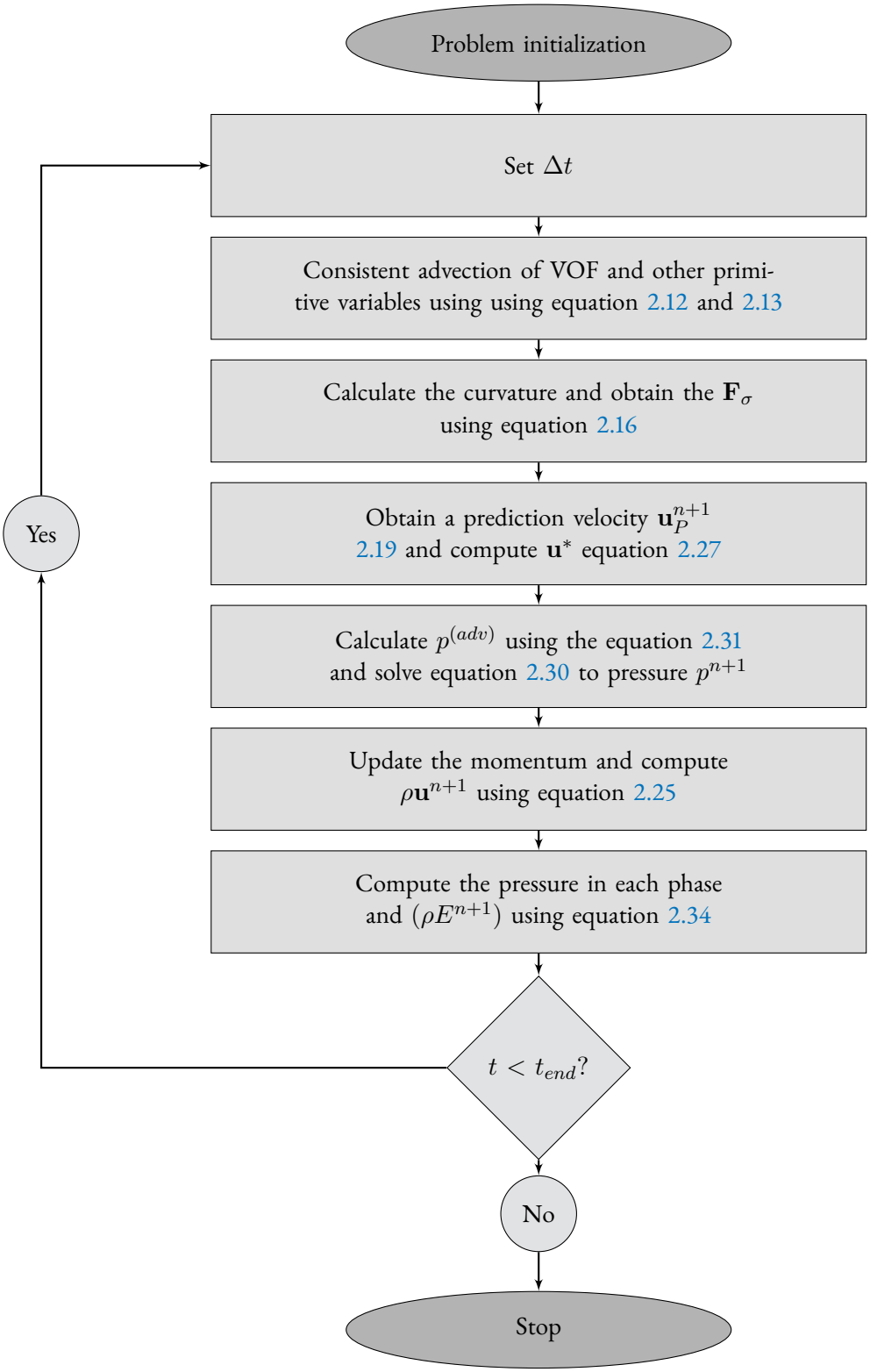


Figure 2.1: The algorithm for all-Mach solver

## 2.3 Numerical model for moving contact lines

The surface tension is the macroscopic manifestation of the imbalance of inter-molecular forces of attraction at the interfaces of different fluids or fluid-solid pairs. A number of setups have been studied in past (eg. dip coating, plunging plate, drop spreading etc.) where the three component co-exist at a line (in 3D) [129, 130, 131, 132]. The line joining three components (two fluids and a solid) is commonly called contact line and the angle between the interfaces measured in the reference fluid is called contact angle. In an thermodynamic equilibrium state of partially wetted homogeneous solid, the contact angle ($\alpha_E$) observed at macroscopic scale is well defined (see reference [129]) and results from the balance of tension along the interfaces given as

$$\cos(\alpha_E) = \frac{\sigma_{sg} - \sigma_{sl}}{\sigma_{lg}}, \tag{2.35}$$

where $\sigma_{lg}$, $\sigma_{sg}$ and $\sigma_{sl}$ are the surface tensions for the gas-liquid, gas-solid and liquid-solid surface respectively. In reality, the surfaces are non-homogeneous which can cause pinning effects that induce hysteresis in the contact line motion such that $\alpha_a < \alpha < \alpha_r$ where $\alpha_a$ & $\alpha_r$ are advancing and receding contact angles [130]. The problem of moving contact lines is more complicated as the thermodynamic equilibrium between the components can no longer be established and the contact angle is given by the dynamic force balance at the molecular scales. In such a case, it is convenient to define an apparent contact angle ($\alpha_{app}$) which is observed at macroscopic scales, generally at few microns. At these length scales (of the micro meter order), the interface slope ($\alpha_{app}$) is often predicted from the balance of viscous and capillary forces [133, 134]. The actual physics at length scales smaller than few microns is not well understood and it is generally assumed that the inter-molecular forces lead to an microscopic angle ($\alpha_m$) for homogeneous surface. Moreover, the hydrodynamic theory with no-slip boundary condition applied to moving contact lines results in logarithmic divergence of viscous stresses upon approaching the contact line [110, 135].

In the numerical models generally employed for the contact line motion a slip is assumed to occur at the smallest length scale of grid size ($\Delta_x$) which relax the standard no-slip boundary condition and remove the stress singularity. In volume of fluid methods, a slip length of $\Delta_x/2$ is introduced implicitly because the interface moves at the non-zero velocity of the cell center located half a grid cell away from solid boundary. This results in grid dependent solutions for the motion of the contact line, Nevertheless, the influence of this numerical effect decays logarithmically with the distance from contact line at large length scales. Another commonly used method is to employ a grid independent slip using Navier-slip boundary condition [136]

$$u_T + U_b = \lambda \frac{\partial u_T}{\partial n}, \tag{2.36}$$

where $u_T$ is the velocity component tangent to the solid boundary and $n$ is the normal direction. This model leads to the grid convergent results for the motion of contact line, the solution still develop on the slip-length. Note that it is computationally very expensive to reach the physically relevant slip-length and is not possible with the current state of computational resources.

In the numerical models, we also impose a contact angle ($\alpha_\Delta$ ) as a boundary condition at the length scale of grid cells and the non-equilibrium effects in the contact angle are neglected at the

scale of grid size similar to [137, 138, 139]. This angle can be seen as a numerical equivalent of the microscopic contact angle $\alpha_m$. This model is shown to recover the the results from molecular dynamics in case of shear droplet and those Cox–Voinov theory for small capillary number regime [138, 140]. The implementation of contact angles boundary condition in 2-dimensions is straight forward as

$$\frac{\partial h}{\partial x} = -\tan(\alpha_\Delta), \tag{2.37}$$

where $h$ is the interface height and x is the distance along solid boundary in the reference fluid, for method described above $h$ is simply the value of height function. In three dimensions, the contact angle implementation using height functions was given by Afkhami et. al. [141].

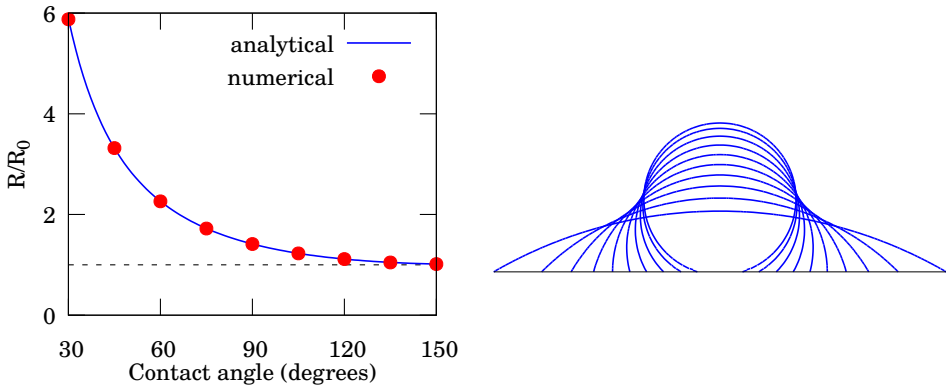


$(a)$ $(b)$

Figure 2.2: $(a)$ The radius of curvature at end of simulation for different angles of contact where analytical results are obtained from Laplace equation and mass conservation $(b)$ The interface shape at end of simulation for various angles of contact

The contact angle boundary condition is already implemented in Basilisk and tested extensively for with the incompressible solver. We check the compatibility of this model with the all–Mach solver by setting up the classical test case of sessile bubble attached to wall spreading under the effect of surface tension forces. For simplicity, we neglect the jump of density and viscosity across the interface. Other parameters are as following: the bubble size $R_0 = 0.5$, viscosity of bubble and surrounding medium $\mu_1 = \mu_2 = 1$, density of bubble and the surrounding medium $\rho_1 = \rho_2 = 1$, surface tension $\sigma = 1$, therefore the Ohnesorge number is $\mathcal{O}h = \frac{\mu}{\sqrt{\rho\sigma R_0}} = 1.5$, and the parameters for the EOS are $\Gamma_1 = 1.4, \Gamma_2 = 7.14, \Pi_1 = 300, \Pi_2 = 0$. We test the model for several contact angles from $30^\circ$ to $150^\circ$ at an interval of $15^\circ$, each bubble is initialized out of equilibrium (hemispherical shape) which then evolves to the equilibrium state. At equilibrium state, the volume of each 2D shape is analytically given as $V = R_0^2(\alpha_\Delta - \sin(\alpha_\Delta)\cos(\alpha_\Delta))$. This is verified in the figure 2.2$a$, the numerically obtained volume match well with the analytical predictions showing that the bubble is evolved to the equilibrium state. The equilibrium bubble

shapes at the end of simulation for all the contact angles is shown in 2.2b. The interface is well represented and does not show any spurious oscillations at the end of simulations.

## 2.4 Energy conservation for a gas bubble in a weakly compressible liquid

In this section, we derive some basic relations from the energy conservation principle applied to expansion/collapse of a gas bubble surrounded by an weakly compressible, Newtonian liquid. We will use these relations in the upcoming chapters to analyze and discuss the results obtained from DNS. The potential energy can be used to predict the stability of gas nuclei in liquid which gives the nucleation threshold (chapter 3). Regarding the collapse of a non-spherical bubbles the conservation of energy allows us to obtain the upper bounds of peak (gas) pressures reached during the bubble collapse (chapter 4).

The first law of thermodynamics states that net rate of change of total energy ($E$) for the system is equal to summation of the rate of work done ($\dot{W}_{ext}$), heat transfer ($\dot{Q}_{in}$), and energy dissipation ($\dot{E}_{diss}$) due to irreversible processes

$$\frac{dE}{dt} = \dot{W}_{ext} + \dot{Q}_{ext} - \dot{E}_{dis}, \tag{2.38}$$

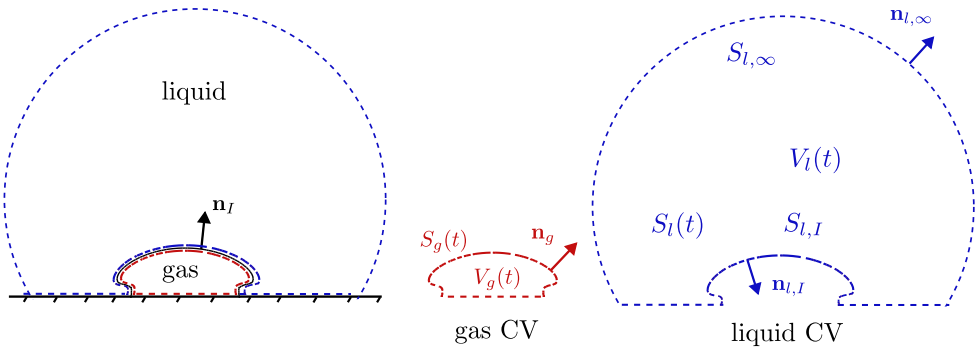


Figure 2.3: The control volumes for gas and liquid considered at a particular instant to write the energy conservation principle.

where $E_{dis}$ is always a positive quantity. The system contains an arbitrary shape gas bubble attached to wall inside a liquid bulk as shown in figure 2.3. The control volume for bubble and liquid are also shown separately with blue and red color respectively which are assumed to be moving with the local flow velocities. Let $V_g$ & $V_l$ are the volume of bubble and liquid control volumes respectively, $S_g$ & $S_l$ represent the surface area enclosing these control volumes and $\mathbf{n}_g$ & $\mathbf{n}_l$ shows the unit normal to these surfaces pointing outward from the control volume. Thus, we can write energy equation for either of the control volumes represented by subscript $i \in (l, g)$ as

$$\frac{d}{dt}\int_{V_i} \rho_i e_i dV + \frac{d}{dt}\int_{V_i} \frac{1}{2}\rho_i \mathbf{u}_i^2 dV = \int_{S_i} -p_i \mathbf{u}_i \cdot \mathbf{n}_i dS - \int_{V_i} \dot{E}_{dis} dV, \tag{2.39}$$

We impose the following assumptions to simplify the equations:

- The bubble expansion and collapse process is adiabatic and mass transfer effects are negligible.
- The effect of body force terms (eg. gravity) is assumed to be negligible.
- The bubble pressure is assumed to be uniform and bubble contains an ideal gas.

Let us first consider the bubble control volume. The internal energy evolution term for the bubble can be integrated as

$$\frac{d}{dt}\int_{V_g}\rho_g e_g dV = \frac{d}{dt}\int_{V_g}\frac{p_g}{\gamma-1}dV = \frac{d}{dt}\int_{V_g}\frac{p_{g,0}V_{g,0}^{\gamma}}{\gamma-1}V^{-\gamma}dV = \frac{p_{g,0}V_{g,0}^{\gamma}}{\gamma-1}\frac{dV_g^{1-\gamma}}{dt}, \tag{2.40}$$

where $p_{g,0}$ and $V_{g,0}$ are the gas pressure and volume for some reference equilibrium state. We can simplify the term representing work done in bubble compression/expansion using the mass conservation for the bubble as

$$\int_{S_g} -p_g\mathbf{u}_g\cdot\mathbf{n}_g dS = -p_g\int_{S_I}\mathbf{u}_I\cdot\mathbf{n}_I dS = -p_g\frac{dV_g}{dt}, \tag{2.41}$$

where $\mathbf{u}_I$ is the interface velocity and $\mathbf{n}_I$ is the normal to interface pointing from gas to liquid. Let us denote the integral of the gas kinetic energy and viscous dissipation over the bubble control volume as $E_{k,g} = \int_{V_g}\frac{1}{2}\rho_g\mathbf{u}_g^2 dV$ and $\phi_{D,g} = \int_{V_g}\dot{E}_{dis}dV$. Thus the equation 2.39 for the gas phase is given as

$$\frac{p_{g,0}V_{g,0}^{\gamma}}{\gamma-1}\frac{dV_g^{1-\gamma}}{dt} + \frac{dE_{k,g}}{dt} = -p_g\frac{dV_g}{dt} + \phi_{D,g}. \tag{2.42}$$

Now we consider the liquid control volume. The internal energy of the liquid in weakly compressible regime can be obtained as [142]

$$\rho e \approx (\rho e)_0 + \left(e_0 + \frac{p_0}{\rho_0}\right)(\rho-\rho_0) + \frac{1}{2}(\rho-\rho_0)\frac{c^2}{\rho_0}. \tag{2.43}$$

where subscript '0' represent the reference state, $c$ is the speed of sound. In the weakly compressible regime for liquid, $(\rho-\rho_0) = (p-p_0)/c^2$, therefore

$$\frac{d}{dt}\int_{V_l}\rho_l e_l dV = \frac{d}{dt}\int_{V_l}\frac{1}{2}\frac{(p_l-p_0)^2}{\rho_0 c_l^2}dV \tag{2.44}$$

To evaluate the work done in liquid, let us define $S_{l,I}$ as the surface of liquid control volume just outside the bubble interface, and $S_{\infty,l}$ represent the surface faraway surface as shown in figure 2.3. It can be readily shown from the mass conservation that

$$-\int_{S_{l,I}}\mathbf{u}_{l,I}\cdot\mathbf{n}_{l,I}dS = \int_{S_{l,\infty}}\mathbf{u}_{l,\infty}\cdot\mathbf{n}_{l,\infty}dS = \frac{dV_g}{dt}.$$

The liquid pressure $p_{l,I}$ is related to the gas pressure by Laplace law (equation 2.7). Hence, the term representing work done on the liquid can be written as

$$\begin{aligned}\int_{S_l} -p_l \mathbf{u}\cdot\mathbf{n}_l dS &= \int_{S_{l,I}} -p_{l,I}\mathbf{u}_{I,l}\cdot\mathbf{n}_{l,I}dS - \int_{S_{l,\infty}} p_\infty \mathbf{u}_{\mathbf{l},\infty}\cdot\mathbf{n}_{l,\infty}dS,\\ &= \int_{S_{l,I}} -(p_g - \sigma\kappa + [[\mathbf{n}_I\cdot\boldsymbol{\tau}\cdot\mathbf{n}_I]])\mathbf{u}_{l,I}\cdot\mathbf{n}_{l,I}dS - p_\infty\frac{dV_g}{dt},\\ &= -\int_I \sigma\kappa\mathbf{u}_I\cdot\mathbf{n}_I dS + \int_I [[\mathbf{n}_I\cdot\boldsymbol{\tau}\cdot\mathbf{n}_I]]\mathbf{u}_I\cdot\mathbf{n}_I dS\\ &+ (p_g - p_\infty)\frac{dV_g}{dt},\end{aligned} \tag{2.45}$$

Let us now denote $E_{e,l} = \int_{V_l}\frac{1}{2}\frac{(p_l-p_0)^2}{\rho_0 c_l^2}dV$, $E_{k,l} = \int_{V_l}\frac{1}{2}\rho_l\mathbf{u}_l^2 dV$ and

$$\phi_{D,l} = \int_{V_l}\dot{E}_{dis}dV + \int_I [[\mathbf{n}_I\cdot\boldsymbol{\tau}\cdot\mathbf{n}_I]]\mathbf{u}_I\cdot\mathbf{n}_I dS,$$

to write equation 2.39 for the liquid phase as

$$\frac{d(E_{e,l}+E_{k,l})}{dt} = -\int_I \sigma\kappa\mathbf{u}_I\cdot\mathbf{n}_I dS + (p_g - p_\infty)\frac{dV_g}{dt} - \phi_{D,l}, \tag{2.46}$$

Adding equations 2.42 and 2.46 we readily obtain the total energy evolution equation for the system of a gas bubble in a liquid as

$$\frac{d(E_{e,l}+E_{k,l}+E_{k,g})}{dt} + \frac{p_{g,0}V_{g,0}^\gamma}{\gamma-1}\frac{dV_g^{1-\gamma}}{dt} = -\int_I \sigma\kappa\mathbf{u}_I\cdot\mathbf{n}_I dS + (p_g - p_\infty)\frac{dV_g}{dt} - (\phi_{D,l}+\phi_{D,g}), \tag{2.47}$$

Equation 2.47 mathematically shows various energy exchanges that take place during the expansion and collapse of a cavitation bubble. The terms $(\phi_{D,l}+\phi_{D,g})$ are always positive as some energy is always dissipated due to irreversible effects.

If $p_\infty$ is constant, we can integrate the equation 2.47 in time, and further using a definition for total dissipation as $\Phi_D = \int_t \phi_{D,l}dt + \int_t \phi_{D,g}dt$, we obtain the final form as

$$\boxed{E_{e,l}+E_{k,l}+E_{k,g}+E_s+\frac{p_{g,0}V_{g,0}^\gamma}{\gamma-1}dV_g^{1-\gamma} - (p_g-p_\infty)dV_g = -\Phi_D + E_0,} \tag{2.48}$$

where $E_0$ is the integration constant which can be computed from the energy at the reference state and

$$E_s = \int_t\int_I \sigma\kappa\mathbf{u}_I\cdot\mathbf{n}_I dSdt$$

is the surface energy. Using

$$\int_I \kappa \mathbf{u}_I \cdot \mathbf{n}_I dS = -\int \nabla_s \cdot \boldsymbol{u} dS + \int \boldsymbol{u} \cdot \boldsymbol{p} dl$$

with $\boldsymbol{p} = \boldsymbol{n} \times \boldsymbol{t}$ and $\boldsymbol{t}$ the tangent to the surface at the interface contour considered (see reference [110]), it is easy to show that in the case of a bubble that is not in contact with the wall the surface energy reduces to $E_s = \sigma S_I$. Otherwise, the surface energy cannot be explicitly integrated and we need to account for the energy associated to the contact of both phases with the solid wall. In absence of dissipation and for an incompressible liquid, this equation can be cast in the form of

$$E_k + E_p = E_m$$

where $E_m$ is the mechanical energy of the system which is constant and $E_p$ is the potential energy of the system at a given state that depends on the bubble geometrical parameters (volume, surface...).

## 2.5 Relevant non-dimensional numbers

Finally, we introduce the relevant non-dimensional numbers that will be used in next chapters to characterize the problem. We consider that the shape of initial bubble/nuclei is spherical cap (figure 2.4) which is motivated by the fact that for a spherical cap the bubble geometry is defined only by two parameters, the bubble radius of curvature $R_{c,0}$ and the contact angle $\alpha$. This simplifies the discussion of the results compared to more complex shapes (e.g. ellipsoids) that could be focus of future investigations. We consider the three-dimensional Rayleigh problem where the bubble/nuclei is in thermodynamic equilibrium with the surroundings and the pressure far from the bubble $p_\infty$ is changed suddenly for infinite time. In the context of bubble nucleation by ultrasound waves, this is equivalent to case where characteristic frequency of the ultrasound pulse is small as compared to the natural frequency of the bubble $\frac{\omega_p}{\omega_b} \ll 1$. This situation is also analogous to the collapse of low pressure bubble formed at the end of expansion phase which collapses at the constant ambient pressure. We also assume that the time scales for the diffusion of heat and mass are very large compared to the characteristic time of bubble response i.e. $\frac{\omega_p R_{c,0}^2}{D} \ll 1$, where D is Fickian constant for diffusion.

In this framework, the general response of a bubble to pressure change depends upon the initial radius of curvature $R_{c,0}$, the contact angle $\alpha$, the liquid pressure just outside the bubble at equilibrium state $p_{L,0}$, time $t$, pressure far from the bubble $p_\infty$, the densities of liquid and gas phase $\rho_l$ and $\rho_g$ respectively, $\mu_l$ and $\mu_g$ i.e. the dynamic viscosity of liquid and gas phase respectively, $\sigma$ the surface tension force per unit length for the liquid and gas pair, and finally $c_l$ the speed of sound in the liquid phase. Note that the initial gas pressure $p_{g,0}$ is related to ambient pressure at equilibrium state via Laplace law i.e. $p_{g,0} = p_{L,0} + \frac{2\sigma}{R_{c,0}}$. Let bubble volume $V$ at time $t$ can be represented as some functional relation

$$V(t) = \mathcal{F}(p_\infty, p_{L,0}, \rho_l, \rho_g, \mu_l, \mu_g, \sigma, R_{c,0}, \alpha, c_l), \tag{2.49}$$

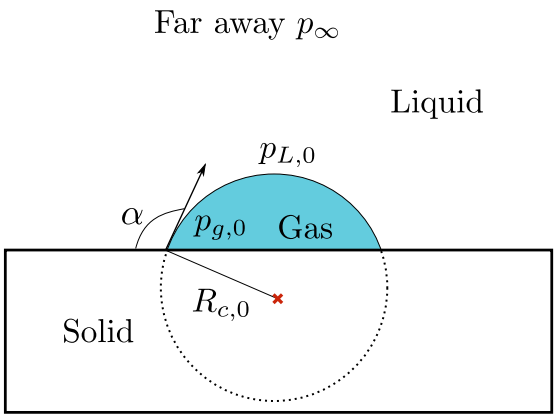


Figure 2.4: The setup for studying bubble dynamic problems, at equilibrium position $p_\infty = p_{L,0}$, for expansion $p_\infty < p_{L,0}$ and for collapse $p_\infty > p_{L,0}$

There are eleven dimensional parameters controlling the problem and the three fundamental dimensions upon which the solution depends. The Buckingham Π theorem implies that there are eight independent non dimensional parameters relevant for the problem, therefore the non-dimensional bubble volume ($V^*$)

$$V^*(t^*) = \mathcal{G}(p^*, \rho^*, m, Re, We, Ma, \alpha),$$

where

$$t^* = \frac{tU_c}{R_{c,0}}, \quad p* = \frac{p_\infty}{p_{L,0}}, \quad \rho^* = \frac{\rho_l}{\rho_g}, \quad m = \frac{\mu_l}{\mu_g}$$

$$Re = \frac{\rho_l U_c R_{c,0}}{\mu_l}, \quad We = \frac{\rho_l U_c^2 R_{c,0}}{\sigma}, \quad Ma = \frac{U_c}{c_l}, \quad \alpha.$$

The Reynolds number ($Re$) is the ratio of inertial to viscous forces and Weber number ($We$) is the ratio of inertial and the surface tension forces. When discussing the contact line dynamics, it is common to use the capillary number ($Ca$) and the Ohnesorge number ($Oh$) defined as

$$Ca = \frac{\mu U_c}{\sigma}, Oh = \frac{\mu}{\sqrt{\rho_l \sigma R_{c,0}}}$$

from which the Reynolds and Weber number can be eventually obtained as

$$Re = \frac{Ca}{Oh^2} \quad We = \frac{Ca^2}{Oh^2}.$$

Both, capillary and Ohnesorge number compare viscous and surface-tension effects in a dynamic and static configuration. Note that the capillary number is defined using a characteristic velocity and Ohnesorge number is defined using a characteristic length. Hence, for a given system with fixed physical properties, the capillary number depends only on the pressure difference (driving the bubble) and not on the size of the bubble, while the Ohnesorge number is given by the size

and is not influenced by the pressure difference. For the sake of simplicity, we fix the value of density ratio $\rho^* = 10^3$, viscosity ratio $m = 10^2$ and Mach number $Ma = 0.003$. These are not changed throughout the manuscript unless explicitly mentioned.

Note that $U_c$ is the characteristic velocity of a given problem. We define $U_c$ differently in each chapter: In chapter 3, we will take $U_c = \sqrt{2/3|p_\infty|/\rho_l}$ as this velocity represents the asymptotic growth rate of a spherical bubble in a low pressure environment obtained from the RP model. In chapter 4, we will use $U_c = \sqrt{p_\infty/\rho_l}$ which is the collapse velocity of a low pressure bubble under the action of ambient pressure. In chapter 5, we will use a wave of amplitude $\Delta p$ to excite the bubble, which introduces a characteristic velocity $U_c = \sqrt{\Delta p/\rho_l}$.

# 3 Heterogeneous bubble nucleation

Bubble nucleation is the primary aspect of cavitation and an integral part of understanding the collapse dynamics of the bubbles as it depends upon the bubble history and nucleation dynamics. In this chapter, we focus on the process of heterogeneous nucleation in which bubbles appear heterogeneously and spatially biased towards the solid walls/impurities. We approach the problem from the lenses of Computational Fluid Dynamics (CFD) in order to understand the effect of forcing and wall properties on the dynamics of the bubbles during first instants of the nucleation process.

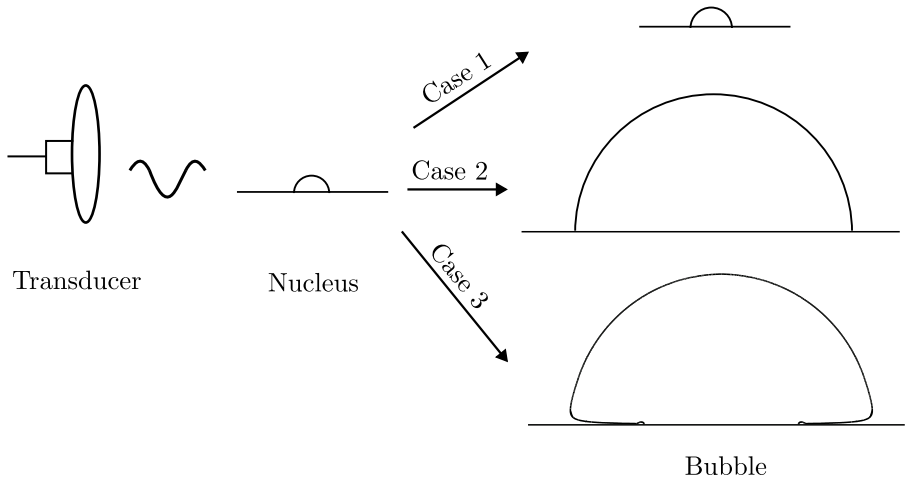


Figure 3.1: The schematic diagram for the different scenario of how a nucleus can respond to the ultrasound pressure drop. These three cases will discussed in detail in this chapter.

In figure 3.1, we schematically show three representative situations which can arise when a gas nuclei is exposed to pressure forcing. In this chapter, we investigate these three cases in detail as a function of the following control parameters: the size of nuclei, the shape of nuclei, the amplitude and frequency of the pressure forcing. In the first case, the nuclei remains stable and does not grow explosively to a large bubble. In second case, the bubble becomes unstable and therefore grows explosively, a liquid microlayer does not from underneath the bubble. In the third case, the bubble grows explosively and a liquid microlayer is formed underneath the bubble. We aim to understand the range of control parameters in non-dimensional space that favor these situations. We solve for the Rayleigh-problem as mentioned in chapter 2 where we assume that the pressure far from the bubble decreases suddenly and is kept at a low value for infinite time, and the effect of a finite pulse duration will be briefly discussed in section 3.1.3 for the spherical bubble case.

## 3.1 Nucleation threshold

In the heterogeneous nucleation, the bubbles can appear from the air nuclei trapped in the solid impurities when the pressure falls below a critical value [73, 75]. This process is analogous to the spherical bubble in the bulk of liquid suddenly exposed to low pressure. The response of a spherical bubble to the pressure drop can be stable or unstable depending upon the critical pressure corresponding to the bubble size. A stable bubble grows only slightly whereas an unstable bubble grows explosively to very large volume (few orders of magnitude). This phenomenon is very well illustrated for spherical bubbles in the film notes of national committee for fluid mechanics films [143]. The unstable situation arises when the expanding forces (eg. the pressure inside the bubble, liquid inertia) becomes greater than the collapsing forces (eg. liquid pressure, the surface-tension forces) acting on the bubbles. Similarly, an air nuclei trapped in the solid impurities can also become unstable if the pressure drops below the critical threshold referred to as the nucleation threshold. This process of bubbles appearing from the nuclei attached to wall as the pressure drop below the nucleation threshold is called heterogeneous nucleation. This phenomenon is experimentally illustrated by Borkent et. al. [80]. In this section, we theoretically and numerically predict the nucleation threshold for the spherical cap shaped nuclei attached to the wall as a function of bubble size $(R_{c,0})$, contact angle $(\alpha)$, and the boundary condition for the motion of contact line.

### 3.1.1 Theoretical predictions of the bubble nucleation threshold

The theoretical developments for the prediction nucleation threshold rely on the assumption of quasi-static bubble growth [73, 75, 80]. The quasi-static evolution of bubble is given by the Laplace equation which is given as following

$$p_\infty = p_{g,0}\left(\frac{V_0}{V_b}\right)^\gamma - \sigma\kappa, \tag{3.1}$$

where $V_b$ is the instantaneous bubble volume, $V_0$ is the initial bubble volume and $p_{g,0}$ is the initial gas pressure, $\rho_l$ is the density of liquid phase, $\sigma$ is surface tension between liquid and gas phase, $\gamma$ is the polytropic coefficient, $p_\infty$ is the liquid pressure far away from the bubble and $\kappa$ is the local curvature. Note that we have assumed an adiabatic bubble expansion in order to write above equation. For the sake of simplicity, we restrict ourselves to the cases where curvature remains uniform so that we can write $\kappa = 2C_\kappa/V_b^{1/3}$. For instance $C_\kappa = (4/3\pi)^{1/3}$ for a spherical bubble while for spherical cap $C_\kappa = g(\alpha)^{1/3}$ where $g(\alpha)$ is a function of contact angle $(\alpha)$ of spherical cap with the solid wall given as $(\frac{\pi}{3}(2+3\cos(\alpha)-\cos^3(\alpha)))$. In such a scenario the dimensional Laplace equation is

$$p_\infty = p_{g,0}\left(\frac{V_0}{V_b}\right)^\gamma - 2\sigma C_\kappa \frac{1}{V_b^{1/3}}, \tag{3.2}$$

Let us write the non-dimensional form of the equation 3.2 using following non-dimensional variables: $\sigma^* = \sigma C_\kappa/p_{L,0}V_0^{1/3}$, $V^* = V_b/V_0$, $p_\infty^* = p_\infty/p_{L,0}$

$$p_\infty{}^* = (1 + 2\sigma^*)\left(\frac{1}{V^*}\right)^\gamma - \frac{2\sigma^*}{V^{1/3}}, \tag{3.3}$$

where $p_{L,0}$ as is the equilibrium pressure in the liquid just outside the bubble given by Laplace law as $p_{L,0} = p_{g,0} - 2\sigma/V_0^{1/3}$ at equilibrium state. For fixed system of liquid and gas the non-dimensional number $\sigma^*$ characterize the initial volume of the the nuclei.

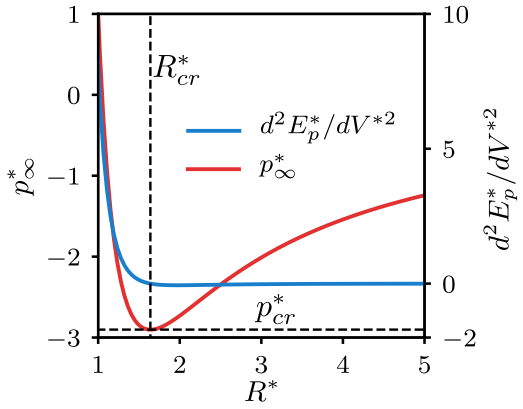


Figure 3.2: The non-dimensional Laplace pressure and second derivative in non-dimensional potential energy w.r.t bubble volume is plotted against radius of bubble for quasi-static expansion of a spherical bubble and representative case of $1/\sigma^* = 0.32$.

We begin by discussing the well known case of the spherical bubble evolution such that the non-dimensional bubble radius $R^* = V^{*1/3}$. In figure 3.2, we show the bubble radius evolution as a function of far field pressure as given by eq. 3.3 for $1/\sigma^* = 0.32$. The point $(p^*_\infty = 1, R^* = 1)$ is initial equilibrium position of bubble, as the pressure decreases (quasi-statically) the bubble expands to a new equilibrium radius until the far field pressure reaches a critical threshold value ($p^*_{cr}$ in figure 3.2) below which no equilibrium position exists anymore. Any small pressure drop beyond this point leads to sudden, unstable expansion of the bubble. This threshold can be found by minima of equation 3.3 and is given as

$$p^*_{cr} = -\left(\frac{3}{2\sigma^*}\gamma(1 + 2\sigma^*)\right)^{\frac{1}{1-3\gamma}} 2\sigma^*\left(1 - \frac{1}{3\gamma}\right). \tag{3.4}$$

Note that the critical pressure beyond which the bubble expansion is unstable is characterized by a critical value of the bubble radius given as

$$R^*_{cr} = \left(\frac{3}{2\sigma^*}\gamma(1 + 2\sigma^*)\right)^{3\gamma-1}, \tag{3.5}$$

which is also shown in figure 3.2 with the black line. Since this threshold was first identified by Blake [76] these are also called Blake's radius and Blake's threshold respectively.

The stability of the bubbles can also be discussed by considering the energy equation 2.48 which in the case of reversible quasi-static evolution of bubble with uniform curvature reduces to

$$\frac{p_{g,0}V_0^{\gamma}}{\gamma-1}V_b^{1-\gamma} = -3\sigma C_\kappa V_b^{2/3} - p_\infty V_b + E_0. \tag{3.6}$$

In this case, the potential energy is

$$E_p = \frac{p_{g,0}V_0^{\gamma}}{(\gamma-1)}(V_b)^{1-\gamma} + 3\sigma C_\kappa (V_b)^{2/3} + p_\infty V_b, \tag{3.7}$$

which can be cast in to the non-dimensional form as

$$E_p^* = \frac{1+2\sigma^*}{\gamma-1}(V^*)^{1-\gamma} + 3\sigma^*(V^*)^{2/3} + p_\infty^* V^*, \tag{3.8}$$

where $E_p^* = E_p/p_{L,0}V_0$. The sign of second derivative of the potential energy w.r.t volume gives the stability condition for the bubble (see reference [79]). The bubble is unstable if the $d^2E_p/dV_b^2 < 0$, where

$$\frac{d^2E_p^*}{dV^{*2}} = \gamma(1+2\sigma^*)V^{*-1-\gamma} - \frac{2}{3}\sigma^* V^{*-4/3}, \tag{3.9}$$

In figure 3.2, we plot the evolution of second derivative for a particular case of spherical bubble where we clearly see that for bubble size larger than critical bubble size the second derivative of energy is negative while it is positive otherwise. We can also obtain the critical bubble size by solving equation $d^2E_p^*/dV^{*2} = 0$ which yields same criterion as equation 3.4.

The criterion obtained above (equation 3.3 and 3.9) can be easily extended for spherical cap shaped bubble nuclei attached to a homogeneous wall. In classical nucleation theories, this represents the case of nuclei that has moved out of the crevice and also the case in which the nuclei volume is much larger than the volume of any irregularity present in the wall so that the bubble can be assumed to lie in a flat surface. We further assume that the bubble nuclei remains as a spherical cap during the first instants before the bubble enters into an unstable regime. The geometry of a spherical cap is defined by two independent parameters: we choose radius of curvature ($R_c$) and angle of contact with solid ($\alpha$), such that the bubble volume is $V_b = R_c^3 g(\alpha)$. The Laplace equation for a spherical cap bubble is

$$p_\infty = p_{g,0}\left(\frac{R_{c,0}^3 g(\alpha_0)}{R_c^3 g(\alpha)}\right)^{\gamma} - \frac{2\sigma}{R_c}, \tag{3.10}$$

where $R_{c,0}$ and $\alpha_0$ are the parameters that controls the bubble shape and size and hence the Laplace pressure. Furthermore, we impose an additional constraints to describe the motion of the contact line in order to reduce the problem into a single variable minimization problem. Here, we impose the conditions corresponding to two limiting scenarios a) The free slip boundary condition which imposes that the contact line moves freely and maintains a constant angle of contact therefore $\alpha = \alpha_0$, where $\alpha_0$ is the initial contact angle b) The no-slip/pinning boundary condition which imposes that the contact line is pinned at the initial location and it does not moves, in this situation $R_c \sin(\alpha) = R_{c,0}\sin(\alpha_0)$ at all the times. Under these conditions, it is possible to

numerically find the minima of equation 3.10 subjected to pinning and free slip boundary condition. In figure 3.3, we plot the critical pressure as a function of the initial radius of curvature and the contact angle for air bubbles at normal temperature and pressure conditions. The panel $a$ and $b$ correspond to free slip and no slip boundary condition.

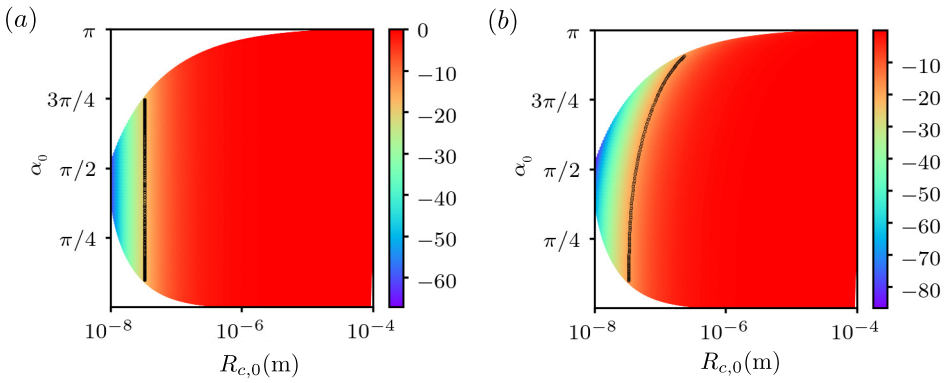


Figure 3.3: The critical pressure drop required for unstable growth of spherical cap shaped air bubbles in contact with rigid wall and in water at normal temperature and pressure conditions. The critical pressure drop predicted from minima of equation 3.10 (colormap) is shown for several bubble shapes and size are characterized by radius of curvature $R_{c,0}$ and contact angle $\alpha_0$. An isobar for $p_{cr} = -2$MPa is also shown with the black curve. The bubbles in panel $(a)$ are subjected to free slip boundary condition whereas in panel $(b)$ are subjected to pinning boundary condition for motion of contact line.

The differences between values reported in figure 3.3$a$ and $b$ reveal that the nucleation threshold depends on boundary condition for the motion of contact line for certain range of bubble sizes. In case of the free-slip boundary condition, the critical pressure for the nucleation is independent of the contact angle (also predicted previously by Atchley and Prosperetti [75]), while in the case of pinned bubbles the contact angle introduces a correction that becomes significant for small bubbles and large contact angles. The isobar for the pressure drop of $p_{cr} = -2$MPa is also shown with black dots in figure 3.3$a$ and $b$. All the bubbles whose initial sizes lie on the left of this isobar (black curve) are stable, whereas all the bubbles which lie on the right of this curve are unstable if $p_\infty = -2$MPa. In other words, figure 3.3 characterizes (for given pressure drop) the size of nuclei active for nucleation among several nuclei that can be present on a wall. The differences between the isobars between the figure 3.3$a$ and $b$, indicate the regions where the stability depends on the boundary conditions.

### 3.1.2 Numerical predictions of the nucleation threshold

The theory of heterogeneous bubble nucleation presented above imposes certain conditions (e.g. inertial effects are neglected) that need to be verified numerically. In this section, we use DNS to obtain the critical pressure drop beyond which the bubble becomes unstable. We solve for the Rayleigh problem where the pressure far from the bubble is assumed to be dropped suddenly to a lower value $p_\infty < p_{L,0}$ and kept constant. In such conditions, an unstable bubble will keep on growing for infinite amount of time (here, till the end of simulation) whereas a stable bubble

will expand to new equilibrium and oscillate around the new equilibrium position due to inertia and viscosity. We start by presenting a simple case of spherical bubble in the bulk of liquid. Later, we show numerical results for spherical cap bubbles evolving in contact with wall to explain the pinning effect in detail. We also present results for expansion of spherical bubble subjected to time varying pressure field to show the effect of finite duration of pulse.

### Single spherical bubble in bulk of liquid

The numerical setup for the problem is shown in figure 3.4*a*. The simulation domain is 3D axi-symmetric with left boundary as the axis of symmetry. The size of domain is 100 times the initial bubble radius. The set of non-dimensional parameters used to setup the problem are given in table 3.1. The liquid pressure field at $t = 0$ is initialized as solution to Rayleigh problem at equilibrium position ($R = R_0$) such that at any location $r$ initial pressure, $p_{r,0} = p_\infty + (p_{L,0} - p_\infty)\frac{R_0}{r}$. When the external pressure is lower than the initial bubble pressure, $p_\infty < p_{L,0}$, bubble expands, in figure 3.4*b* we show the evolution of bubble radius for two values of the pressure drop slightly above and below the critical value predicted by equation 3.4 for $1/\sigma^* = 0.32$. The red line shows the case where $p_\infty/p_{cr} > 1$ and the bubble grows explosively till the end of simulation whereas the green line shows the evolution of a bubble when $p_\infty/p_{cr} < 1$ and as expected the bubble oscillates around the new equilibrium radius.

| $\rho_l/\rho_g$ | $\rho\sqrt{p_{L,0}/\rho_l}R_0/\mu$ | $1/\sigma^* = p_{L,0}R_0/\sigma$ | $c_l^* = \sqrt{\rho_l c_l^2/p_{L,0}}$ | $p_{cr}/p_{L,0}$ |
|---|---|---|---|---|
| 1000 | $\infty$ | $\in \{0.16, 0.24, 0.32, 0.64\}$ | 0.05 | -2.9 |

Table 3.1: Non-dimensional parameters used for simulations of spherical bubble expansion

To numerically predict the dependence of critical pressure drop on the bubble size (represented with $\sigma^*$ for given gas-liquid pair), we perform similar numerical simulations changing the pressure drop and $1/\sigma^*$. In figure 3.4*c*, each point corresponds to one numerical simulation, the case where the bubble expands unstably are shown with red crosses and the case where the bubble oscillates stably about new equilibrium radius are shown with green circles. The critical pressure drop given by the quasi-static theory (equation 3.4), shown with the dashed line, indicate that the numerical results agree well with the theoretical estimates. The numerically obtained threshold for unstable growth is slightly under-predicted in comparison to the theoretical estimates because of the inertial effects which promote the bubble growth and thus bubbles attain the critical size at slightly higher pressure and become unstable. Note that the inertial effects were neglected while deriving the quasi-static theory.

### Bubbles attached to wall

We use similar procedure to predict the numerical threshold for bubbles attached to wall with different contact angle $\alpha_0$. In the theoretical model, the bubble shape remains spherical cap and therefore $\alpha_0$ is a geometric parameter that defines the shape of the bubble. For DNS, this angle $\alpha_0$ is set as the boundary condition at the smallest grid size $\alpha_\Delta$. The numerical setup is shown in figure 3.5*a* and the dimensionless parameters are same as table 3.1. We start by imposing free slip

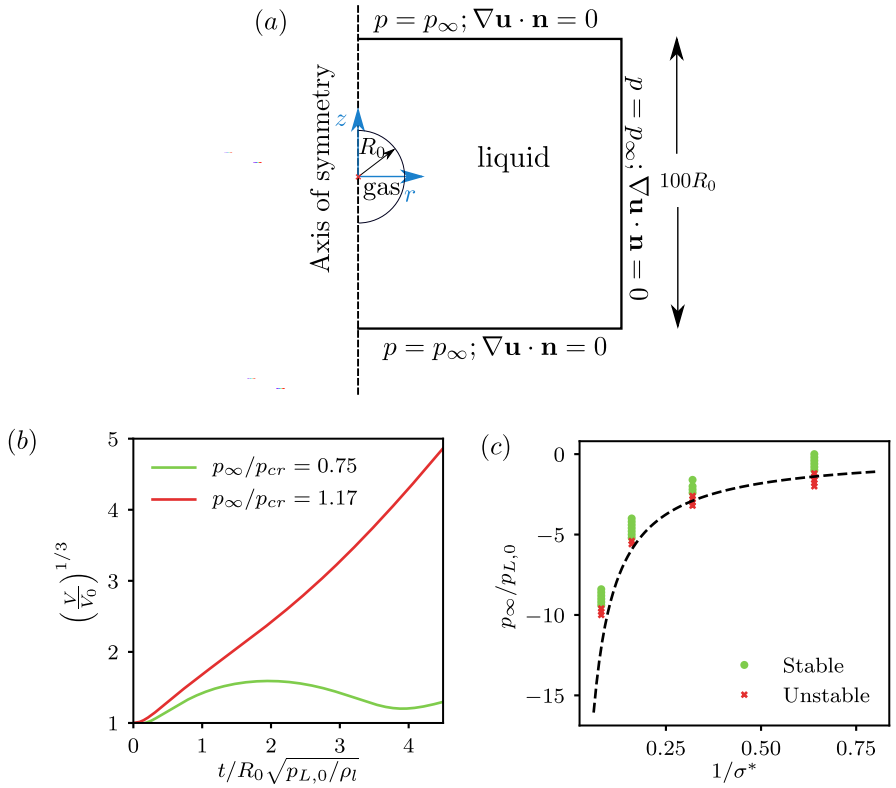


Figure 3.4: ($a$) The numerical setup for the single bubble expansion liquid bulk ($b$) Radius evolution for spherical bubble exposed to pressure slightly more than and less than the critical pressure in the case $1/\sigma^* = 0.32$ ($c$) The numerical prediction of critical pressure drop for transition form stable to unstable behavior shown for different bubble sizes characterized by $\sigma^*$

boundary condition at the wall thus the contact line moves with the initially imposed contact angle the angle that remain constant throughout the simulation. Similar to the spherical bubble case, we vary $p_\infty$ close to the critical pressure drop predicted with the quasi-static theory. In figure 3.5$b$, we show the temporal evolution of the dimensionless bubble equivalent radius $(V/V_0)^{1/3}$ for several pressure drops. Consistent with the spherical bubble case, the numerical obtained threshold is slightly lower than the theoretical predictions (minima of equation 3.10).

An important conclusion from figure 3.3 is that in the limiting case when the bubble expands with constant contact angle ($\alpha = \alpha_0$), the nucleation threshold is independent of angle of contact and is function of radius of curvature $R_{c,0}$ only. We verify this with numerical simulations for bubbles with same $R_c$ and varying contact angle $\alpha$ (see figure 3.5$c$). Analogous to the theoretical curve (black dashed line) the numerical predictions are shown to be horizontal lines independent of the contact angle $\alpha$ and are slightly under-estimated due to inertia.

### Pinning effects

We have predicted in figure 3.3 that the boundary condition at the wall alters the nucleation threshold and pinning of contact line can act as a stabilizing mechanism for the nuclei. In fig-

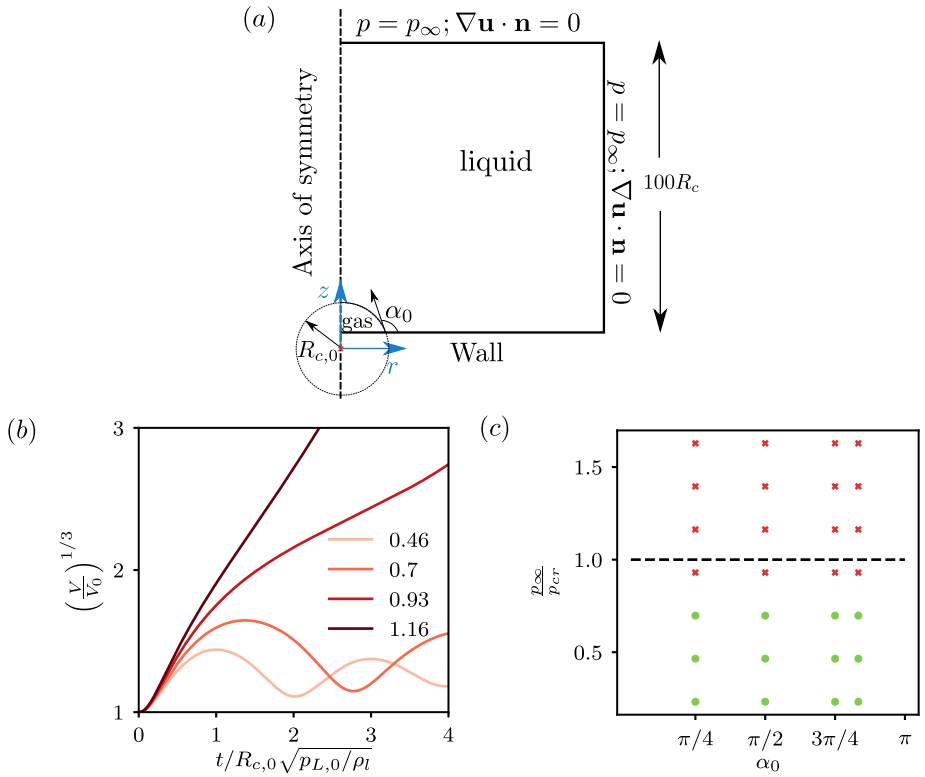


Figure 3.5: ($a$) The numerical setup for simulations for expansion of bubbles attached to wall. ($b$) The evolution of dimensionless bubble volume for representative bubble with $\alpha = 150°$ and $R_{c,0}\sigma/p_{L,0} = 1.4$ for different pressure drops compared the critical pressure drop $p_\infty/p_{cr}$ shown in legend. ($c$) The numerical predictions of critical pressure drop for bubbles with different contact angles, the unstable bubbles are shown with red points where as the stable ones with green, black dash line corresponds to critical pressure drop predicted from equation 3.10.

ure 3.6$a$, we plot the isobars for the critical pressure $p_{cr}/p_{L,0} = -0.86$ (obtained for $\sigma^* = 1$) for both pinning and free slip boundary conditions. We can identify the following three regions:
Region $i$: where the bubbles are stable irrespective of the behavior of the contact line.
Region $ii$: where the stability of the bubble depends on how the contact line moves at the wall and thus numerically its response is sensitive to the boundary condition imposed at the wall.
Region $iii$: where the bubbles are always unstable and grow explosively irrespective of the response of the contact line.

| $\rho_l/\rho_g$ | $p_{cr}/p_{L,0}$ | $1/\sigma^*$ | $\rho\sqrt{p_{L,0}/\rho_l}R_0/\mu$ | $\sqrt{\rho_l c_l^2/p_{L,0}}$ |
|---|---|---|---|---|
| 1000 | 0.86 | 1.4 | 10 | 0.05 |

Table 3.2: The dimensionless parameters for predicting thresholds of bubbles attached to wall

To demonstrate the effect of boundary condition numerically, we choose a representative bubble from region $ii$ given by $R_{c,0}p_{L,0}/\sigma = 1.4$ and $\alpha = 2\pi/3$ (red cross in figure 3.6$a$). We

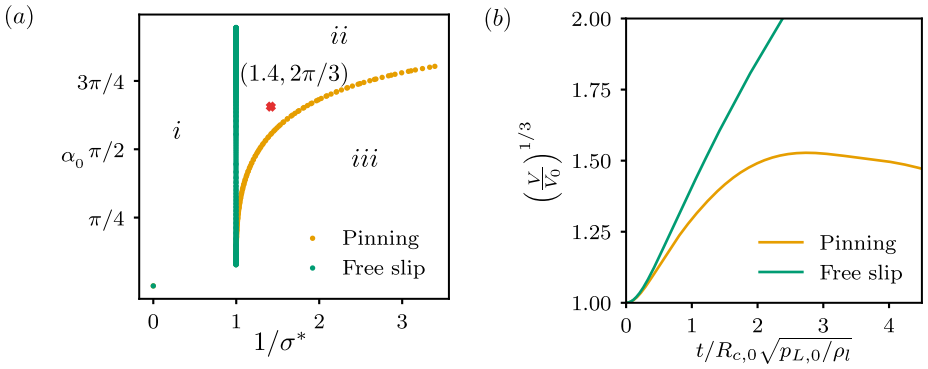


Figure 3.6: $(a)$ Isobars for critical pressure drop of $p_{cr}/p_{L,0} = -0.86$ for bubbles subjected to the two limiting boundary conditions for motion of contact line, the red point is chosen as representative of intermediate region where the stability of bubble depends on the boundary condition. $(b)$ The DNS results for evolution of bubble volume for a bubble from intermediate region (red point in figure 3.6$a$) subjected critical pressure drop and the limiting boundary conditions.

numerically simulate the growth of this bubble at critical pressure drop in the two limiting situations of contact line boundary conditions and for parameters given in table 3.2. The pinning effect is introduced in the code by putting zero velocities and pressure gradients in cells next to wall. The actual situation of contact line motion may be in middle of these two extreme cases considered here, this test only aims to demonstrate that the wall boundary condition can influence the threshold for bubble nucleation. The evolution of the dimensionless equivalent radius in these limiting conditions is shown in figure 3.6$b$. As expected the bubble behaves unstably when using the free slip boundary condition but it is stabilized when the contact line is pinned and thus oscillates about the new equilibrium shape/size.

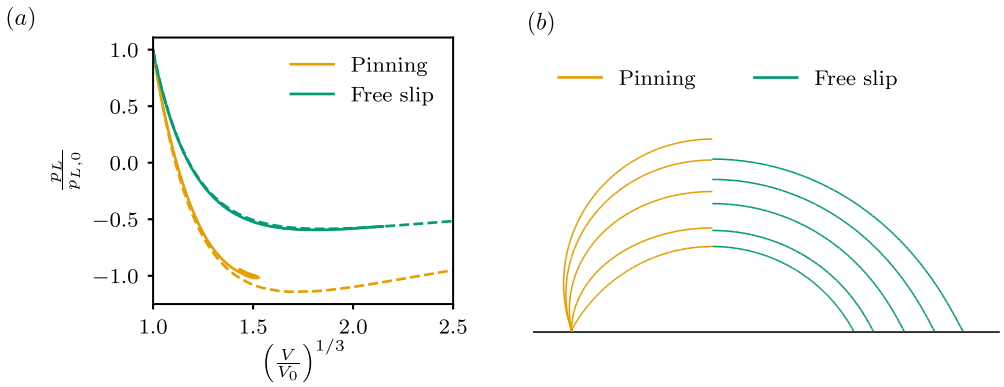


Figure 3.7: The comparison is drawn between same bubble ($p_{L.0}R_{c,0}/\sigma = 1.4, \alpha = 2\pi/3$) subjected to same pressure drop but different limiting boundary conditions. $(a)$ The evolution of Laplace pressure with the bubble volume obtained from the DNS shown with the thick lines and the dashed line is obtained from the quasi-static theory. $(b)$ The interface contours obtained from DNS at various instances of time where left half is the case of pinning boundary condition and right half is the case of free slip boundary condition.

The effect is more evident from the evolution of Laplace pressure in these limiting situations (see figure 3.7). Note that the liquid pressure at the interface ($p_L$) is computed using the Laplace law while assuming that the gas pressure is uniform and equal to average pressure in the bubble. Because the bubbles evolve as spherical caps, the liquid pressure outside the interface is also uniform. The dashed lines are obtained from quasi-static theory (equation 3.10) and the thick lines from direct numerical simulations. The pinned bubble does not reach the minima in the Laplace curve and oscillates in the stable part of the diagram. When the same bubble was subjected to a free slip boundary condition the bubble size exceeds the critical size and advance into the unstable growth regime. In figure 3.7*b*, we show the bubble evolution in these two situations by plotting bubble shapes as obtained from DNS for visual depiction of the numerical experiments. We choose the limiting cases i.e. the pinned contact line and infinite slip whereas the contact line dynamics lies in the the gray area between these two extreme conditions therefore in reality the critical threshold is expected to lie somewhere in the region $ii$ (of figure 3.6$a$) depending up on the mobility of the contact line.

### 3.1.3 Finite pulse duration effects

In the previous sections, we have assumed that the bubble is suddenly exposed to a low pressure for infinite amount of time (zero frequency case). In reality the pressure is dropped gradually by an external source (eg. transducer in reference [80]) and then recovered back to the ambient condition. In this case, the ratio of time scale associated with external excitation and the natural time period of the bubble oscillation can influence the bubble nucleation event. To mimic the physical situation of ultrasound cavitation, we set up a test cases where the bubble is excited by a linear and planar Gaussian perturbation in ambient pressure. Figure 3.8$a$ shows the setup for this case where the color scale represent the pressure field in the domain and the inset view shows the initial bubble. The simulations are axisymmetric about the bottom boundary and the pressure perturbation is given as $p_L/p_{L,0} = 1. - p_m/p_{L,0} e^{-\left(\frac{t+t_0}{T_p}\right)}$ where $p_m$ is the maximum gauge pressure of the pulse. This pulse travels towards the bubble with the speed of sound, hence the pressure around bubble is lowered for a characteristic time $T_p = 6S_g/c_l$ where $S_g$ is the standard deviation of the Gaussian perturbation and $c_l$ is speed of sound.

Although a Gaussian perturbation is not a wave we define the parameter $F_R$ analogous to frequency ratio in the classical case of bubble oscillations as

$$F_R = \frac{1}{t_p} \frac{R_0}{\sqrt{3\gamma p_{g,0}/\rho_l}},$$

such that $F_R \to 0$ corresponds to sudden pressure drop for infinite time. We perform parametric study for several values of $p_m$ close to the critical pressure and for $F_R \in \{0.08, 0.25, 0.8\}$ and show the maximum bubble radius $R_{max}$ in figure 3.8*b* with dots. The dashed lines correspond to the results from Rayleigh-Plesset model and the color code gives the amplitude of wave compared to critical pressure predicted from the quasi-static model ($-p_m/p_{cr}$). When $F_R > 1$ the bubble pressure is not lowered for enough time to over come the inertia of the heavier liquid around the bubble interface and the bubble growth is insignificant, as $F_R$ decreases and pressure is lower

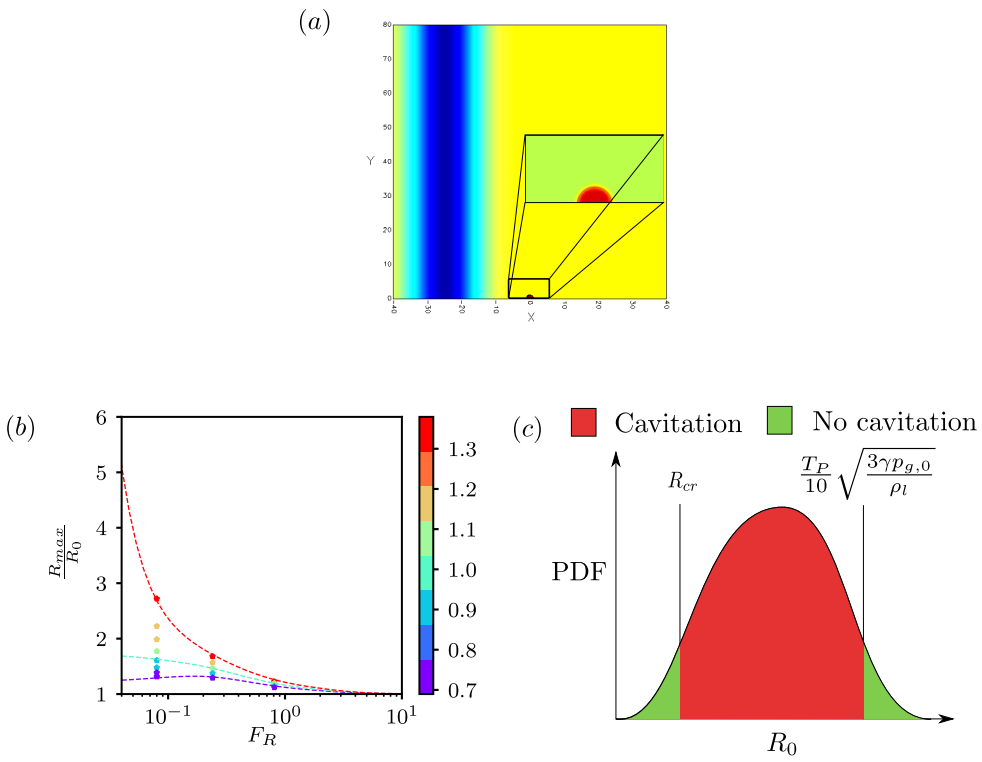


Figure 3.8: $(a)$ Setup for studying bubble expansion from Gaussian pressure perturbation $(b)$ Max radius plotted against $F_R$ for several pressure amplitude for different $p_\infty/p_{cr}$ shown with the colormap $(c)$ Bubble population active for cavitation depending upon the initial bubble radius and the two limiting criterion posed by surface tension forces (equation 3.5) and finite pulse duration.

than the critical pressure and the bubbles show explosive growth. Thus, there is a limit for $F_R$ to observe significant cavitation which is $F_R \approx 0.1$ in this case.

There are two important criterion for bubble size to observe unstable growth for a given ultrasound pulse i.e. fixed amplitude of perturbation and the characteristic time. Equation 3.5 shows that for known equilibrium pressure and gas-liquid pair $\sigma^*$ represents all the initial nuclei sizes that are present in the problem and in the low frequency limit bubbles nucleate when $R_0 > R_{cr}$. On other hand, we have seen that transient effects imply that to observe significant bubble growth, we need to satisfy $F_R < 0.1$, which implies that $R_0 < \sqrt{\frac{3\gamma p_{g,0}}{\rho_l}}\frac{T_p}{10}$. These two conditions are illustrated in figure 3.8$c$ where some probability distribution function of nuclei size is plotted against the nuclei sizes that may exist. All the bubbles active for cavitation are shown in red color and inactive bubble sizes in green. Arguably, if $F_R$ of pulse is such that the two constraints overlap any significant bubbles are not observed independent of amplitude of this pulse.

## 3.2 Unstable bubble growth and microlayer formation

The discussion on bubble nucleation in the previous section (except section 3.1.2) has been focused on the inviscid flow dynamics such that the contact line could move freely. The viscous effects introduce the resistance to the motion of contact line and may result in the formation of a microlayer (case 3 in figure 3.1). In this section, we investigate the dynamics of microlayer formation during the growth of the unstable bubbles in the Rayleigh problem using the Navier slip model for the contact line motion (see section 2.3). This model has been extensively used to mimic the contact line motion in references [137, 138, 139]. We use the set up described in figure 3.5. For the ease of representation, we use $\alpha$ instead of $\alpha_\Delta$ for the numerical contact angle which can be different form the actual microscopic equilibrium contact angle $\alpha_e$ in a physical setup. It is well known that in the Rayleigh problem the bubble expands at an asymptotic rate given as $\dot{R} = \sqrt{\frac{2}{3}\frac{\Delta p}{\rho_l}}$, which can be estimated by neglecting the acceleration term in Rayleigh–Plesset model [144]. In this section, we choose this asymptotic growth rate as characteristic velocity of the problem $U_c = \sqrt{\frac{2}{3}\frac{\Delta p}{\rho_l}}$, where $\Delta p = p_{L,0} - p_\infty \approx |p_\infty|$ is the effective pressure drop that the bubble experiences.

The viscous effects are generally concentrated near the wall within the viscous boundary layer whose thickness scales with $\sqrt{\nu t}$ where $\nu$ is the kinematic viscosity and $t$ is the time. Therefore the problem of bubble nucleation is intrinsically a multiscale problem similar to other contact line problems studied extensively in past such as boiling, plunging/pulling plate, spreading drops/bubbles etc [130, 131, 145, 146, 147]. In figure 3.9, we show a particular example of an unstable bubble expansion in a low pressure liquid, where the non-dimensional velocity field is shown with the colormap as $|\mathbf{u}|/U_c \in (0, 1)$, the mesh is shown in the background with gray color. We can readily recognize the multiscale nature of the problem. Three different regions based on the length scales can be identified where the dynamics can differ significantly from each other. These are discussed as following

- At large length scales i.e. comparable to the bubble size generally greater than a few microns, the bubble dynamics is mainly governed by the liquid inertia effects, surface-tension only plays secondary role during the first instants after the nucleation. The viscous effects are negligible in this region as this region generally lies outside the viscous boundary layer.

- At an intermediate length scale, generally ranging few hundred nano meters to few microns close to the wall, the dynamics is governed by the complex interplay between the viscous and the surface tension stresses, the interface is highly curved and the thin film equations are often used to model the dynamics in this region.

- Finally, at scales smaller than few hundred nano meters, the fluids are known to slip on the solid surface up to a few nano-meters, the molecular forces control the dynamics of the contact line motion. This region is often modeled by specifying the boundary conditions in the numerical simulations. The accurate boundary conditions for mimicking the physics of the contact line motion is unknown and is an area of active research (see references [138, 148, 149, 150]).

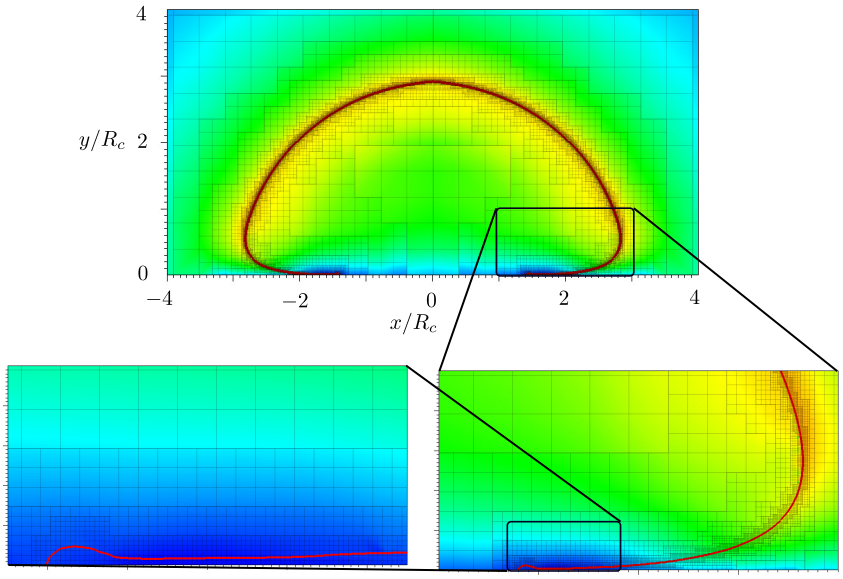


Figure 3.9: The figure shows the bubble shape in the regime where the microlayer forms during the bubble expansion, zoom in the intermediate scale is shown in the bottom right panel and zoomed in view of the smallest scale is also shown in bottom left panel.

### 3.2.1 Theoretical description of microlayer

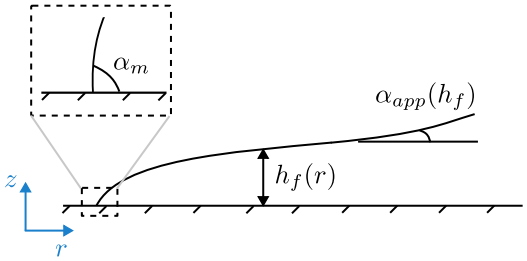


Figure 3.10: Schematic illustration of the interface close to wall approximated as the thin film often used to model the dynamics of interface at the intermediate length scale.

The theoretical models for the contact line motion and the interface shape are frequently developed using the lubrication approximations to the Navier–Stokes equations [133, 142, 151, 152]. If we assume that the interface can be represented as free surface, the velocity field is one dimensional $\mathbf{u} = \{u_r, 0, 0\}$, the gradient of velocity in direction perpendicular to the wall in $z$ direction is large as compared to the direction parallel to the wall in $r$ direction ($z$ and $r$ shown in figure 3.10), and the liquid is incompressible, in such scenario the Navier–Stokes equation reduces to (see reference [153] for detailed explanations)

$$\rho \frac{\partial u_r}{\partial t} = -\frac{\partial p}{\partial r} + \mu \frac{\partial^2 u_r}{\partial z^2}, \tag{3.11}$$

which is a linear differential equation for $u_r(z,t)$. The boundary conditions for this equation are given as following

$$u_r - \lambda \frac{\partial u_r}{\partial z} = 0, \quad at \quad r = 0 \tag{3.12}$$

$$\frac{\partial u_r}{\partial z} = 0, \quad at \quad y = h_f \tag{3.13}$$

$$p = -\sigma\kappa, \quad at \quad y = h_f \tag{3.14}$$

where the interface curvature $\kappa$ can be represented in terms of interface height ($h_f$) using lubrication approximation as

$$\kappa = \frac{\partial^2 h_f}{\partial r^2} + \frac{1}{r}\frac{\partial h_f}{\partial r} \tag{3.15}$$

Simplifying (see reference [152]), one can obtain the thin film equation for the interface shape as

$$\frac{3\mu}{\sigma}\frac{\partial h_f}{\partial t} + \frac{1}{r}\frac{\partial}{\partial r}\left[(h_f^3 + 3\lambda h_f^2)r\frac{\partial}{\partial r}\left(\frac{\partial^2 h_f}{\partial r^2} + \frac{1}{r}\frac{\partial h_f}{\partial r}\right)\right] = 0 \tag{3.16}$$

The steady state solution in the limit of capillary numbers much smaller than unity for equation 3.16 is of form (see reference [131])

$$\alpha_{app}^3 = \alpha_m^3 + 9\frac{\mu u_{CL}}{\sigma} ln(r/\lambda), \tag{3.17}$$

where $\alpha_{app}$ is the apparent contact angle approximated as $\frac{\partial h_f}{\partial r}$ and $u_{CL}$ is the steady contact line velocity. This relation is commonly referred to as Cox–Voinov law. An important difference in the current study and the classical experiments of liquid coating over the solid surfaces (for which these theories are developed) is that the characteristic velocity is not an independent parameter (as velocity of solid). It depends implicitly on the driving pressure $\Delta p$ which takes a steady value asymptotically. Moreover, the characteristic velocity of bubble expansion is generally of the orders of $10m/s$ which is much larger than the classical coating experiments. Cooper & Lloyd [154] in their Appendix A, used unsteady 1-D model with uniform pressure (eq. 3.11 assuming $dp/dr = 0$) to obtain the 1-D conduction equation that can be solved by separation of variable, this solution predicts flow velocity inside microlayer to be

$$u_r = \sum_{m=1}^{\infty}\left[U_m sin(2m+1)\frac{\pi}{2}y\ exp\left(-(2m+1)^2\frac{\pi^2}{4}\frac{\nu t}{\delta^2}\right)\right], \tag{3.18}$$

where $U_m$ is an integration constant, and first term is the predominant term that decays exponentially in time ($u_r \propto exp(-\nu t)$). The zoomed in view of microlayer in the bottom left panel of figure 3.9 suggests that after the microlayer has formed, there exist a region where the interface is parallel to the wall $dp/dr \approx 0$ and the velocity is very small.

### 3.2.2 Direct numerical simulations

In this section, we discuss the DNS results for expansion of bubbles from small spherical cap nuclei. We choose the capillary number ($Ca = \mu U_c/\sigma$) and the Ohnesorge number ($Oh = \mu/\sqrt{\rho\sigma R_{c,0}}$) as characteristic non-dimensional numbers of the problem in this section. For a laboratory experiment with fixed fluids (eg. air bubble in water) if the nuclei size is fixed then one moves along the constant $Oh$ lines, while if the amplitude of pressure forcing is fixed one would move along constant capillary number lines. Along with the $Ca$ and $Oh$, we show the effect of numerical slip length ($\lambda_{num}$) and contact angle ($\alpha$) on the process of formation of microlayer. The ranges of these parameters considered in this study are as following: $Ca \in (0.005, 1.4)$, $Oh \in (0.372, 0.01)$, $\alpha \in (30°, 135°)$ and $\lambda_{num}/R_{c,0} \in (0.02, 0.003)$. We start by comprehensively describing the bubble growth and the microlayer formation process for small $Oh$ numbers by choosing a representative bubble with $Oh = 0.037$, $\alpha = 90°$, $\lambda_{num}/R_{c,0} = 0.01$ and varying $Ca$. Note that increasing $Ca$ at constant $Oh$ results in increase of both $Re = Ca/Oh^2$ and $We = (Ca/Oh)^2$. The simulations are run on the swiss super computer *Piz Daint* and a typical simulation for bubble expansion runs on 360 CPUs in around 5 hours.

#### Overall bubble dynamics

The overall growth rate of the bubble is governed by inertial effects. This is consistent with the experimental study of bubble expansion from pits, Bremond et. al. [55] could predict the growth of an hemispherical cap shaped bubble growing in contact with the wall using simple expression for asymptotic growth $\dot{R} = U_c = \sqrt{2/3\Delta p/\rho_l}$. In figure 3.11*a*, we plot the non-dimensional equivalent bubble radius defined from the volume ratio $R/R_0 = (V/V_0)^{1/3}$ against the non-dimensional time $tU_c/R_{c,0}$. After an initial transient the slope of curve does not change which is indicative of the asymptotic bubble growth regime. Since, all of the curves overlap and the slope of the curves is unity, we can conclude that in this regime the bubble growth rate (represented with equivalent radius) scales with $U_c$.

The bubble shapes for $Ca = 0.72$ (representative case) at different non-dimensional times shown with different colors in figure 3.11*b*. In the asymptotic growth regime a major part of bubble lies outside the boundary layer and the macroscopic bubble shape can be approximated as a hemispherical cap. To confirm the self-similar nature of the bubble, we rescale the bubble shapes with non-dimensional length $U_c t/R_{c,0}$ in the direction normal to the interface (see 3.11c). The shapes are self similar except for slight off set which decreases with time. This can be attributed to the fact that $\sqrt{2/3\Delta p/\rho_l}$ is the asymptotic value of growth rate which not exactly reached during the initial transient considered here.

#### Dynamics of microlayer formation

The dynamics at the intermediate length scales are controlled by visco-capillary effects. The capillary number is defined as the ratio of viscous stresses and the surface-tension stresses. The viscous stresses inhibit the motion of fluids and contact line near the wall and the surface-tension stress prevents the fluid interface from bending. Therefore, we expect more propitious conditions for the formation of microlayer at high capillary numbers. The problem of microlayer formation is similar to the the deposition of thin liquid film on the the solid surface, famously known as the

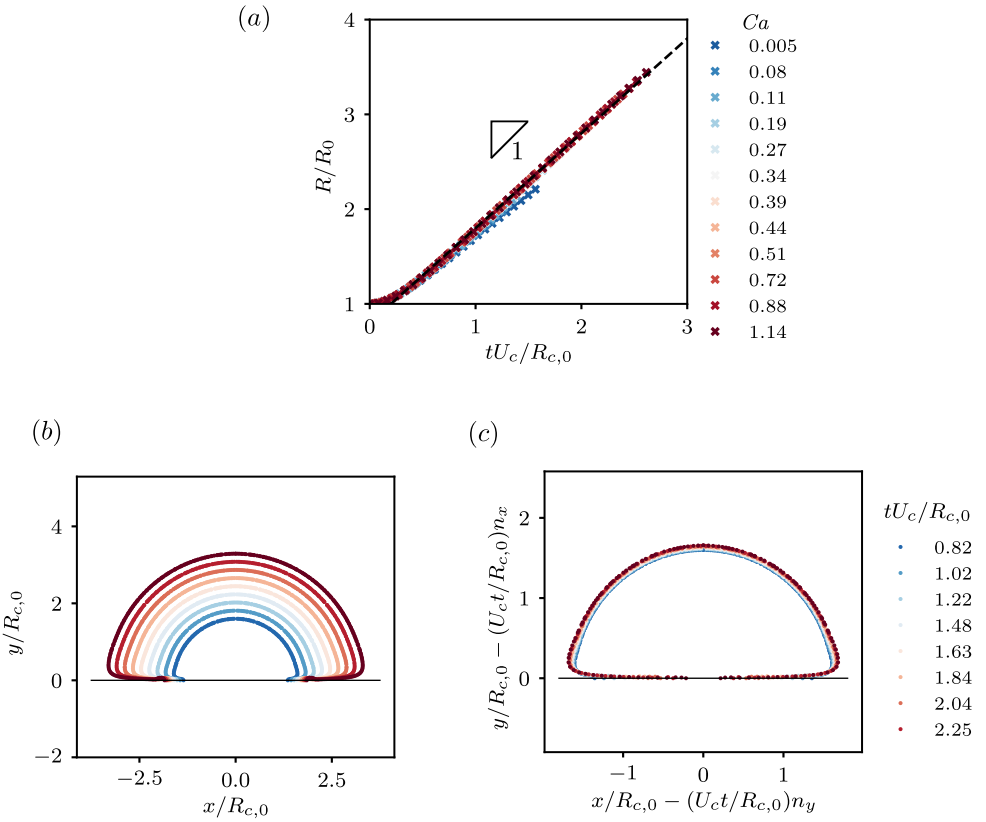


Figure 3.11: Results for bubble expansion in the case of $\alpha = 90°$,$Ob = 0.037$,$\lambda_{num}/R_{c,0} = 0.01$ and varying *Ca*. $(a)$ The evolution of non-dimensional equivalent bubble radius $R = (V/V_0)^{1/3}$ for different capillary numbers (color-map). $(b)$ The interface contours for different non-dimensional times shown with the color-map $(c)$ The interface shapes re-scaled with the characteristic velocity $U_c t/R_{c,0}$ in the normal direction

Landau–Levich–Derjaguin (LLD) film [155, 156] which has been studied extensively in past using setups where a plate is suddenly pushed in to or pulled out of the liquid and is well understood in these configurations[131, 138, 151, 157]. In context of the bubble nucleation the liquid film is known as the microlayer because the height of this film is generally of orders of a few micrometers. The problem of microlayer is also important in boiling where it enhance the evaporation rates and boiling heat transfer rates significantly [137, 158]. However, the study of microlayer formation in cavitation bubble nucleation is relatively rare ([58]).

In order to describe the effect of capillary number on the microlayer formation, we identify three characteristic points on the bubble interface as shown in figure 3.12 and defined as following: (a) The point where the bubble interface meets the $z$ axis, it is the measure of bubble height $h(t)$, the velocity of this point is defined as the time derivative bubble height $u_h = dh/dt$. (b) The point where the bubble interface meets $r$ axis, it gives the length of contact at the wall $c(t)$ and characterize the motion of contact line. The velocity of this point is defined as $u_{CL} = dc/dt$. (c)

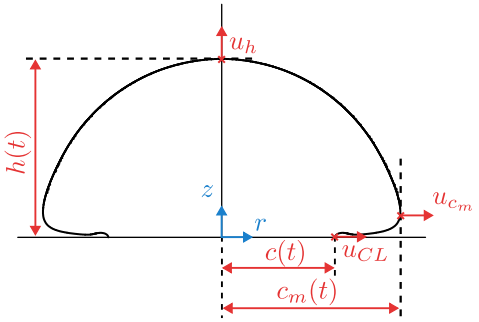


Figure 3.12: The definition of relevant points on the bubble interface that are used for describing the bubble expansion and formation of microlayer

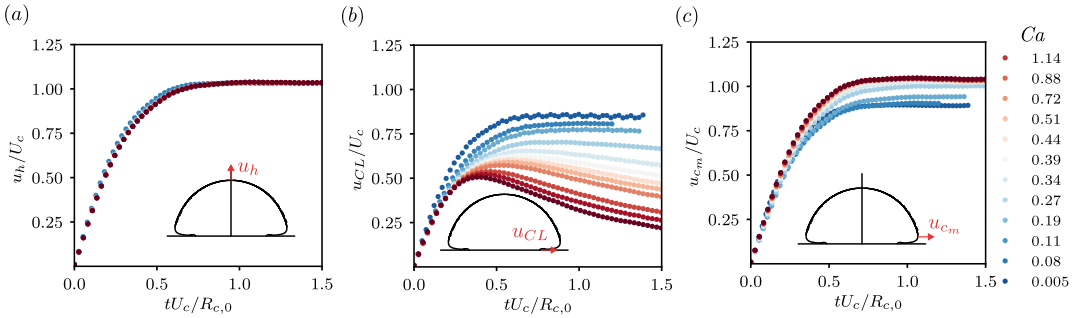


Figure 3.13: Results for bubble expansion in the case of $\alpha = 90°$,$Oh = 0.037$,$\lambda_{num}/R_{c,0} = 0.01$ and varying *Ca*. This figure characterize the motion of the interface using three points defined in figure 3.12. $(a)$ The velocity of axial point defined as $\frac{1}{U_c}\frac{dh}{dt}$ $(b)$ The velocity of contact point defined as $\frac{1}{U_c}\frac{dc}{dt}$ $(c)$ The velocity of the point corresponding to $c_{max}$ defined as $\frac{1}{U_c}\frac{dc_{max}}{dt}$

The third point is defined as the interface point at the maximum radial distance $(c_m(t))$ from the $z$ axis. The velocity of this point is defined as $u_{c_m} = dc_m/dt$.

The evolution of velocity of these three points non-dimensionalized with the characteristic velocity of bubble growth are plotted in figure 3.13*a*,*b* and *c*, for different capillary numbers (colormap). The point $h(t)$ lies outside the boundary layer for all values of *Ca* and is therefore independent of the capillary number. The height evolves with velocity $U_c$ after an initial transient that is of the order of convective time $(tU_c/R_{c,0} \sim 1)$. The contact line velocity shown in figure 3.13*b* evolves similar to the $h(t)$ for small flow capillary numbers, i.e. the contact line velocity approaches the characteristic velocity $U_c$ after an initial transient. As expected in this case, the interface is unable to bend and the microlayer formation is inhibited (see figure 3.14 $(a)$ - $(d)$). In such a case the Rayleigh–Plesset model can be used to describe the overall bubble dynamics. However as the capillary number increases, the viscous stresses becomes important and impede the motion of contact line resulting in the temporally decaying $u_{CL}$ after the initial transient. The contact line velocity decays faster for large values of the capillary numbers. Note that the equation 3.18, also predict the similar trend for the velocity at some distance from the no-slip wall due to viscous effects $u \propto e^{-\nu t}$. Also, at large *Ca* the surface tension stresses are reduced which promote the bending of the interface and the formation of microlayer as seen from figure 3.14$(e) - (h)$.

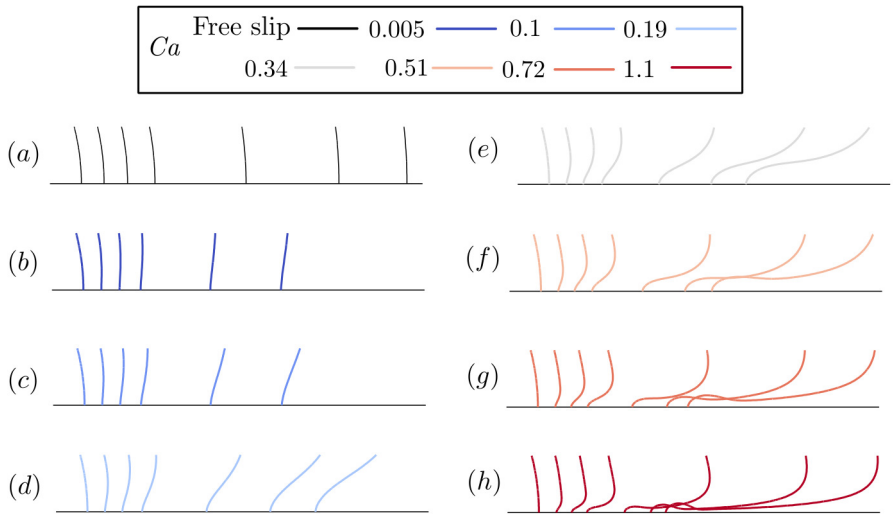


Figure 3.14: Results for bubble expansion in the case of $\alpha = 90°$,$Oh = 0.037$,$\lambda_{num}/R_{c,0} = 0.01$ and varying *Ca*. The zoomed-in view of the evolution of bubble interface close to the wall, each panel corresponds to different capillary numbers *Ca* represented with the colormap. In each of the panel, the interface evolves from left to right and each lines corresponds to different non-dimensional time. The non-dimensional time $tU_c/R_{c,0}$ interval between the curves in each panel is $0.408$ therefore contours in each panel are shown at $tU_c/R_{c,0} \in \{0, 0.41, 0.82, 1.22, 1.63, 2.04, 2.44\}$

During the time scales associated with the microlayer formation, the steady contact line velocity is not reached and the standard models for predicting the dewetting transition based on steady contact line velocity (eg. reference [157]) are expected to be inaccurate. An interesting future perspective could be to compare the current DNS calculations with the steady contact line theory in order to estimate the effect of time dependence of $u_{CL}$ on the transition into microlayer formation regimes.

Finally, the velocity for the point $c_m$ exhibits a behavior similar to contact line ($c(t)$) for small capillary numbers, while the response resembles that of the axial point ($h(t)$) for large capillary numbers (see figure 3.13*c*). This fact is more clear in figure 3.15 *a*, where we show the velocity of these three points $h, c, c_m$ in the same plane at an instant $tU_c/R_{c,0} = 1.22$ (sufficiently larger then the initial transient time). The rate of microlayer formation can be quantified as the difference between the velocity $u_{c_m}$ and the contact line velocity. For $Ca > 0.24$, $u_{c_m}$ is equal to $U_c$ and therefore the rate of microlayer formation depends on the unknown contact line velocity ($u_{CL}$). This velocity is shown to decrease monotonically with the *Ca* and consequently the rate of microlayer formation i.e. difference between red circles and blue crosses increases with *Ca*.

Inside microlayer the flow is mainly governed by visco-capillary effects, where $\sigma/\mu$ is expected to be more important velocity scale in this region. In figure 3.15*b*, we plot the evolution of the local contact line capillary number, $Ca(u_{CL}) = \mu u_{CL}/\sigma$. As expected for small global capillary numbers ($Ca < 0.24$ in this case), the contact line capillary number is approximately equal to the global capillary number $Ca(u_{CL} \approx ca)$ after the initial transient. Interestingly, at $tU_c/R_{c,0} \sim$

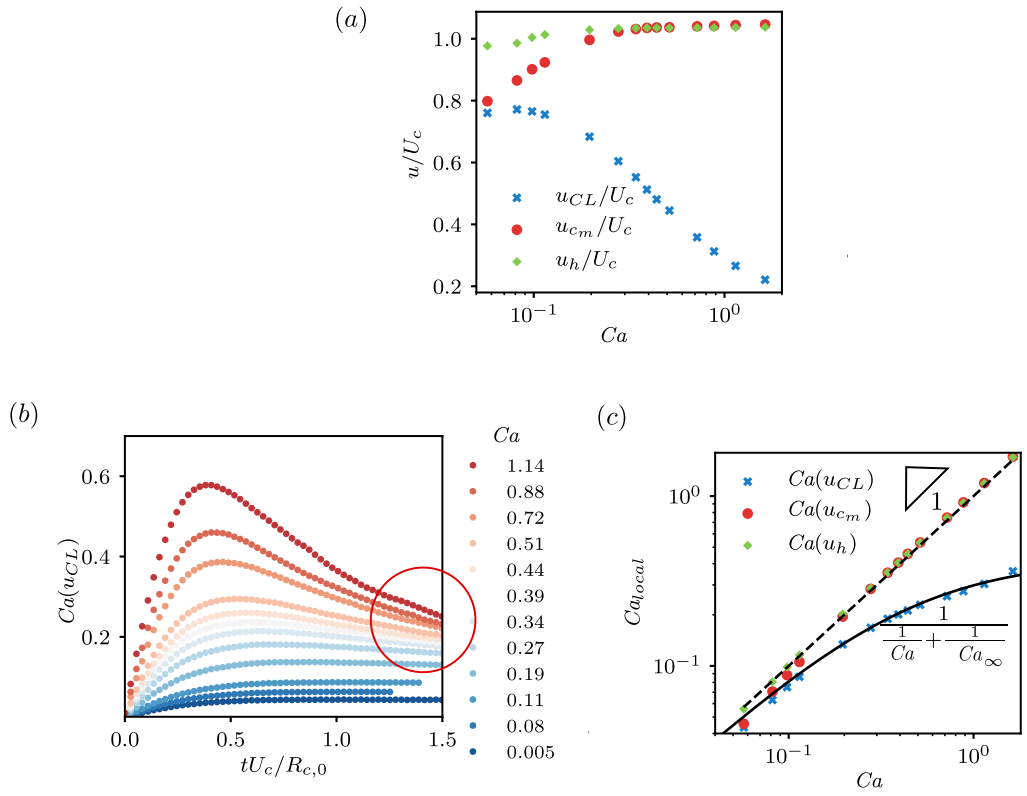


Figure 3.15: Results for bubble expansion in the case of $\alpha = 90°$,$Oh = 0.037$,$\lambda_{num}/R_{c,0} = 0.01$ and varying $Ca$. $(a)$ The non-dimensional velocity of three interface points defined in figure 3.12 at non-dimensional time $tU_c/R_c = 1.22$ is shown for different values of capillary numbers. $(b)$ The evolution contact line capillary number $Ca(u_{CL}) = \frac{\mu u_{CL}}{\sigma}$ for different values of capillary numbers (color-map). $(c)$ Local capillary numbers for three interface points defined in figure 3.12 at non-dimensional time $tU_c/R_c = 1.22$ is shown for different values of global capillary numbers. The dotted line is $Ca = Ca_{local}$ and the solid is fitting using harmonic averaging i.e. $\frac{1}{\frac{1}{Ca}+\frac{1}{Ca_\infty}}$

1.5 (region highlighted with red circle in figure 3.15*b*) the contact line capillary number converges asymptotically both in terms of non-dimensional time and in global capillary numbers for $Ca > 0.24$. A similar asymptotic behavior was observed in the numerical simulations of Guion [159], who proposed that $Ca(u_{CL})$ can be represented with a harmonic average formula as

$$Ca(u_{CL}) = \frac{1}{\frac{1}{Ca} + \frac{1}{Ca_\infty}}, \tag{3.19}$$

for all values of $Ca$. In figure 3.15*c*, we show the contact line capillary number (blue cross) at $tU_c/R_{c,0} = 1.22$ as well as equation 3.19 with a thick black line. Equation 3.19 captures well the regimes of both small and large global capillary numbers as well as the transition between the two. It also allows us to find the asymptotic value $Ca_\infty$ for $Ca(u_{CL})$ in the limit $Ca \to \infty$. The local $Ca$ for other points in figure 3.12 (for $h$ we define as $Ca(u_h) = \mu u_h/\sigma$ and for $c_m$ we define

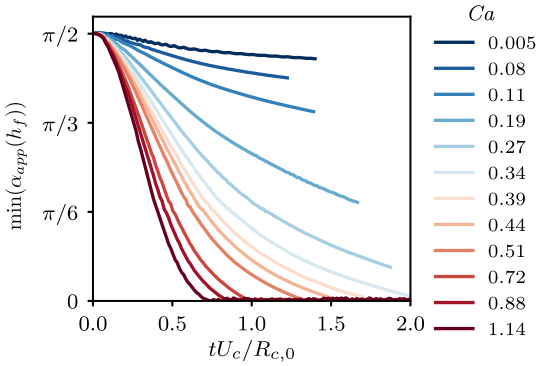


Figure 3.16: Results for bubble expansion in the case of $\alpha = 90°$,$Oh = 0.037$,$\lambda_{num}/R_{c,0} = 0.01$ and varying *Ca*. The minimum value of apparent angle defined as the angle between the tangent to the interface and the radial axis $r$ at a given microlayer thickness $(h_f)$.

$Ca(u_{c_m}) = \mu u_{c_m}/\sigma$) are also shown to be equal to *Ca* (see figure 3.15*c* red and green points) as one would expect for $U_c = 1$.

The bending of the interface can be quantified by computing the apparent contact angle defined in figure 3.10(angle between the tangent to the interface and the axis parallel to wall in the liquid phase). For the spherical cap (at $tU_c/R_{c,0} = 0$) this angle would vary from $\alpha$ to $\pi$, as the interface bends and deviates from spherical cap shape, this angle can decrease below $\alpha$. In figure 3.16, we plot the evolution of the minimum value of $\alpha_{app}$ (indicator of maximum bending) over the interface. For small values of *Ca*, the minimum value of $\alpha_{app}$ decreases slightly below the $\alpha$. As *Ca* increases the interface bends more and this angle decreases at faster rates, for $Ca > 0.42$ it decreases to zero value indicating that the interface becomes parallel to the wall in the region where the microlayer is formed.

### Effect of equilibrium contact angle

The Cox–Voinov solution (equation 3.17) obtained by solving steady state thin film equation in the limit $Ca \ll 1$ shows that the apparent contact angle depends strongly on the microscopic contact angle (see section 3.2.1). The angle $\alpha$ is the numerical equivalent of microscopic contact angle $\alpha_m$ therefore, we study the microlayer formation as a function of $\alpha \in (30°, 135°)$ and $Ca \in (0.07, 0.55)$ for constant $Oh = 0.037$ and $\lambda_{num}/R_{c,0} = 0.01$. In figure 3.17*a*, we plot the contact line capillary number $Ca(u_{CL})$ with circles as function of global capillary number *Ca* for several contact angle boundary conditions $\alpha$ (color-map), and fitting with the harmonic average formula (dotted lines). The black line corresponds to $Ca(u_{CL}) = ca$ which is the upper limit for the value of $Ca(U_{CL})$. The DNS reveals that small $\alpha$ favors the formation of microlayer, in particular for $\alpha < 60°$, the velocity of contact line remains small for all range of capillary numbers tested and the microlayer forms almost instantaneously. The numerically obtained asymptotic values of contact line capillary number $Ca_\infty$ (red crosses in figure 3.17*b*) is well represented as a cubic function $0.12 \times \alpha^3$ ($\alpha$ in rad). A similar trend was observed by Guion et. al. [159] for $\alpha < \pi/2$, surprisingly the cubic dependence holds for large angles. Note that, if we suppose that Cox–Voinov law (originally obtained in small *Ca* regime) is valid and try to predict $Ca(u_{CL})$ such

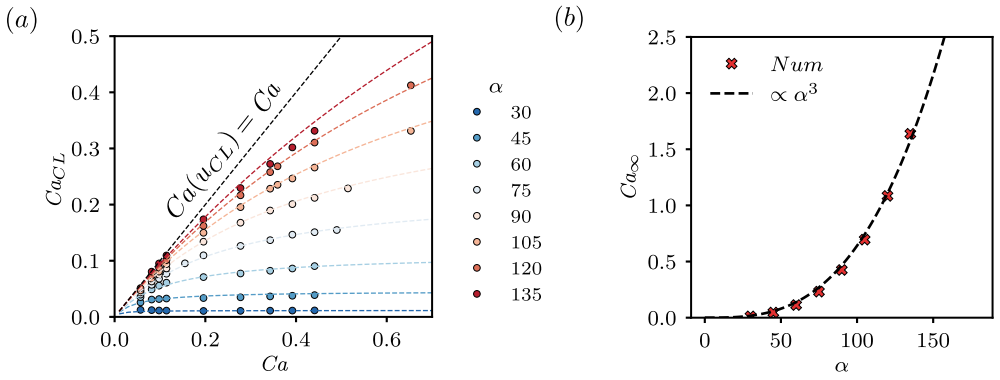


Figure 3.17: Results for bubble expansion in the case of $Oh = 0.037$,$\lambda_{num}/R_{c,0} = 0.01$ and varying $Ca$ as well as $\alpha$. The effect of contact angle on the asymptotic growth regime of microlayer $(a)$ The numerical results (circles) for contact line capillary number $Ca(u_{CL})$ as a function of global capillary number $Ca$, the dashed lines show the fitting curves obtained using $Ca = \frac{1}{\frac{1}{Ca} + \frac{1}{Ca_\infty}}$ for different contact angle boundary conditions (color-map). $(b)$ The fitting parameter $Ca_\infty$ that represents the global capillary number for asymptotic microlayer growth is plotted as a function of $\alpha$, along with the fitted curve $\propto \alpha^3$ (dashed line).

that at interface height $L$, $\alpha_{app} = 0$ as seen from figure 3.16, we can obtain a relation between the $Ca(u_{CL})$ and $\alpha$ as

$$Ca(u_{CL}) = \frac{1}{9log(L/\lambda)}\alpha^3, \tag{3.20}$$

which recovers the cubic dependence of $Ca(u_{CL})$ on the contact angle. Further matching the numerical and theoretical prefactors i.e. $\frac{1}{9log(L/\lambda)} = 0.12$ results in $L/\lambda = 2.5$, which is not physically meaningful (as the $\lambda$ is generally nanometer length scale and $L$ is few micrometers). This discrepancy might be caused by two main reasons a) the capillary numbers are not small enough to neglect the higher order terms in $Ca$, b) The numerical slip length that we put in the simulations $\lambda_{num} = 0.012R_{c,0}$ (which is smallest permissible with current computational resources) might not be small enough to capture the separation of length scales between the slip length and the microlayer region. An important take away from above results for constant $Oh = 0.037$ is that the slip model predicts an asymptotic value of contact line capillary number $Ca(u_{CL})$ for all values of $\alpha$ considered which varies with the cube of $\alpha$. As the asymptotic regime is achieved when $Ca \to \infty$ at fixed $Oh$, it can also be understood as regime where $Re \to \infty$ and $We \to \infty$.

### Finite Reynolds and Weber number effects

The dynamics of microlayer formation can be discussed in terms of the capillary number only in the limit of large Reynolds and Weber numbers. In real applications, the bubble nuclei can be smaller than 10 micron and this condition might not be fulfilled. Because both, $Re$ and $We$ are going to be increasingly small as the size of the nuclei decreases. In this section, we will use as characteristic quantity of the problem as Ohnersorge number, which is of the order of 1 for

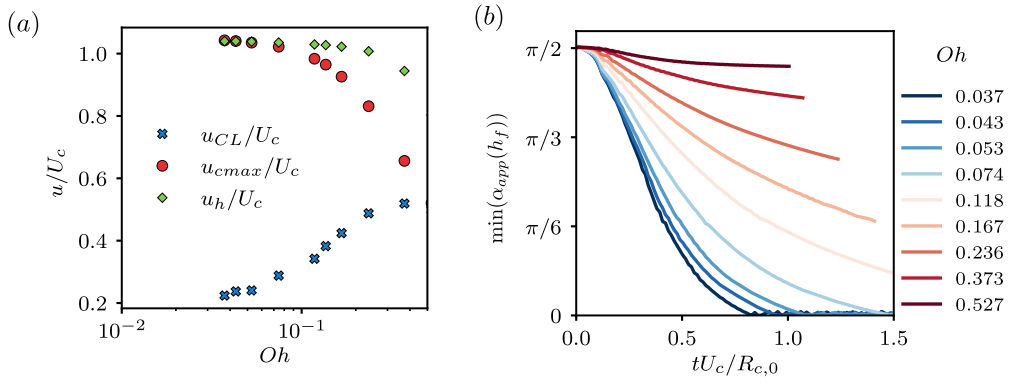


Figure 3.18: Results for bubble expansion in the case of $\alpha = 90°$,$Ca = 0.57$,$\lambda_{num}\rho\sigma/\mu^2 = 0.00012$ and varying $Oh$. The effect of Ohnesorge number on the microlayer formation at constant $Ca$. $(a)$ The velocity of three important interfacial points is plotted as a function of Ohnesorge number. $(b)$ The evolution of minimum interface slope is shown for different Ohnesorge numbers (colormap)

nanometric nuclei. For constant capillary number, the Reynolds and Weber number can be expressed as a function of Oh as $Re = ca/Oh$ and $We = ca/Oh^2$. We vary $Oh$ at fixed the capillary number $Ca = 0.7$ (chosen arbitrarily), slip length $\lambda_{num}\rho\sigma/\mu^2 = 0.00012$ and contact angle $\alpha = \pi/2$. In figure 3.18$a$, we show the the velocity of the interfacial points, $h$, $c$, $c_m$ (figure 3.12) at non-dimensional time $tU_c/R_{c,0} = 1.45$ (sufficiently larger then the initial transient time). The previously described asymptotic behavior for microlayer growth is recovered at the small $Oh$. As the $Oh$ increases, the finite $Re$ and $We$ effects start to appear. The velocity of $c_m$ decreases and that of contact line increases, when both become comparable, the microlayer growth is suppressed. Therefore the asymptotic theory is valid for $Oh \ll 1$ at a fixed $Ca$. It would also be an interesting future perspective to understand the finite viscosity and capillary effects. In the figure 3.18, we show the evolution of the minimum of interface slope for varying $Oh$ shown in the colormap, the interface slopes decays faster for small $Oh$ and increasing $Oh$ results in less bending of the interface.

The microlayer formation is suppressed when the $Oh$ increase at constant $Ca$ or when $Ca$ decreases at constant $Oh$. In both these cases we move closer to the critical pressure drop required for the unstable bubble growth. The critical pressure equation (equation 3.4) can be transformed into the $Oh - Ca$ plane, therefore we can obtain a critical Capillary number $Ca_c$ corresponding to Ohnesorge numbers for which we expect the bubble to become unstable

$$Ca_c = Oh\sqrt{2\left(1-\frac{1}{3\gamma}\right)\left[\frac{3}{2}\left(\frac{Ca_0}{Oh}\right)^2\gamma\left(1+2\left(\frac{Oh}{Ca_0}\right)^2\right)\right]^{1/(1-3\gamma)}}, \qquad (3.21)$$

where $Ca_0$ is defined as $Ca_0 \equiv \frac{\mu}{\sigma}\sqrt{p_{L,0}/\rho_l}$. In figure 3.19 we show the stable region obtained from equation 3.21 with the shaded region, the representative bubble $(a)$ in this region is also shown to be stable. Far from the critical region the bubble exhibits the microlayer formation at asymptotic rate as also seen form representative case $(c)$, when the bubble lies in the unstable re-

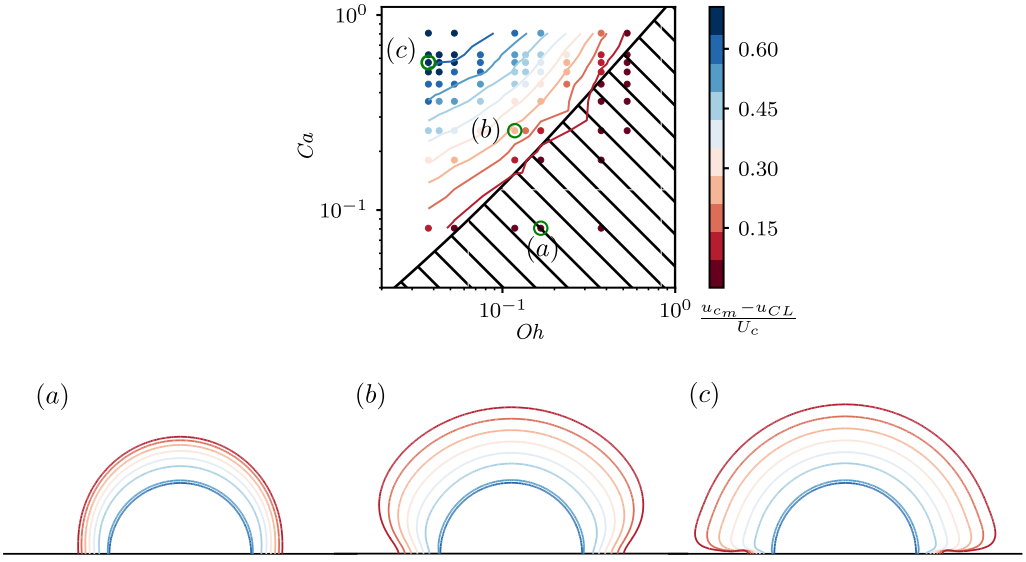


Figure 3.19: The non-dimensional velocity difference between interface point $c_m$ and the contact line is shown in the phase map of *Oh-Ca* plane. The shaded region corresponds to the stable region as predicted by equation 3.21, the solid color lines are isolines for different values $(u_{c_m} - u_{CL})/U_c$ calculated from the numerically obtained values (points). The bubble evolution is also shown for three representation cases marked as $(a)$,$(b)$ and $(c)$ with the color code representing the bubble interface at different times.

gion but closer to the stability curve the microlayer formation is inhibited even though the bubble becomes unstable.

#### Effect of slip length

The effect of numerical slip-length is summarized in this section by focusing on a representative case with $Ca = 0.54$, $\alpha = \pi/2$ and $Oh = 0.0373$. The slip length is varied from $0.001R_{c,0}$ to $0.024R_{c,0}$, and we plot the results in figure 3.20. The velocity of the three points defined in figure 3.12 is shown in figure 3.20$a$, as expected the effect of slip-length is local to the contact line and does not influence the motion of $c_m$ and $h$. Also, the increase in slip length facilitates the mobility of the contact point, thus the contact line velocity increases causing decrease in microlayer growth rate. This conclusion is supported by the evolution of minimum interface slope represented by $\alpha_{app}$ in figure 3.20$b$. Therefore the the asymptotic values of the contact line capillary number is a function of the slip length imposed in the numerical simulations.

### 3.2.3 Structure of Microlayer

Here, we consider the bubble shape in the microlayer formation regime and match the same with the known solutions from the literature. The bubble interface obtained from DNS for a representative case of $Ca = 1.14$, $Oh = 0.0327$, $\alpha = \pi/2$, $\lambda_{num} = 0.012R_{c,0}$ is plotted at non-dimensional time $tU_c/R_{c,0} = 2.65$ with black cross on the linear and log-log axis in figure 3.21$a$ and $b$ respectively. The axis are non-dimensionalized with the capillary length $L_\sigma = \sigma/\Delta p$. The

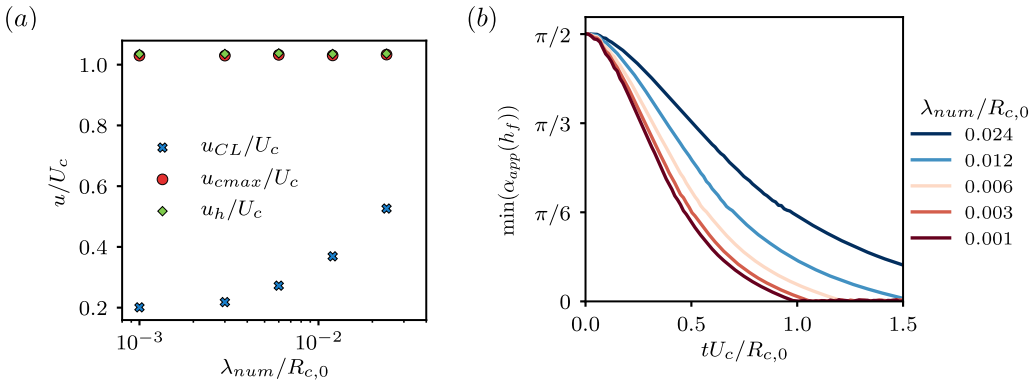


Figure 3.20: Results for for bubble expansion in the case of $\alpha = 90°$,$Oh = 0.037$, $Ca = 1.4$ and varying $\lambda_{num}/R_{c,0}$. The effect of slip length on the microlayer formation regime. $(a)$ the velocity of three important interfacial points is plotted as a function of non-dimensional slip-length. $(b)$ The evolution of the minimum interface slope for various slip-length (color-map)

three distinguishable features or the interface can be described as following: The bubble shape outside microlayer which remains hemispherical and is well represented with a curve with constant radius of curvature centered at the initial center of curvature of nuclei as shown with the blue curve. The interface close to wall is highly curved and a bulge is formed similar to one observed in previous numerical results of reference [137, 158]. In the microlayer region, the classical Cox–Voinov law fails to even qualitatively predict the interface shape in the intermediate region as it predicts a convex interface shape, whereas the interface forms a concave shape following the cusp/bulge region. Guion et. al. [137] also obtained an concave shape and obtained an alternative solution for the interface shape in the microlayer region by scaling the inertial and viscous forces. This yielded the microlayer height $h_f = C_0\sqrt{r}$ where $C_0$ is some constant and $r$ is the

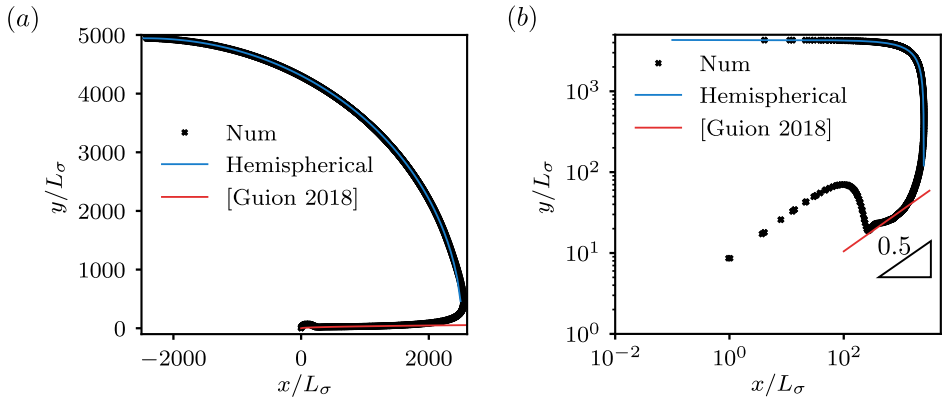


Figure 3.21: Results for for bubble expansion in the case of $\alpha = 90°$,$Oh = 0.0327$,$\lambda_{num}/R_{c,0} = 0.01$ and $Ca = 1.4$. The interface shape obtained from the direct numerical simulations (black cross) and the models proposed for interface shape are also shown with thick lines in $(a)$ linear scale $(b)$ log-log scale.

non-dimensional radial distance from the contact line. Surprisingly, this scaling describes the interface shape reasonably well in the microlayer region (red curve in figure 3.21), this fact really questions the basic assumption in the theoretical models for prediction of interface shape i.e. in the intermediate scale the inertial effects are negligible.

# 4 Bubble collapse

The process of bubble nucleation, discussed in the previous chapter, is followed by the collapse of the cavity formed. In this chapter, we investigate the dynamics of the collapse of a single bubble that is in contact with a rigid wall. Particularly, we show that the bubble shape at the instant of maximum radius is a critical parameter that governs the direction of jets created during the bubble collapse. We show that for a spherical cap bubble, when the contact angle is larger than 90 degrees a classical jet directed towards the wall is observed whereas when the contact angle is larger than 90 degrees an annular re-entrant jet appears. We explain this change of behavior using the impulse potential flow theory for small times which shows the presence of a singularity on the initial acceleration of the contact line when the contact angle is larger than 90 degrees. Direct numerical simulations show that although viscosity regularizes the solution at $t > 0$, the solution remains singular at $t = 0$ even for finite Reynolds numbers. In these circumstances, numerical and experimental results show that the collapse of flat bubbles can eventually lead to the formation of a vortex ring that induces unexpected long-range effects. Using the numerical simulations and the energy conservation principle, we also characterize the strength of collapse by considering different energy exchange that takes place during the collapse of the bubble. When the bubble collapse is not spherically symmetric the kinetic energy accumulated inside the liquid can significantly penalize the maximum gas pressures reached during the collapse. The effect of kinetic energy becomes increasingly important as the pressure difference driving the collapse increases.

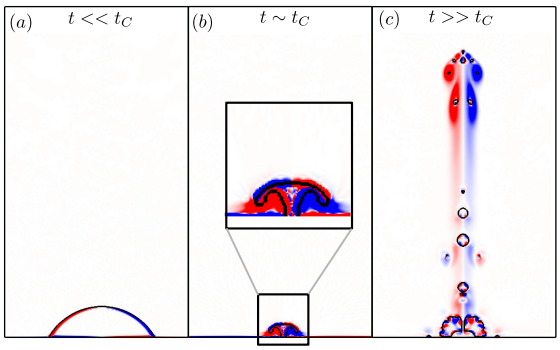


Figure 4.1: The collapse dynamics of a spherical cap bubble in contact with rigid wall explained in terms of 3 time scale $(a)$ the short time scale which is much smaller than the bubble collapse time scales $(b)$ The time scales comparable with the bubble collapse time scale $(c)$ The time scales much larger than the collapse time scales

In figure 4.1, we start by showing the phenomenology of collapse of a flat bubble in contact with a rigid wall obtained from direct numerical simulations. We draw the bubble interface contour

with black curves and the vorticity field with colormaps. The bubble dynamics can be described in three stages corresponding to three time scales shown in panels a,b & c respectively. At short time after the beginning of collapse phase $t \ll t_c$ the bubble interface experiences a non-uniform acceleration due to asymmetry caused by the wall. This leads to the appearance of liquid jets at the time scales comparable with the collapse time scales ($t \sim t_c$). These jets are responsible for cavitation damage and accumulate the kinetic energy which can further penalize the maximum gas pressure reached during the bubble collapse. In certain situations, this jet can generate a secondary jet opposite to the wall that can result in a vortex ring formation at $t \gg t_c$. Figure 4.1 also lay an outline for the contents of this chapter. To understand the dynamics at short time scales ($t \ll t_c$), we use impulse potential theory characterize the acceleration of fluid interface that turns out to be singular at the contact line. To describe the dynamics at longer time scales ($t \sim t_c$), we use DNS and energy balance equation to understand the energy transfers in to various forms during the collapse. We also study the change in jetting direction as a function of bubble shape from the DNS results and compare these to the experiments of laser induced bubbles. At much longer time scales $t \gg t_c$, we illustrate the formation of vortex ring using DNS and clarify that it is a surprising consequence of bubble shape and singularity at $t \ll t_c$.

## 4.1 Problem setup

We focus on the classical three dimensional Rayleigh problem for the bubble attached to wall that has a shape of spherical cap. We restrict this study to an axi-symmetric configuration which allow us to focus the computational resources to resolve complex flow fields near the wall. The problem and the relevant non-dimensional numbers are described in detail, in chapter 2, where $p_\infty > p_{L,0}$ results in the collapse of bubble. The characteristic velocity of the bubble collapse is chosen to be $U_c = \sqrt{p_\infty - p_{L,0}}/\rho_l$. For a low pressure bubble (assuming $p_{L,0} \ll p_\infty$) collapsing in water under the action of the ambient pressure, the characteristic velocity is $U_c = 10\mathrm{m}/s$, and therefore both the Reynolds and Weber number are determined only by the radius of curvature of the bubble. In particular, for the experiments considered in this study, the radius of curvature remains to be of the order 1 cm obtaining characteristic values of the Weber and Reynolds number of the order of $We \sim O(10^4)$ and $Re \sim O(10^5)$. The influence of finite values of Reynolds number will be discussed at the end of the chapter.

## 4.2 Short time dynamics

The dynamics of a collapsing bubble at short time scales after reaching the instant of maximum volume corresponds to first stage in figure 4.1. From the analytical perspective, the system of equations can be simplified if we consider the interface as a free surface, i.e. we neglect inertial and viscous effects inside the bubble, which is a reasonable assumption given that $\mu_g/\mu_l \ll 1$ and $\rho_g/\rho_l \ll 1$. The velocity at small times remains negligible therefore the convective terms can be neglected as compared with temporal derivatives of velocity and spatial pressure gradients [160, 161]. This hypothesis remains true when the time scales under consideration are smaller than the advection time scales i.e. $\frac{t_s U_c}{R_c} \ll 1$. Under these assumptions, we can obtain velocity field by integrating the linearized momentum equation as

$$\mathbf{u}(t_s) = -\frac{1}{\rho}\int_0^{t_s} \boldsymbol{\nabla} p + \frac{1}{\rho}\int_0^{t_s} \boldsymbol{\nabla}\cdot\boldsymbol{\tau}. \tag{4.1}$$

It is classical for the linear system to decompose the velocity field into a potential part ($\mathbf{u}_\phi$) and a viscous correction ($\mathbf{u}_\nu$) i.e. $\mathbf{u} = \mathbf{u}_\phi + \mathbf{u}_\nu$. The potential flow theory gives $\mathbf{u}_\phi$ whereas the viscous contribution requires more complex analysis [160, 162, 163]. For the short times and large enough Reynolds numbers, the viscous contributions to velocity are relevant only in the small region of thickness $\delta \sim \mathcal{O}(\sqrt{\nu t})$ near the solid boundary. Thus for large Reynolds and short times, we expect the solution to be governed by the potential part, the viscous part being only a correction in a thin region close to the wall.

### 4.2.1 Potential flow solution

The potential flow solution is obtained by solving the inviscid part of the linearized momentum equation

$$\frac{\partial \mathbf{u}_\phi}{\partial t} = -\frac{1}{\rho}\boldsymbol{\nabla} p. \tag{4.2}$$

Assuming that the liquid is an incompressible substance, we can take the divergence of Equation 4.2 to obtain the Laplace equation for pressure as

$$\boldsymbol{\nabla}^2 p = 0. \tag{4.3}$$

The magnitude of the initial pressure gradient field (or acceleration field) at short infinitesimal times govern the dynamics of bubble collapse at a finite time. The solution to Laplace problem is referred to as the "free surface model". The geometry of the problem setup and boundary conditions are shown in Figure 4.2 and is given as following: The bubble interface is assumed to be at a constant pressure $p_{L,0}$ and far-away from the bubble the pressure is $p_\infty > p_{L,0}$.

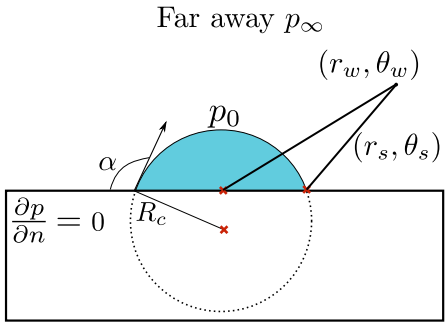


Figure 4.2: The setup for the problem where the bubble shape is spherical cap. The coordinate system used in describing the flow field i.e. $(r_w, \theta_w)$ centered at wall and $(r_s, \theta_s)$ centered at the contact point are also shown.

We introduce the dimensionless pressure $\tilde{p} = \frac{p - p_{L,0}}{p_\infty - p_{L,0}}$ to obtain the acceleration in the free surface model. Note that in the limiting case of linear problem the interface does not move, there-

fore surface tension effects at short times only introduce a correction on the scaling prefactor $(p_\infty - p_{L,0})$ upon which the solution depends. The boundary conditions required to solve the Laplace equation for $\tilde{p}$ are: $\tilde{p} = 1$ far away from the bubble, $\tilde{p} = 0$ at the bubble interface and $\frac{\partial \tilde{p}}{\partial n} = 0$ at the solid boundary. The above approximations lead to only one free non-dimensional parameter i.e. the contact angle $(\alpha)$.

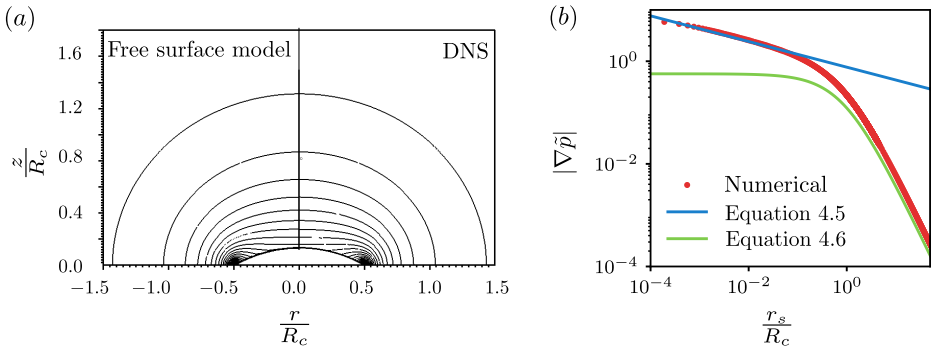


Figure 4.3: $(a)$ Isocontours of the magnitude acceleration for bubble with contact angle $\alpha = 2\pi/3$: The left half isocontours are obtained from free surface model and in the right half isocontours obtained from DNS at infinite Reynolds. $(b)$ Non-dimensional acceleration magnitude along the wall obtained for same case using the free surface model.

In figure 4.3*a*, we present the isocontours of the magnitude of the non-dimensional acceleration field ($|\nabla \tilde{p}|$) obtained for a spherical cap bubble with contact angle $\alpha = \frac{2}{3}\pi$, while figure 4.3*b* shows the profile of the acceleration along the wall in the liquid phase with respect to the distance from the contact line obtained from free surface model. The isocontours in the left half are obtained numerically from the free surface model, while on the right half are obtained from the full direct numerical simulation of the Navier–Stokes equations accounting for the presence of a gas with non-zero density and a finite value of viscosity at $\frac{tU_c}{R_c} = 2.07 \cdot 10^{-6}$. Good agreement between the two solutions support the argument that equation 4.3 is a good representation of the bubble response at very short times. We clearly distinguish two separate regions: the far-field where the pressure gradient contours are hemispherical caps centered at the axis of symmetry, and the near field where the contours for pressure gradient are intricate and diverges as the flow approaches the triple contact point. Next, we characterize each of these regions:

### Near field

The numerical solution for local non-dimensional acceleration magnitude at bubble interface $|\mathbf{a}|/a_0$ is shown in figure 4.4*a* where $a_0 = \frac{p_\infty - p_{0,L}}{\rho R_c}$ is the acceleration for a spherical bubble with radius $R_c$ and a known pressure difference. We use the angle with respect to the wall $\theta_w$ to parameterize the interface position, $\theta_w = 0$ corresponding to the point of contact between the interface and the solid wall and $\theta_w = \pi/2$ being the intersection of the interface with the axis of symmetry. We choose four representative cases with $\alpha = \pi/3, \pi/2, 2\pi/3, 3\pi/4$. As expected, in the case of $\alpha = \pi/2$, the numerical solution recovers the Rayleigh–Plesset solution and the non-dimensional acceleration is uniform and equal to one all over the interface. When $\alpha < \pi/2$ the interface acceleration (thus velocity) tends to zero at the contact line, and therefore it seizes to

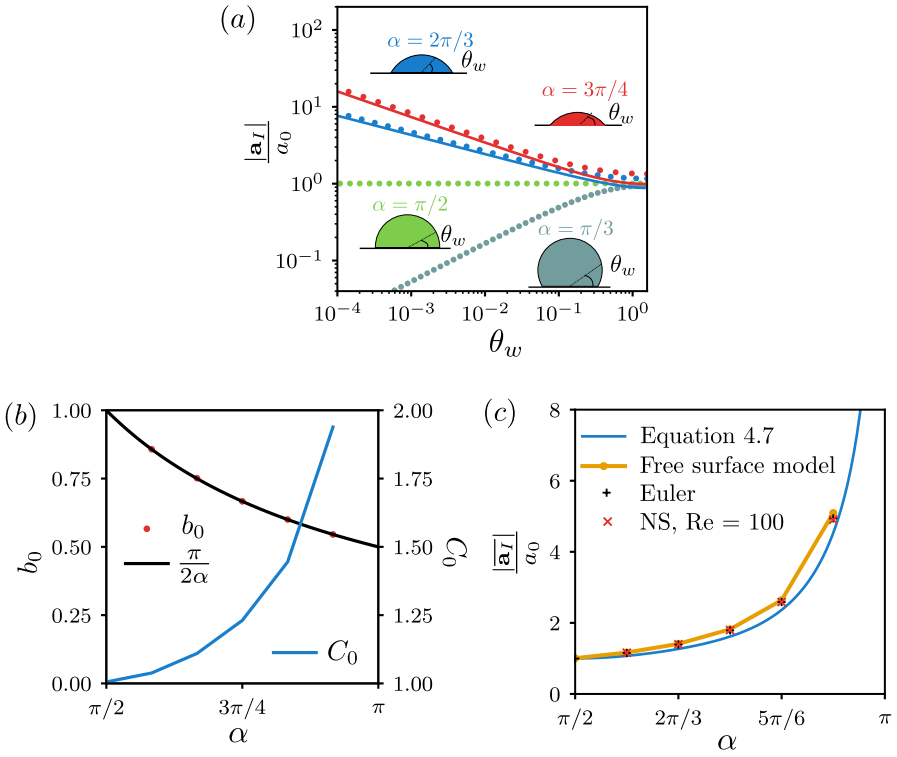


Figure 4.4: $(a)$ Non-dimensional acceleration magnitude, $|\mathbf{a}_I|/a_0$ along the interface parameterized using the angle $\theta_w$ (measured in the counter-clockwise direction from the point of contact of wall and the axis of symmetry) for $\alpha = \frac{\pi}{3}, \frac{\pi}{2}, \frac{2}{3}\pi, \frac{3}{4}\pi$. Dots represent the numerical solution from free surface model and the thick lines are predictions using equation 4.5 evaluated at the interface. $(b)$ Exponent $b_0$ and coefficient $C_0$ obtained from fitting the pressure gradient obtained from the free surface model along the wall for different $\alpha$. $(c)$ Non-dimensional averaged interface acceleration magnitude as a function of the contact angle using different methods: analytical expression given by equation 4.7 (blue line), the solution from the free surface model (yellow line), the DNS solution of the Euler equations (black crosses), and the DNS solution of the Navier–Stokes solver for $Re = 100$ (red crosses).

move even in the potential flow problem with a slip wall. For $\alpha > \pi/2$, the appearance of the singularity is evident because the acceleration diverges as we approach the $\theta_w \to 0$ limit.

To interpret this result one must keep in mind that the general solution of the Laplace equation in spherical coordinates can be obtained by separation of variables that leads to an infinite series. This series sometimes diverges at the edge where Dirichlet and Neumann boundary conditions meet due to the appearance of a singularity [164]. This singularity was reviewed extensively in the past [142, 165, 166, 167, 168, 169] but the studies where this singularity appears in the bubble dynamics problems are rare. The asymptotic solutions close to the point where homogeneous Dirichlet and Neumann boundary conditions meet can be alternatively expressed by using the general solution of the Laplace equation [164, 168, 170] and takes the form of

$$\tilde{p}_s = \sum_k^{\infty} C_k \tilde{r}_s^{b_k} \cos(b_k \theta_s), \tag{4.4}$$

where $\tilde{r}_s = r_s/R_c$ is the non-dimensional distance from the contact line and $b_k = \frac{\pi}{\alpha}(k + 1/2)$. Taking the derivative with respect to the normal of the interface, we readily find the interface acceleration magnitude near the contact line as

$$|\mathbf{a}_I| = \frac{1}{\rho}|\frac{\partial p}{\partial \mathbf{n}_I}| \approx a_0 C_0 b_0 \tilde{r}_s^{b_0 - 1}, \tag{4.5}$$

This expression exhibits a singularity at the contact point ($r_s \to 0$) when $b_0 = \frac{\pi}{2\alpha} < 1$ (or $\alpha > \pi/2$) implying that the acceleration at the triple contact point is infinite. In these conditions the first term in the expansion is the leading order term that eventually dominates the solution in the region $r_s \leq R_c$. This can also be clearly seen in figure 4.3*b* where the fitting curve shown with solid line is obtained using the first term of the series solution (i.e. parameters $C_0$ and $b_0$ in equation 4.5). We repeat the fitting procedure for various $\alpha$ to verify that the numerical values of $b_0$ match well with theoretical predictions and find $C_0$ which is a constant of order one that slightly increases with $\alpha$ (figure 4.4b). In this report, we will focus on characterization of the peculiar cases where the singularity appears using equation 4.5. Figure 4.4*a* shows that the numerical solution (dots) is well described by equation 4.5 evaluated at the interface (solid lines), showing excellent agreement close to the contact point, i.e. small values of $\theta_w$. Near the axis of symmetry (e.g. $\theta_w \to \pi/2$ and $\tilde{r}_s \approx 1$), the errors become apparent and the first term in the series does not suffice to describe accurately the acceleration field.

### Far field solution

The far field flow created by the bubble resembles to a punctual sink sitting at the intersection between the wall and the axis of symmetry. The integration of the momentum equation in the radial coordinate provides the magnitude of pressure gradient generated by a punctual sink at an arbitrary distance from the sink as

$$\left|\frac{d\tilde{p}_{\text{far}}}{d\tilde{r}_w}\right| = \frac{|\overline{\mathbf{a}}_I|}{a_0} \frac{(1 + \cos(\alpha))}{\tilde{r}_w^2}, \tag{4.6}$$

where $|\overline{\mathbf{a}}_I|$ is the magnitude of averaged acceleration along the interface, which determines the strength of the punctual sink. Figures 4.3*b* clearly shows that this equation captures well the decay of the pressure gradient with the distance $\tilde{r}_w = \tilde{r}_s + R_c \cos(\alpha)$ far from the interface.

Because the first term of the series in equation 4.5 predicts the interface acceleration reasonably well, we obtain an estimation of the averaged acceleration magnitude for bubbles with $\alpha > \pi/2$ as

$$|\overline{\mathbf{a}}_I| = \left|\frac{1}{S_b}\int \frac{-1}{\rho_l}\frac{\partial p}{\partial \mathbf{n}_I} dS_b\right| = a_0 C_0 b_0 G(\alpha), \tag{4.7}$$

where $S_b$ stands for the bubble interface surface and $G(\alpha)$ is a geometrical factor that can be numerically computed assuming that the first term in the series is indeed the leading order term along the entire bubble interface which is approximated as a straight line with contact angle $\alpha$, this gives

$$G(\alpha) = \frac{1}{1+\cos(\alpha)} \int_{\alpha-\pi/2}^{\pi/2} \left( \frac{\cos(\alpha)+\sin(\theta)}{\sin(\alpha)} \right)^{b_0-1} \cos(\theta) d\theta.$$

Figure 4.4*c* shows that the averaged non-dimensional interface acceleration magnitude obtained using this model compares well with the full numerical results of the free surface model and the DNS solution of the (both viscous and inviscid) Navier–Stokes equations. The results of the simplified model are obtained using the value of $C_0$ numerically computed and reported in figure 4.4*a*. For $\alpha > \pi/2$, $|\bar{\mathbf{a}}|$ increases with $\alpha$. The three proposed models agree well for the angles tested implying that the free surface model as well as the simplified expression given in equation 4.7 capture well the averaged bubble response at short times for sufficiently large Reynolds numbers.

### 4.2.2 Viscous correction

The potential flow solution is only formally exact at the initial time $t = 0$, when the interface is at rest. As soon as the interface is set into motion a thin boundary layer immediately develops regularizing the flow close to the contact point. To investigate the influence of viscosity on the dynamic response of the bubbles, we use the results from the DNS of the Navier–Stokes equations at short times. We use the numerical setup shown in figure 4.5*a* and the grid refined progressively near the interface to a minimum grid size of $\Delta x_{min}/R_c = 0.0007$

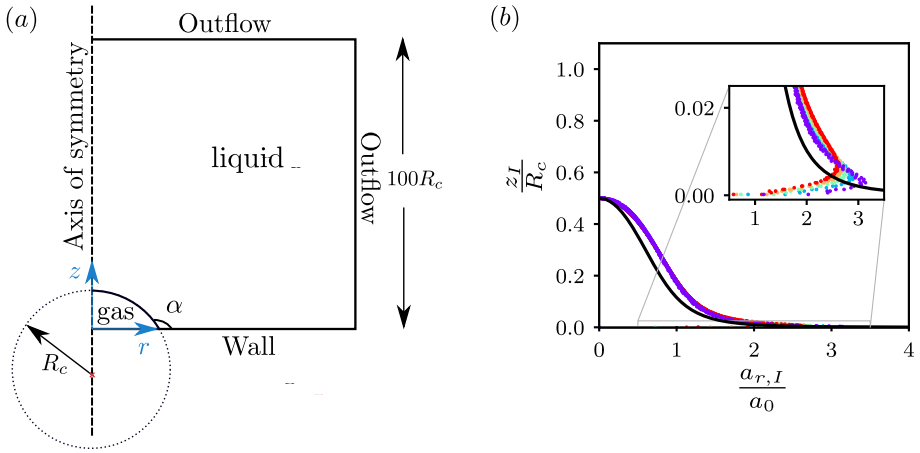


Figure 4.5: $(a)$ The numerical setup for DNS $(b)$ Results from the DNS for $\alpha = 2\pi/3$ and $Re = 100$. Time averaged interface acceleration in direction parallel to the wall, $a_{r,I} = u_{r,I}/t$, as a function of the distance from the wall at 5 different times (in color where $tU_c/R_{c,0} \in [7.27 \cdot 10^{-5}, 3.6 \cdot 10^{-4}]$). For reference we include the potential flow solution given by equation 4.5 evaluated at the interface (solid black line). The inset represents a zoom into the viscous boundary layer generated close to the wall.

In figure 4.5*b* we characterize the bubble motion at short non-dimensional time $tU_c/R_c$ by showing the evolution of the time averaged interface acceleration magnitude parallel to the wall, defined as $a_r(t) = u_r(t)/t$, as a function of the normal distance from the wall. The results shown with colored dots are obtained from DNS for $\alpha = 2\pi/3$ and $Re = 100$ where color scale represents the non-dimensional time varying between $7.27 \cdot 10^{-5}$ and $3.6 \cdot 10^{-4}$. The inset figure with zoomed view shows the clear development of a boundary layer very close to the wall where the maximum velocity defines the thickness of this layer. Outside this region the free surface potential flow solution shown with a solid black curve (Eq. 4.5) predicts the interface acceleration obtained from DNS relatively well.

In figure 4.6*a*, we show that the velocity of the contact line ($u_{cL}$) changes as the mesh is refined since slip length changes implicitly ($\lambda = \Delta x_{min}/2$) because interface moves with the cell center velocity in our numerical method (here the slip-length is not defined explicitly). Thus, inside the viscous boundary layer, the interface acceleration is sensitive to the slip length imposed and also to the movement of the contact line. In this region, the solution of free surface model at $t = 0$ cannot be extrapolated to predict the flow field near the contact line at short times.

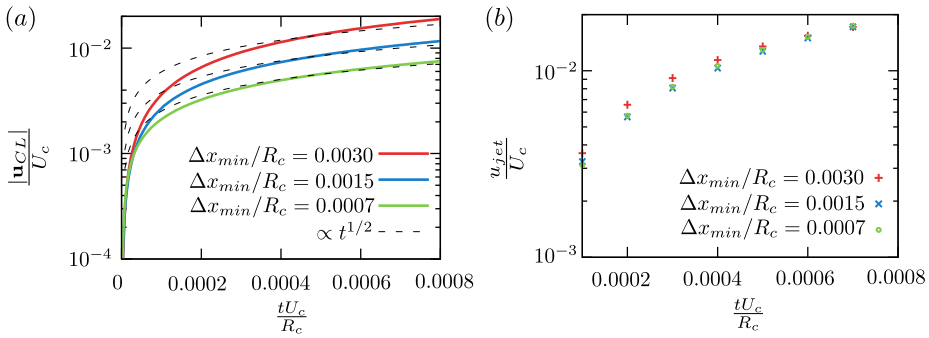


Figure 4.6: The grid convergence of viscous solution $(a)$ The evolution of velocity of contact line is plotted for different grid-size. $(b)$ The evolution of jet velocity is plotted for various grid size.

Despite the sensitivity of the contact line motion to the slip length imposed, figure 4.6*b* reveals that the peak interface velocity (jet velocity $u_{jet}$) is converged and therefore independent of the slip length. This fact together with slight dependence of the average acceleration with $Re$ (figure 4.4*c*) confirms that for large enough Reynolds numbers, the bubble dynamic response is mainly governed by the potential flow solution. In these conditions, the free surface potential flow model at $t = 0$ is a useful tool to predict the average dynamics of the interface at small times.

In order to characterize the jet formation process we extract the maximum interface velocity magnitude from DNS data, which we name as jet velocity $u_{jet}$. This velocity can be fitted using a power law function of the form (figure 4.7*a*)

$$\frac{u_{jet}}{U_c} = A\left(\frac{tU_c}{R_c}\right)^q, \tag{4.8}$$

Where $A$ is a constant. A theoretical estimation of coefficients $q$ can be obtained from the singular solution described in the previous section as follows: The jet velocity after small time

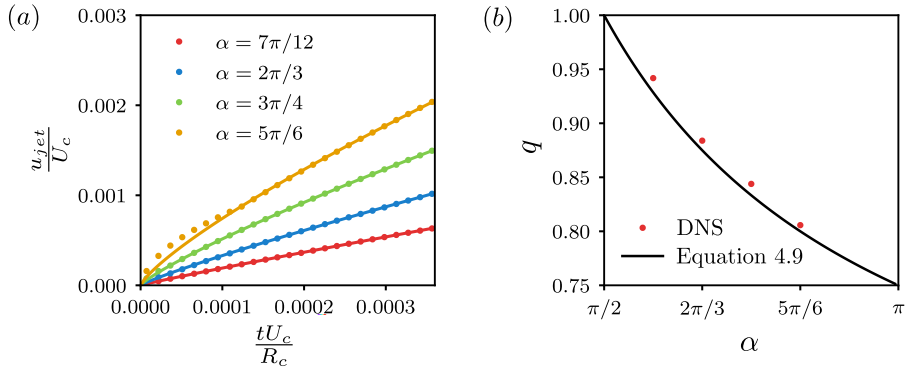


Figure 4.7: $(a)$ Evolution of jet velocity for different contact angles from (dots) DNS and (solid lines) fitting using Eq. 4.8. $(b)$ Exponent $q$ from DNS fitting and predictions of Eq. 4.9.

$(t_s)$ can be approximated from the initial acceleration evaluated at the interface at height equal to thickness of boundary layer $z = \delta(t_s)$. As $\delta$ is given approximately by the solution of the Stokes problem for the flow near the flat plate that is impulsively started from rest, it is logical to impose that $\delta(t_s) \approx C_\delta \sqrt{\nu t_s}$ where $C_\delta$ is a constant of order unity. In this case the jet velocity is estimated as

$$u_{jet}(t_s) = a_{r,I}(t = 0, z_I = \delta(t_s))\ t_s$$

where we assume that the interface quickly decelerates as soon as it enters inside the viscous boundary layer. Thus, the coefficient $q$ is readily obtained as

$$q = \frac{1}{2} + \frac{\pi}{4\alpha}. \tag{4.9}$$

As shown in Figures 4.7$b$ this model captures well the evolution of the jet velocity at small times found from DNS simulations for $\alpha > \pi/2$. The exponent $q$ (figure 4.7$c$) decreases as $\alpha$ increases because the acceleration gradient in the normal direction increases with $\alpha$ as seen in figure 4.4$b$. Note that $q < 1$ for $\alpha > \pi/2$ and therefore the jet acceleration is singular at $t = 0$ even in the presence of viscous effects.

## 4.3 Long time dynamics

After describing the dynamic response of collapsing bubble at short times in detail, we investigate the dynamics of bubbles at longer times i.e. fig 4.1$b$ and $c$. We present the discussion on the peak gas pressures and the description of phenomenology induced by non-spherical effects during the bubble collapse and the comparison of DNS results with the experiments.

### 4.3.1 Peak gas pressures and jetting during the collapse of a bubble

For an ideal gas, pressure is directly related to internal energy through equation of state, for instance during the collapse of a bubble the gas is compressed and its internal energy increases. Part of energy focused during the process of bubble collapse is released in the form of high speed liquid jets and shockwaves. These are generally responsible for the cavitation damage, and therefore understanding these energy transactions can potentially improve the understanding of cavitation damage. In this section, we present the theoretical and DNS results to understand the energy exchanges during non-spherical bubble collapse in contact with a rigid wall.

#### Theoretical background

The energy conservation equation (2.48) can be used to understand the energy exchanges during the bubble collapse. If we assume that the the surface tension effects are negligible, liquid is incompressible, and that the gas is very light in comparison with the liquid such that the $E_{k,g} \ll E_{k,l}$, where $E_{k,g}$ and $E_{k,l}$ are the kinetic energies of gas and liquid phase respectively. We can obtain equation relating the non-dimensional liquid kinetic energy with bubble volume ($V_g$) as

$$\frac{E_{k,l}}{p_\infty V_{g,0}} = \frac{1}{\gamma - 1}\frac{p_{g,0}}{p_\infty}\left(1 - \left(\frac{V_g}{V_{g,0}}\right)^{1-\gamma}\right) + \left(1 - \frac{V_g}{V_{g,0}}\right) - \Phi_D, \tag{4.10}$$

where $V_{g,0}$ is the maximum bubble volume at the end of expansion phase, $p_{g,0}$ is the initial gas pressure at instant of maximum volume $\Phi_D$ is the energy dissipated due to the irreversible effects. Assuming zero dissipation (reversible process), we can find the roots of equation 4.10 numerically to obtain the bubble volume at the instant when kinetic energy in liquid is null. These states include the instant of maximum radius ($V_g = V_{g,0}$) and the instant of minimum volume in case the bubble collapses with spherical symmetry ($\dot{R} = 0$). In the limit, $p_\infty \gg p_{g,0}$ and $V_g \ll V_{g,0}$, the right hand side of equation 4.10 reduces to unity, hence the upper bound of liquid kinetic energy in the collapse process is $Ek, l/p_\infty V_0 = 1$.

Furthermore, if we use the adiabatic law to write the volume ratio in terms of pressure ratio it is possible to obtain an equation that relates the instantaneous gas pressure and the kinetic energy in the liquid as

$$\left(\frac{p_g}{p_{g,0}}\right)^{(\gamma-1)/\gamma} + (\gamma - 1)\frac{p_\infty}{p_{g,0}}\left(\frac{p_g}{p_{g,0}}\right)^{-\gamma} = 1 + (\gamma - 1)\frac{p_\infty}{p_{g,0}} - (\gamma - 1)\left(\frac{E_{k,l}}{p_{g,0}V_0} + \Phi_D\right), \tag{4.11}$$

we could find the roots of this equation numerically for known values of $E_{k,l}$ and $\Phi_D$ to predict the gas pressure during the collapse. However, at the instant of maximum gas pressure (minimum bubble volume), the first term on the left hand side is significantly more important as compared to the second term (as $p_{max} \gg p_{g,0}$) therefore we can further simplify equation 4.11 to obtain $p_{max}$ as

$$\frac{p_{max}}{p_{g,0}} \approx \left[1 + (\gamma - 1)\frac{p_\infty}{p_{g,0}} - (\gamma - 1)\left(\frac{E_{k,R}}{p_{g,0}V_0} + \Phi_D\right)\right]^{\frac{\gamma}{\gamma-1}}, \tag{4.12}$$

where $E_{k,R}$ is the kinetic energy at the instant of minimum volume. In the limiting case of reversible spherical bubble collapse $E_{k,R} = 0, \Phi_D = 0$ and $p_\infty \gg p_{g,0}$ we recover the classical expression for the maximum pressure (see reference [171])

$$p_{max}/p_{g,0} = ((\gamma - 1)p_\infty/p_{g,0})^{\gamma/(\gamma-1)} \tag{4.13}$$

This expression reveals that the non-dimensional peak pressure reached during the spherical bubble collapse, $p_{max}/p_{g,0}$, depends on $p_\infty/p_{g,0}$ only and not on the bubble size. Note that energy dissipation and residual kinetic energy in liquid ($E_{k,R}$) are always positive, therefore the gas pressure in non-spherical collapse is always less than that of the spherical collapse. Both $E_{k,R}$ and $\Phi_D$ represent the energy that has been transferred into the liquid which otherwise could have been used for the compression of the gas. The residual liquid kinetic energy concentrated inside the high speed jets at instant of maximum compression and can be linked to the cavitation damage.

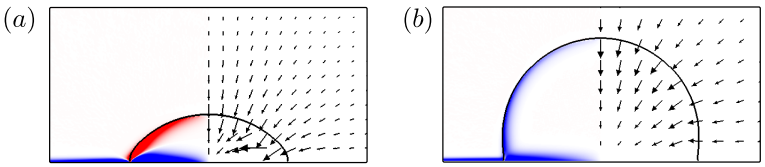


Figure 4.8: we show the vorticity in color map and velocity vectors obtained from DNS after short time short time ($\frac{tU_c}{R_c} = 0.11$) for $Re = 1000$ and $(a)$ $\alpha = 2\pi/3$ and $(b)$ $\alpha = 5\pi/12$.

It is interesting to note that for our axisymmetric system the residual kinetic energy is directly related to the presence of vorticity in the liquid (see reference [162] section 3.11) at the instant when the bubble reaches the minimum radius. At this instant the averaged velocity induced by the bubble is zero and therefore the there is no net flux across the far away boundary. In these conditions, the kinetic energy is related to vorticity as

$$E_k = \pi \int\int \omega_\theta \frac{\Psi}{r} dr dz \tag{4.14}$$

where $\Psi$ is the streamfunction. Vorticity is generated at the wall and also at the bubble interface [172, 173], and then diffused towards the liquid bulk due to viscosity. Thus there is a direct link between the emission of vorticity into the liquid and the penalization of the peak pressures reached during the collapse of a bubble. At short times vorticity is concentrated in a sheet vortex at the interface. By assuming zero stress condition at the interface for $t = 0$, the only non-zero component of the vorticity can be written as

$$\omega_\theta = -\frac{2}{R_c}\frac{\partial u_I}{\partial \mathbf{n}_I}$$

or equivalently

$$\frac{\partial \omega_\theta}{\partial t} = -\frac{2}{R_c}\frac{\partial a_I(t=0)}{\partial \mathbf{n}_I}$$

where $\mathbf{n}_I$ is the normal to the interface and $u_I$ and $a_I$ in the interface velocity and acceleration in the normal direction. It immediately follows from the potential flow solution (figure 4.4*a*) that the sign of the acceleration gradient changes depending on the initial contact angle is greater or less than $\pi/2$, reverting the sign of the vortex sheet generated at the interface. This behavior is indeed observed from the numerical simulations as shown in figure 4.8 ($a$ and $b$), where the strength of the vortex sheet is plotted with saturated color maps. The change in dominant color represents the opposite sign of vorticity at interface between the two cases. Thus, we can conclude that the presence of a free surface acts as a source of vorticity that diffuses into the liquid bulk and eventually penalize the peak pressures reached during the collapse of the bubble.

### Direct numerical simulations

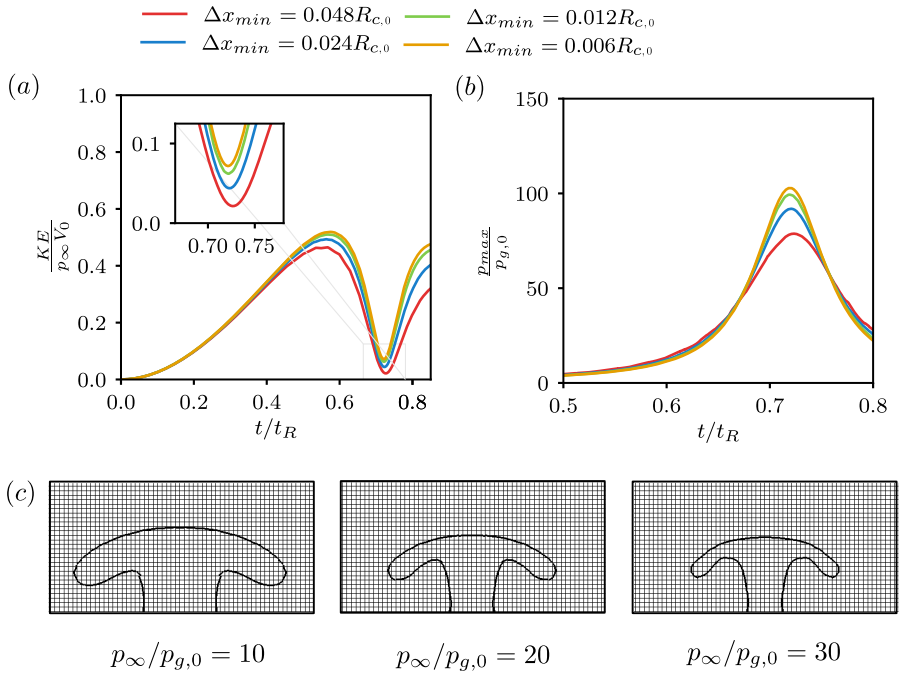


Figure 4.9: The grid convergence is demonstrated for a representative case $p_\infty/p_{g,0} = 8$, $Re = \infty$, $We = \infty$ $(a)$ Non-dimensional kinetic energy $(b)$ Average bubble pressure $(c)$ The bubble shapes for different driving pressures and smallest possible grid size as obtained from DNS using setup from figure 4.5*a*.

The relative importance of the residual kinetic energy and the viscous and acoustic dissipation mechanisms cannot be easily anticipated theoretically. Instead, we can use DNS to understand the characteristics of bubble collapse and energy exchange in the regime where $Re = \infty$, $We = \infty$ in order to limit dissipation mechanisms to liquid compressibility effects only. From the dimensional analysis of chapter 2, we see that $\alpha$ and $p_\infty/p_{g,0}$ are the free and independent non-dimensional parameters that control the bubble collapse. The numerical setup is the same as the one shown in figure 4.5*a*. The important time scale for the collapse process was given by lord Rayleigh [67] which is used to non-dimensionalize time, it is given as $t_r = 0.915 R_0 \sqrt{\rho_l/(p_\infty - p_{g,0})}$. The

grid convergence study for the evolution of kinetic energy integrated over the liquid control volume and the average bubble pressure for a representative case of $p_\infty/p_{g,0} = 8, \alpha = 2/3\pi$ is shown in figure 4.9*a*,*b*. The overall convergence for these quantities is good, the results remain slightly grid dependent in at the instant of minimum kinetic energy and maximum pressure (minimum volume). These points are hard to converge, specially at larger pressure ratios because of the non-spherical collapse and jet formation. Very thin structures start appearing during the close to minimum volume which are poorly resolved even for the finest grid. The bubble interface for different pressure ratios for the finest grid are shown in 4.9*c*, note that $p \propto 1/V^{3\gamma}$ therefore even small changes in volume are amplified as gas pressure, due to this we have restricted the discussion in current section to relatively small driving pressure.

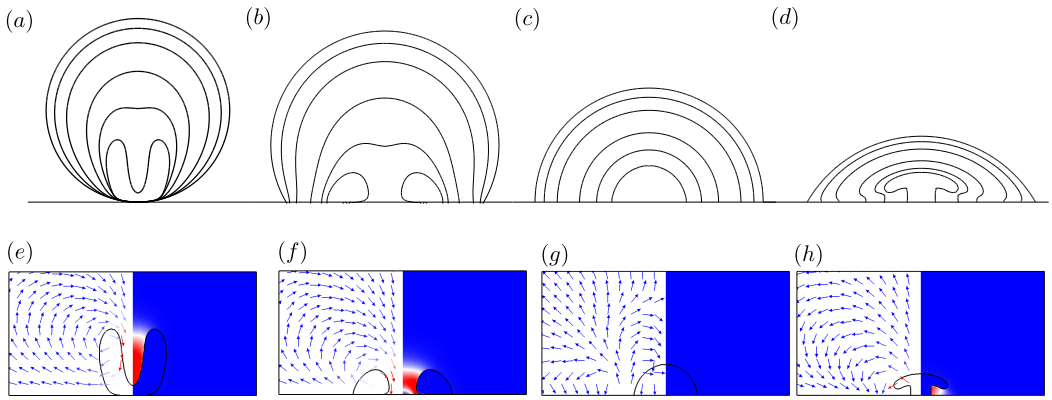


Figure 4.10: The DNS results for collapse of bubbles with different $\alpha$ and for $p_\infty/p_{g,0} = 8$,$Re = \infty$, $We = \infty$. The top row shows the evolution of bubble shapes contours for $(a)$ $\alpha = 0$ $(b)$ $\alpha = \pi/3$ $(c)$ $\alpha = \pi/2$ $(d)$ $\alpha = 2/3\pi$. The snapshot of bubble at the instant of minimum volume is given in bottom row where the interface is shown with black curve ,the kinetic energy in liquid phase is shown with linear color map in right half and the velocity vectors in left half for $(e)$ $\alpha = 0$ $(f)$ $\alpha = \pi/3$ $(g)$ $\alpha = \pi/3$ $(h)$ $\alpha = 2/3\pi$

We start by discussing the effect of initial contact angle by fixing $p_\infty/p_{g,0} = 8$. In figure 4.10 the panels $(a-d)$, we show the bubble interface evolution at various times for $\alpha \in \{0, \pi/3, \pi/2, 2\pi/3\}$ and panel $(e-h)$ shows the snapshot at the instant of minimum volume displaying the bubble interface with the black contour, the colormap of liquid kinetic energy in the right half and the velocity vectors in the left half. Two important observations from figure 4.10 are $(a)$ all the bubbles except $\alpha = \pi/2$ loose the spherical symmetry and liquid jets are present at the instant of the minimum radius which implies that the kinetic energy in not null. (b) The jet direction is different depending on the initial contact angle: the jet is directed towards the wall for $\alpha < \pi/2$ whereas an annular jet appears parallel to wall in case $\alpha > \pi/2$.

In figure 4.11*a*, we show the evolution of non-dimensional equivalent bubble radius, which shows that the minimum of equivalent radius is only weakly linked with the bubble shape whereas the non-dimensional time of bubble collapse time depends significantly on $\alpha$. The bubble collapse time (see figure 4.11*b*) for hemispherical bubble compares well with the Rayleigh collapse time, for bubbles with $\alpha < \pi/2$, it is relatively constant and around $1.25t_R$, and for $\alpha > \pi/2$ it decreases sharply. The prolongation in the bubble collapse compared to Rayleigh collapse time is discussed

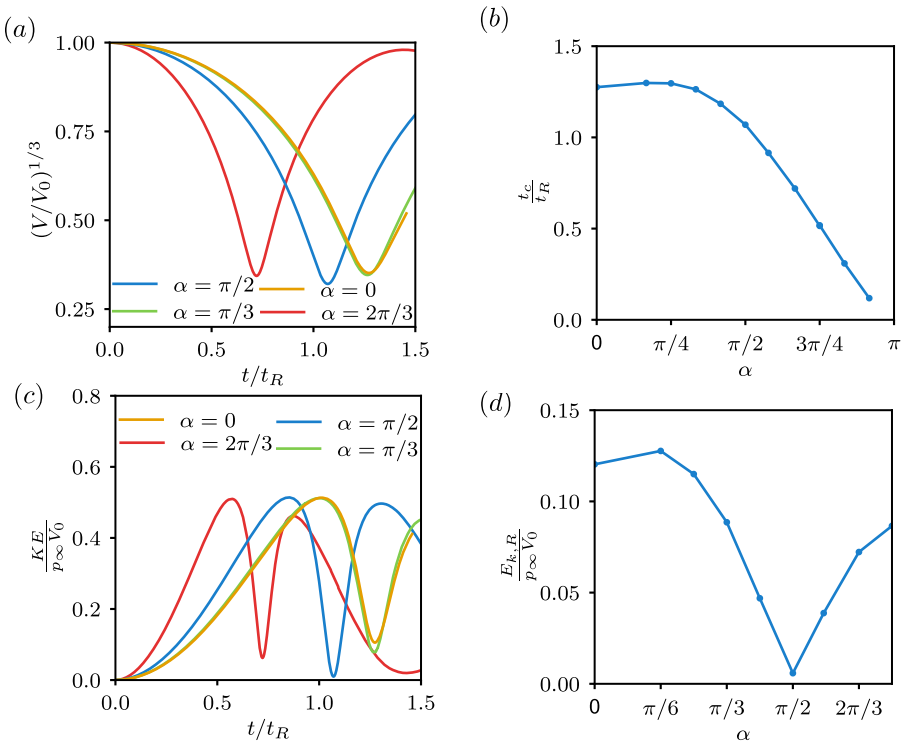


Figure 4.11: The DNS results for $p_\infty/p_{g,0} = 8$,$Re = \infty$, $We = \infty$ and varying contact angle. $(a)$ Non dimensional equivalent radius of the bubble. $(b)$ The non-dimensional collapse time is plotted as function of $\alpha$. $(c)$ The temporal evolution of the dimensionless kinetic energy integrated over liquid control volume. $(d)$ The residual kinetic energy at the instant of minimum volume for different $\alpha$.

in detail by Reuter et. al. [174] for laser generated bubbles, interestingly they also report similar factor of around 1.2 for $0.5 < d/R_{max} < 1$ (where d is standoff distance for laser focus and $R_{max}$ is the maximum bubble radius), even though the setup and shapes of bubbles are very different. In figure 4.11*c*, we show the temporal evolution of the non-dimensional kinetic energy integrated over the liquid control volume. The non-dimensional liquid kinetic energy increases as the liquid accelerates in the beginning of collapse phase and starts to decrease in the later part when the liquid decelerates close to the minimum volume. As expected, the kinetic energy does not decay to zero at the minimum volume for $\alpha \neq \pi/2$ as there is some kinetic energy accumulated inside the liquid jets, which we designated as the residual kinetic energy $E_{k,R}$. This is plotted in figure 4.11*d*, the value of $E_{k,R}$ is minimum for $\alpha = \pi/2$ (not exactly zero) and it increases when we move away from thin point. Numerical results predict that the residual kinetic energy form smaller angles can be more than 10% of the upperbound of $E_{k,l}$ predicted previously from the theory.

Equation 4.10, derived from the energy conservation gives the relation between the liquid kinetic energy and the bubble volume, we verify this relation in figure 4.12*a* (assuming $\Phi_D = 0$). The equation predicts the evolution of liquid kinetic energy very well in the be beginning of the

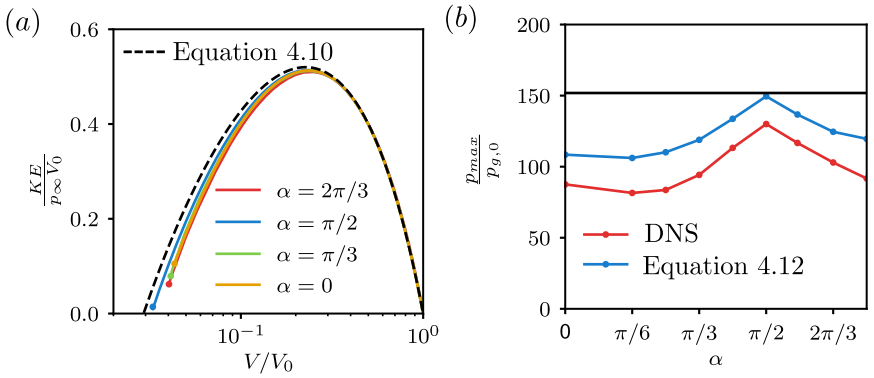


Figure 4.12: The DNS results for $p_\infty/p_{g,0} = 8$,$Re = \infty$, $We = \infty$ and varying contact angle. $(a)$ The evolution of kinetic energy with the bubble volume is shown along with equation 4.10 taking $\Phi_D = 0$. $(b)$ The maximum pressure is plotted for various values of $\alpha$ as obtained from DNS (red curve), we also the solution of equation 4.12 assuming $\Phi_D = 0$, the blue curve is obtained by calculating the integral of kinetic energy form DNS and black line is obtained assuming $E_{k,R} = 0$.

collapse phase, some differences becomes visible after the maximum kinetic energy. These are due to the numerical energy dissipation and the liquid compressibility effects which becomes increasingly important towards the end of collapse phase. Supponen et. al. [56] showed the gradual buildup of liquid pressure during the last stages of collapse resulting in to increasing importance of liquid compressibility effects. Therefore equation 4.12 slightly overpredicts the liquid the kinetic energy. Also the residual kinetic energy is clearly visible and even for $\alpha = 0$, we never reach the zero kinetic energy because of the numerical dissipation and liquid compressibility. In order to gain further insight into the influence of the angle on the peak pressures reached. In figure 4.12$b$, we plot the maximum pressure vs $\alpha$ obtained from DNS with red curve. As expected, the highest pressure is reached for the 90 degrees case which corresponds to a spherical bubble as $E_{K,R} \approx 0$. The solution of equation 4.12 is also plotted assuming $\Phi_D = 0$: while the blue line shows the points for which the residual kinetic energy is obtained from numerical simulations, the black line is obtained with the assumption that the residual kinetic energy is also zero. Clearly, the blue curve predicts well the trend in pressure reduction due to the liquid kinetic energy. A consistent shift between the red and blue curves is attributed to the damping due to liquid compressibility and numerical viscosity.

In figure 4.13$a$, we plot the residual liquid kinetic energy for different $p_\infty/p_{g,0}$ and for different $\alpha$. The residual kinetic energy increases as the $p_\infty/p_{g,0}$, therefore the penalization of gas pressure is also expected to increase. Moreover, Saade et. al. [109] showed that for spherical bubbles the effect of liquid compressibility also becomes more important for larger values of $p_\infty/p_{g,0}$. These effects are reflected in figure 4.13$b$ where we plot the maximum pressure as a function of driving pressure $p_\infty/p_{g,0}$ for various $\alpha \in \{0, \pi/6, \pi/3, 2\pi/3\}$ alongside the equation 4.12 is also plotted considering $E_{k,R} = 0, \Phi_D = 0$ (black line). As expected, the influence of the contact angle on the peak pressures is increasingly important as the pressure ratio increases that is why the peak pressures reached are significantly lower when the collapse is very intense (note that the plot is shown in log-scale) due to effects mentioned above. An future prospect of current study would

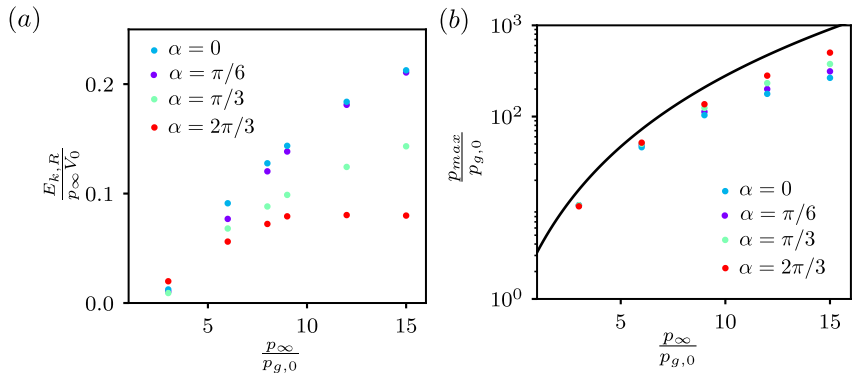


Figure 4.13: The DNS results for varying $p_\infty/p_{g,0} = 8$,$Re = \infty$, $We = \infty$ and different contact angle. $(a)$ The residual liquid kinetic energy at the instant of minimum volume is plotted for various $\alpha$ (colormap) and $p_\infty/p_{g,0}$. $(b)$ The maximum pressure is plotted as a function of $p_\infty/p_{g,0}$ for different alpha (colormap), the black curve corresponds to equation 4.12 assuming $\Phi_D = 0$, $E_{k,R} = 0$

be to understand the relative importance of these individual mechanisms (liquid compressibility, kinetic energy and dissipation) as function of $\alpha$ and $p_\infty/p_{g,0}$.

### 4.3.2 Experimental comparison

Now, we compare the numerical results with experiments and explain the dependence of jet direction on the initial bubble shape. Figure 4.14 shows the experimental setup described briefly here, more details are available in references [66] & [175]. The experiments were conducted in ENSTA Bretagne with Dr. Michel Arrigoni's group using a pulsed Nd:YAG laser (model quanta ray pro 350-10) that provides maximum of 3.5J of energy with Gaussian distribution in time having half maximum at 9.2 ns. This laser beam passes through a quarter wave plate and polarizer for modulating the energy and then focused using a plano-convex lens of focal length 250mm that creates a focal spot of 4mm in diameter on the aluminum plate. For bubbles shown with $\alpha > \pi/2$ the laser is focused on the water droplet attached to bottom of an aluminum plate (1 mm thick) kept at bottom of a water tank and for the bubbles with $\alpha < \pi/2$ the laser if focused on the top of this aluminum plate kept at the bottom of same tank. The laser energy is set to $50\%$ of maximum in case where $\alpha < \pi/2$ and we observe the cavitation phenomenon in the water tank using high speed camera.

First we discuss the case where the singularity is present (e.g. $\alpha > \pi/2$). The generation of bubbles with $\alpha > \pi/2$ is investigated using the setup described briefly above. The cavitation in the water drop induces shock waves in aluminum plate that leads to the appearance of multiple bubbles in the water tank, these bubbles interact to form a flat bubble with shape similar to spherical cap at maximum volume (figure 4.15 a). The snapshots are taken at every $0.1$ms, the interface from the second snapshot is extracted and fitted with an approximate spherical cap which gives $R_c = 7.56 \times 10^{-3} m$ and $\alpha = 0.727\pi$.

We reproduce the experimental conditions numerically using the numerical setup described in section 4.2.2. The minimum mesh size of $\Delta x = 60\mu m$, the far field pressure $p_\infty$ is 1 atm and the

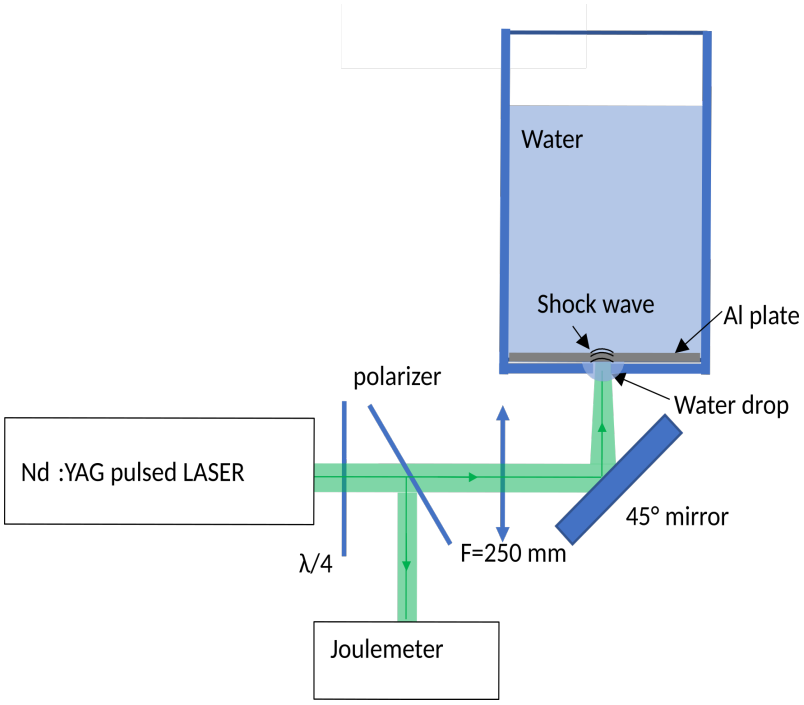


Figure 4.14: Experimental setup used to create flat bubbles.

pressure inside bubble is set to a low value (0.1 atm) selected by matching the collapse time from the experiments and the numerical simulations. We consider both surface tension and viscous effects in the numerical simulations with $Re \approx 75600$ and $We \approx 10500$. The numerically obtained bubble shapes plotted with red contours and scaled to bubble size in snapshot 2, these are subsequently overlaid on the experimental snapshots after 0.1ms. A very good agreement is seen between the numerical and the experimental bubble shapes, small differences subsist because of the simplification of the bubble shape during the bubble expansion, the influence of gravity, mass transfer and other effects that are not considered in the numerical simulations.

At the beginning of collapse phase the highest interface velocity is developed at edge of the viscous boundary layer (see figure 4.5*b*) that leads to the appearance of an annular jet parallel to the wall that further leads to a mushroom-like shape of the interface contour (see figure 4.15*a*). These results are consistent with previous numerical works of Lauer et. al. [94] and Koukouvinis et. al. [95]. Remarkably, when the collapse is strong enough and the jet reaches the axis of symmetry, a stagnation point appears there leading to a secondary upward jet normal to the wall. The re-entrant jet observed for $\alpha > \pi/2$ is not very conventional in cavitation and generates vortex ring structures similar to those observed by Reuter et. al. [96] which are persistent in nature and can travel large distances in comparison to bubble size. The generation of this vortex ring is illustrated numerically in figure 4.16*a* where the color maps show the vorticity field. A clear annular re-entrant jet is observed, followed by a mushroom like structure and the bubble detaches from the wall, consequently generates a jet in the upwards direction which eventually leads to formation of vortex ring. In the experiments we visualize this vortex by adding the dye in the bottom of the

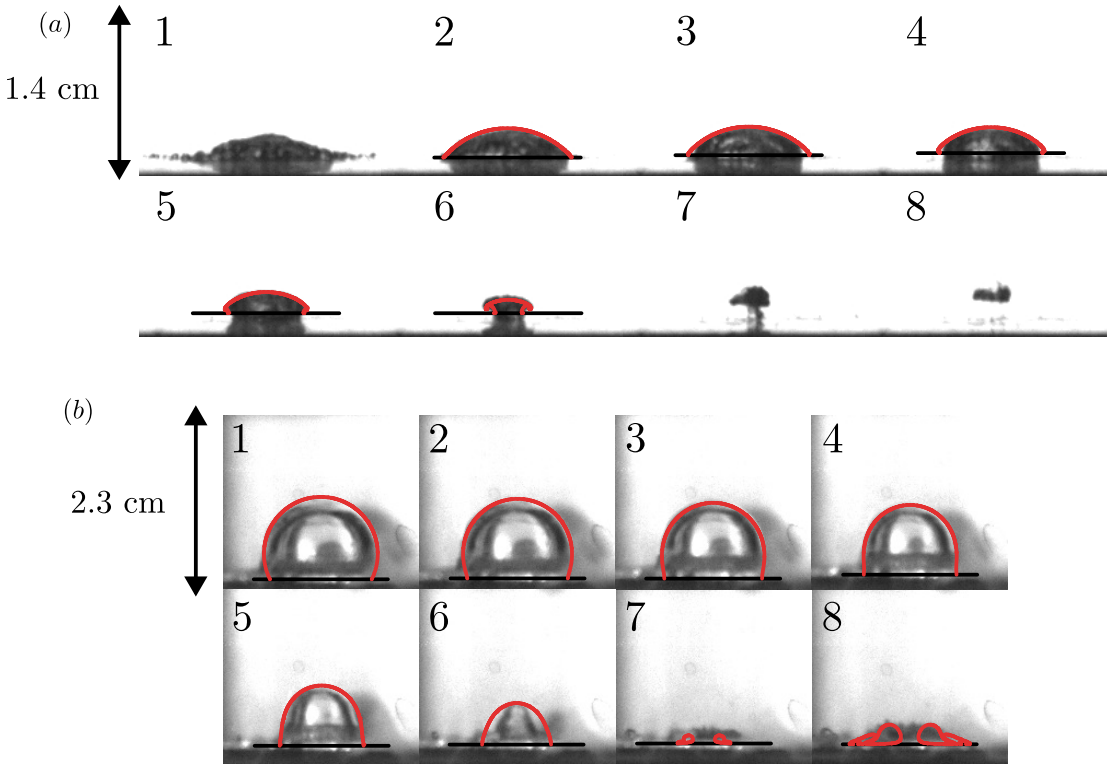


Figure 4.15: The snapshots of bubble shape are shown for the two representative cases, the numerical bubble shapes shown with red curves are overlaid at same times and scaled to same length as in experiments. $(a)$ Case where $\alpha > \pi/2$, each snapshots are taken every $0.1$ms $(b)$ Case where $\alpha < \pi/2$, each snapshots are taken every $0.125$ms.

tank (figure 4.16*b*) during the collapse of a flat bubble. This vortex ring can travel to long distance and induce unusual long range effects like free surface waves and jetting (see figure 4.16*c*).

The dynamics of bubbles with $\alpha < \pi/2$ (figure 4.15*b*) can be obtained using a classical experiment where a laser is focused directly in to the liquid very close to the wall. The bubble shape from snapshot 2 in figure 4.15*b* is approximated with a spherical cap that gives $R_c = 7.63 \times 10^{-3} m$ and $\alpha = 0.389\pi$. The interface contours obtained numerically are shown with the red curves and are scaled to size of the bubble size in first snapshot. In this case, the interface acceleration is minimum at the contact line and maximum at the tip of the spherical cap leading to a conventional high-speed liquid jet directed towards the wall (see figure 4.15*b*). This jet developed towards the wall impinges in to the solid surface causes cavitation damage. Similar dynamics have been described in several of previous studies by Naudè & Ellis and recently by Gonzalez et. al. [57, 91].

If the vortex dipole shown in figure 4.16 reaches a free surface, a jet is observed at the free surface. The appearance of this jet is significantly delayed with respect to the instant of the bubble collapse. Thus quite remarkably for bubbles with $\alpha > \pi/2$, the singularity in the potential flow solutions at very short time $t \ll t_c$ leads to an alteration in jet direction at times comparable to bubble collapse time $t \sim t_c$ which eventually leads to the formation of this vortex ring that can induce effects at time scales much larger the the collapse time $t \gg t_c$. Therefore the shape of bubble just

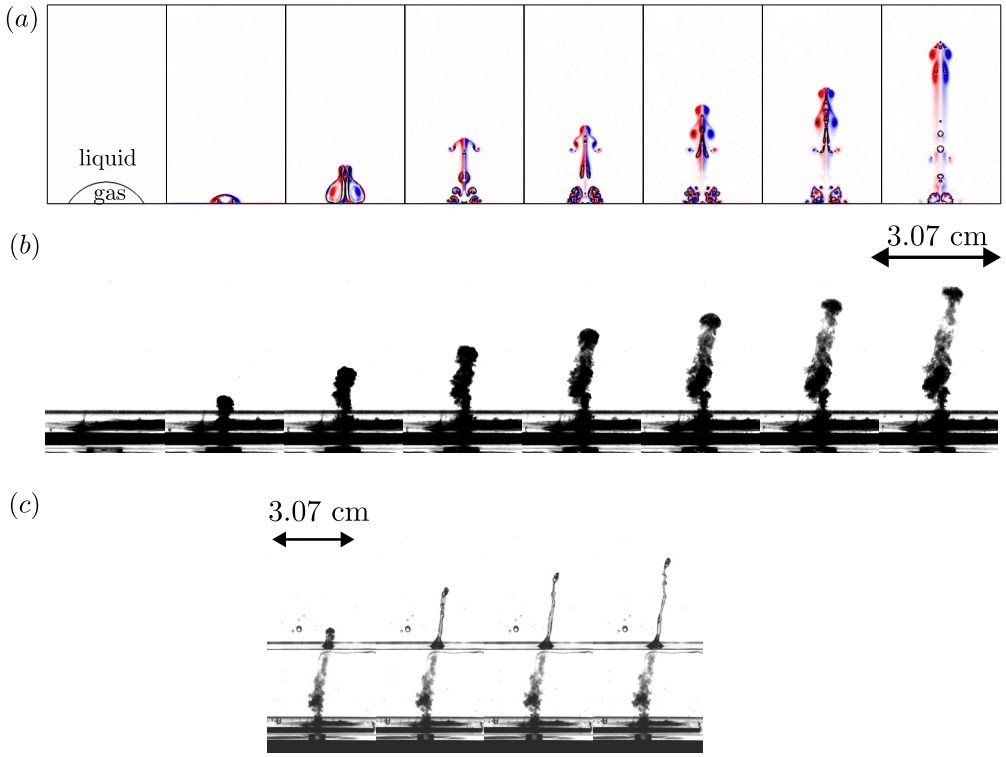


Figure 4.16: $(a)$ Bubble interface in black curve and the vorticity field in the colormap as obtained from DNS is shown at (consecutively from left to right) $\frac{tU_c}{R_c} = 0, 0.19, 0.3, 0.81, 1.00, 1.45, 1.95, 4.90$. The results are plotted for $\alpha = 2\pi/3$ and $Re = \infty$ $(b)$ The visualization of liquid flow field obtained by adding dye at the bottom of tank resulting from collapse of bubble is shown at every 2.5ms. $(c)$ Interaction of vortex ring with the free surface as observed from the experiments.

before the beginning of collapse phase turns out to be a very critical parameter that governs the overall bubble dynamics and its interaction with surrounding media.

### 4.3.3 Finite Reynolds number effects

Popinet & Zaleski [87] showed that for the small bubbles collapsing in the vicinity of a rigid wall, the jets can be suppressed due to the viscous effects. In this section, we use the DNS to quantitatively predict the range of size for which the viscous effect becomes important and the secondary jet opposite to the wall is suppressed. We take an ideal case of an air bubble with $p_{b,0} = 0.1$ atm and constant contact angle equal to 120 degrees collapsing in water at an ambient far field pressure. In this situation, the characteristic velocity of the collapse process stays constant and equal to 10 m/s and the initial radius of curvature is left as the unique parameter controlling the values of the Reynolds and Weber number.

In figure 4.17$a$ we show the maximum non-dimensional velocity reached during the collapse as a function of the Reynolds number. For Reynolds numbers above a given critical value $Re > Re_c = 100$ the influence of Reynolds on the peak velocities is only marginal. However, when

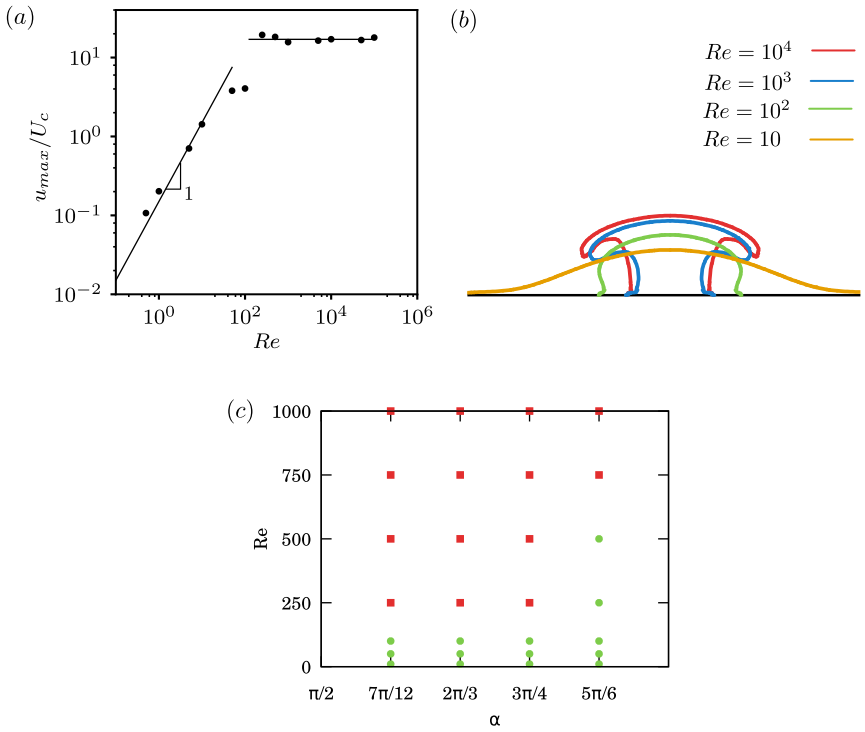


Figure 4.17: The DNS results for $p_\infty/p_{g,0} = 10$, varying $Re$, varying $We$ and varying contact angle. $(a)$ Peak of the non-dimensional velocity as a function of Reynolds number for an air bubble at $p_0 = 0.1$ atm collapsing in water at atmospheric pressure. $(b)$ Interface contours as a function of the Reynolds number at the instant of minimum radius. $(c)$ The critical Reynolds for appearance of jet opposite to the wall is shown as a function of contact angle, (red squares) are the points where the jet appear opposite to the wall and (green circles) corresponds to the points where the jet parallel to wall does not appear.

the Reynolds is below this critical value, the jet velocity drops dramatically further decaying with decreasing $Re$. This sudden change in the peak velocities is controlled by the appearance of jetting, which is not visible in numerical simulations for $Re \leq 100$ (see figure 4.17$b$). For a low pressure air bubble collapsing in water at atmospheric pressure these results reveal that the reversed re-entrant jet disappears for bubbles larger than $R_c > 10\mu$m. In a similar study we show the effect of $\alpha$ on $Re_c$ for infinite $We$, we mark the cases for which the jet appears with red squares and the ones for which it does not appear with green circles in figure 4.17$c$. Independent of the $\alpha$ and $We$ the numerical simulations predict that the $Re_c = 100$ for $\alpha < 5\pi/6$, and for very flat bubbles $\alpha \geq 5\pi/6$ this no longer holds and the viscous effects become important even at slightly larger values of Reynolds number as bubble height decreases significantly.

# 5 Multibubble cavitation

In this chapter, we use three dimensional numerical simulations to revisit the problem of multibubble cavitation discussed experimentally by Bremond et. al. (Phys. Fluids 17, 091111 (2005) Phys. Rev. Lett. 96, 224501 (2006)). In particular, we focus on understanding the asymmetry observed during the expansion and collapse of the bubbles. Numerical simulations reveal that the asymmetry during the expansion can be attributed to Bjerknes forces which result from the finite characteristic length of the pulse imposed by the finite effective speed of sound. These effects are amplified during the collapse due to Rayleigh–Taylor instabilities. We compare the numerical and experimental results of the asymmetry to clarify the role of the effective speed of sound on the process. Preliminary results show that the effective speed of sound in experimental conditions was smaller than the speed of sound in the pure liquids. The values of effective speed of sound estimated are consistent with the classical theory of wave propagation in the bubbly liquids, where small amount of the gas drastically reduces the effective speed of sound in the medium. To support this theory, we also show several tiny bubbles that stay in liquid bulk from the fragmentation of large bubbles during the subsequent experiments. This asymmetry is also shown to change the direction of the liquid jet generated during the last stages of collapse.

Figure 5.1 shows the experimental snapshots taken from the reference [55, 176], where the pits of 4 micron are created on silicon plate which is submerged in a large water tank. The pressure is dropped by a pulse generated from piezo-transducer similar to signal shown in figure 1.2*b*. The decrease in pressure causes the nuclei to become unstable and bubbles of the order of 100 micron are formed from the pit. Here, we show the top view of three cases: Two pits drilled at a distance of 200 micron shown in figure 5.1*a* left, two pits separated by a distance of 400 micron is shown in the figure 5.1*b*, thirty seven pits drilled in an hexagonal arrangement of pitch 200 micron shown in the figure 5.1*b*. The asymmetry in the pressure field can be caused by the pressure pulse itself or by the nearby bubbles which can result into asymmetric bubble shapes. In order to understand the source of asymmetry in the experiments, we perform three dimensional simulations under conditions similar to the experiments. Instead of the pits, we initialize a hemispherical cap shaped nuclei with the radius $R_{c,0}$ of 20 micron. The three dimensional simulations are costly and current computational resources do not permit us to resolve scales smaller the the 5 micron, therefore we are limited to use 20 micron nuclei in order to well resolve the initial nuclei with a minimum 8 point per diameter.

In the experiments, we speculate that the asymmetry for bubbles can be caused by following mechanisms: (a) Bjerknes forces and (b) Rayleigh–Taylor instabilities acting during the collapse stage only. In case of a single bubble exposed to the pressure waves, it is well known that the wave of finite length induces a force that is responsible for the translation of the bubbles. This force is known as primary Bjerknes (see reference [177, 178, 179, 180, 181]) force given as

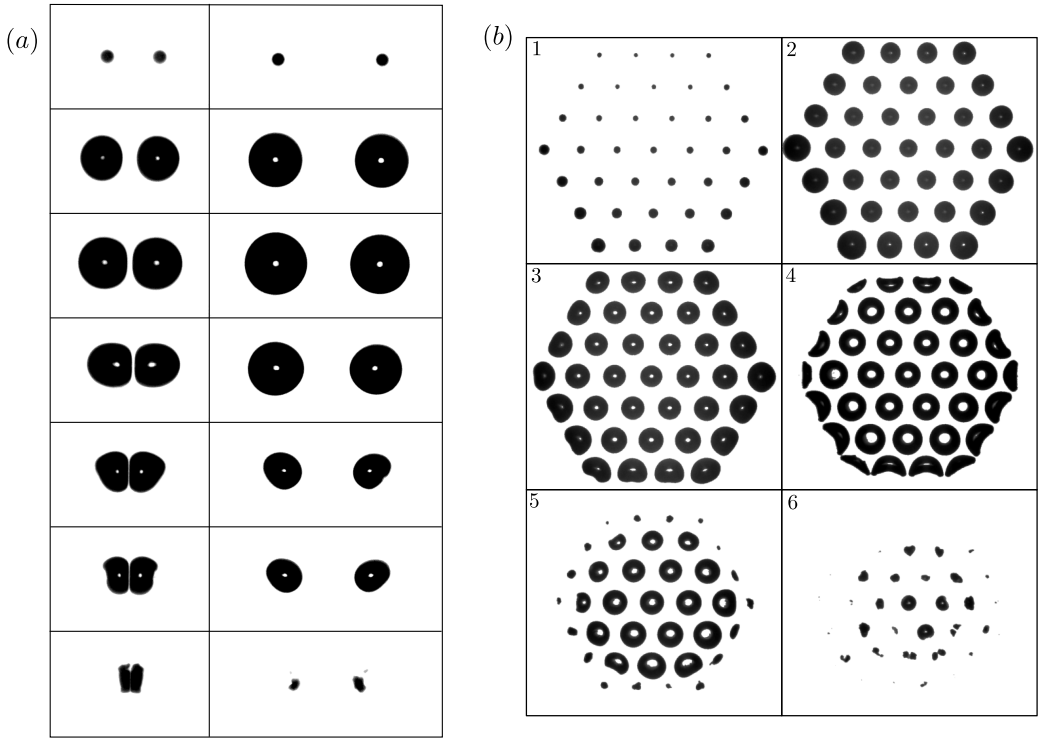


Figure 5.1: The top view of multiple cavitation bubbles nucleating from pits ($4\mu$m diameter) and collapsing in contact with the rigid wall. $(a)$ A pair of bubbles nucleating from two pits separated by a distance of $200\mu$m and $400\mu$m is shown in left and right panel respectively. The snapshots from top to bottom rows in both columns belong subsequently to time, $t(\mu\text{s}) \in \{5, 8, 13, 17, 22, 23, 24\}$. $(b)$ A cluster of thirty seven bubbles nucleating from the pits drilled in a hexagonal arrangement having a pitch distance of $200\mu$m. The snapshots are numbered from $1-6$ which correspond to time, $t(\mu\text{s}) \in \{4, 9, 17, 31, 38, 44\}$. The figure is adopted from experiments of Bremond et. al. [55, 176].

$$\mathbf{F}_b = -\langle V(t)\boldsymbol{\nabla} p(\mathbf{x},t)\rangle_t, \tag{5.1}$$

where $V(t)$ is the bubble volume at instant $t$, $\boldsymbol{\nabla} p(\mathbf{x},t)$ is the pressure gradient at location $\mathbf{x}$ and instant $t$ and $\langle . \rangle_t$ is the temporal average. If the bubble is attached to a wall, the friction causes the resistance to the movement of contact line and the force induces asymmetry at the bubble interface. In the case of multiple bubbles, the pressure gradients can also result from nearby bubbles resulting into the secondary Bjerknes forces. It is also well known that the small non-spherical disturbances in the bubble shape can grow unstably (only) during the acceleration phase of the collapsing bubbles, famously known as Rayleigh–Taylor (RT) instabilities [171, 182]. Therefore during the expansion, the asymmetry is attributed only to the Bjerknes forces, and these disturbances are amplified during the collapse phase due to RT instabilities.

## 5.1 Setup

The simplified 2D schematic of the problem is shown in figure 5.2*a*. The initial nuclei (shown with circles) of radius $R_{c,0}$ are separated by a distance $d$ and exposed to a 1D pressure pulse of amplitude $\Delta p = 15$MPa and a characteristic length $(L_p)$(defined from the pulse duration $(T_p)$ given from hydrophone measurements). The pressure pulse propagates with an effective speed of sound $c_e$ towards the nuclei in the direction normal to the line joining these nuclei as shown in with red arrow. Note that problem is symmetric about the $x = 0$. The non-dimensional parameters relevant for the problem are same as shown in chapter 2 where the characteristic velocity is defined with the amplitude of pressure pulse as $U_c = \sqrt{\Delta p/\rho_l}$. In addition, the separation distance $(d)$ between the bubbles and the characteristic length of the pressure pulse yields two more non-dimensional numbers i.e. $d/R_{c,0}$ and $L_p/R_{c,0}$. The non-dimensional numbers that we explore in this chapter are *Re*, *We*, $L_p/R_{c,0}$, $d/R_{c,0}$. As a physical justification to change in $L_p$, we hypothesize the existence of small gas bubbles fragmented from bigger bubbles in subsequent cavitation experiments that might be responsible for changing $c_e$ in the liquid media. Both $c_e$ and $L_p$ are linearly related to each other such that $L_p = T_p c_e$ for constant duration of pulse $(T_p)$ measured in the experiments, therefore we interchangeably use both $L_p$ and $c_e$ to describe the effect of pressure pulse. Also note that $L_p/R_{c,0}$ is not an independent non-dimensional number, it is an alternative to Mach number defined in chapter 2.

The computational setup used for the problem is shown in figure 5.2*b*. We use a cubic domain of size varying from 26mm in the case of bubble pairs to 130mm in the case of bubbles cluster. The color map shows the projection of the initial pressure field that is taken from the hydrophone measurements of the Bremond et. al. [55]. The pressure perturbation $p'$ is transformed into spatial domain as $p(y) = p_0 + p'(y_0 + c_e t)$. Other primitive variables are initialized using the linear plane wave solution for small perturbation (see reference [142]). The bottom boundary is considered as wall where we initialize the hemispherical nuclei of size in the range $R_{c,0} \in (20, 50)\mu$m and $\alpha = 90°$. We use the Navier-slip model (see section 2.3) for the contact line where we have the numerical slip length $(\lambda_{num} = 5\mu\text{m})$. For other boundaries, we have used standard reflecting boundary conditions. We make huge domains in order to make sure that the reflected pressure pulse never affects the simulation till the end of the simulations. A zoomed view of the bottom boundary is also shown for a particular case of bubble pair. In the zoomed view, we show the

initial nuclei and the projection of the grid on the bottom boundary. The grid is progressively refined from to $40\mu$m to the smallest grid size of $5\mu$m near the nuclei. Note that owing to the mesh refinement capabilities of Basilisk, it is possible to resolve the large scale separation between the characteristic length of the pressure pulse and the bubble (up to 3 orders of magnitude). In this framework, we study the dynamics of bubbles as a function of effective speed of sound in liquid $c_e$, size of initial nuclei $R_{c,0}$, numerical slip length $\lambda_{num}$, $d$ and compare our numerical results with the the experimental results. The simulations are run on Swiss super computer *Piz Daint* where a typical 3D simulation takes around 15h on 7200 processors with hyperthreading and includes around 1.3 Million grid points.

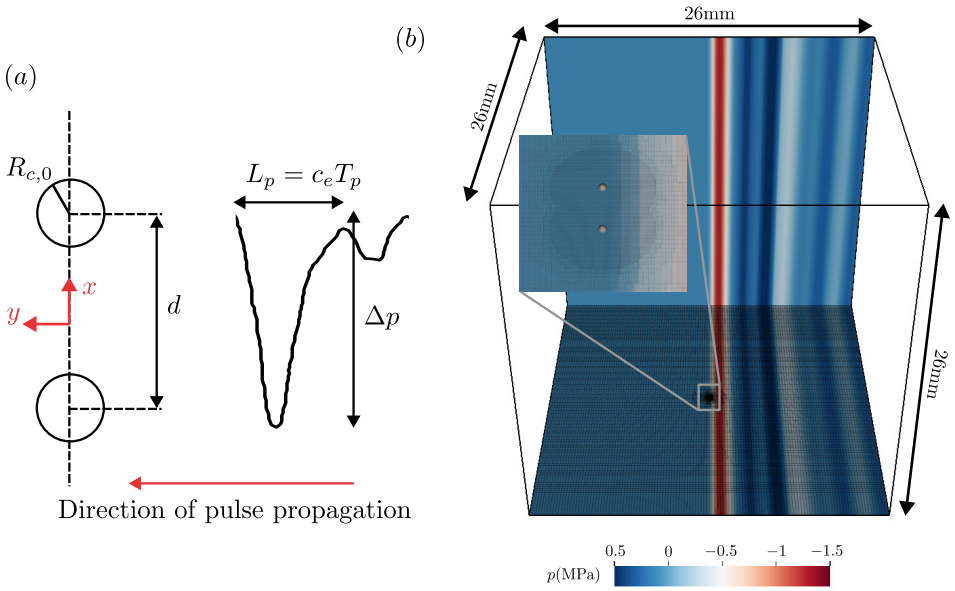


Figure 5.2: $(a)$ The simplified 2D schematic of the problem where the initial nuclei (shown with circles) of radius $R_{c,0}$ are separated by a distance $d$ and exposed to a 1D pressure pulse of amplitude $\Delta p = 15$MPa and a characteristic length $(L_p)$ (defined from the pulse duration $(T_p)$ given from hydrophone measurements). The direction of wave propagation is shown with red arrow. $(b)$ The 3D computational setup used in current study where the projected color-map corresponds to the initial pressure field taken from the experiments (reference [176]). A zoomed-in view of initial nuclei and the projection of the numerical grid on the bottom boundary of the domain are shown in the inset figure.

## 5.2 Bubble pair

In this section, we focus on the problem of a pair of bubbles separated by some distance and we investigate the effect of $d$,$c_e$ and $R_{c,0}$.

### 5.2.1 Description of Asymmetric behavior

We start by discussing the numerical results for bubble evolution of bubble pairs in four different cases where $d \in \{200, 400\}\mu$m and $c_e \in \{500, 1500\}$m$/s$. The speed of sound in water at normal temperature and pressure conditions is around 1500m/s, but here we also show $c_e = 500$m/s for the reasons that become clear later. We fix the size of nuclei to $20\mu$m and slip length to $\lambda_{num} = 5\mu m$.

In figure 5.3$a$ and $b$ we show the snapshots of the top view of the bubbles at different times for $d = 200\mu$m and $400\mu$m respectively. The left row in each panel corresponds to $c_e = 1500$m/s while right row is obtained for $c_e = 500$m/s. The isobars are also shown with color contours. The pressure pulse travels in $y$ direction and causes first a drop in pressure resulting into a rapid expansion of bubbles. At later times, the bubbles reach their maximum radius and then collapse under the action of ambient pressure. Qualitatively, the numerical results for $c_e = 500$m/s is better representation of the bubble shapes observed in experiments (figure 5.1) for both $d$ equal to 200 and $400\mu$m. Especially, the asymmetric behavior of the bubble observed during the collapse stage which is insignificant in the case of $c_e = 1500$m/s. In order to quantify the asymmetric response of bubble, we define the asymmetry parameter $(\mathcal{A}_y)$ as the shift in the centroid of bubbles in the direction of the motion of pressure pulse, such that $\mathcal{A}_y = y_c(t) - y_0$ where $y_c(t)$ is the bubble centroid at an instant $t$ (see figure 5.3$c$). In figure 5.3$d$, we show the evolution of $\mathcal{A}_y$ obtained numerically (lines) for all the cases. At beginning of expansion phase, $\mathcal{A}_y$ becomes negative indicating that the bubble centroid shifts downwards resulting from expansion being biased towards the lower half $(y < y_0)$. Then, $\mathcal{A}_y$ changes sign indicating that the collapse followed by expansion of bubbles is also biased in the lower half $(y < y_0)$. This causes cone like asymmetric bubble shape at $t = 22$ and $23\mu$s for $c_e = 500$m/s, while this effect remains insignificant in the case of $c_e = 1500$m/s. Clearly the experimental values of $\mathcal{A}_y$ (dots in figure 5.4$d$) in both cases ($d$ = 200 and $d = 400\mu$m) are well represented by $c_e = 500$m/s.

### 5.2.2 Effect of effective speed of sound

In order to discuss the effect of effective speed of sound in detail, we focus on a particular case of bubble nucleating from pair of hemispherical nuclei of size $20\mu$m separated by a distance of $200\mu$m, $\lambda_{num} = 4.4\mu$m and varying $c_e$ in range $(208, 3333)$m/s. The temporal evolution of the asymmetry parameter is shown in figure 5.4 for different values of $c_e$. The temporal behavior of $\mathcal{A}_y$ is very similar in all the cases, as described before. The experimental measurement of $\mathcal{A}_y$ (black cross) is also overlaid, and the inset figure shows a comparison between the numerical (red points) and the experimental bubble shapes at $t = 22\mu$s and $23\mu$s. The comparison of numerical and experimental results for $\mathcal{A}_y$ suggests that $c_e \approx 500$m/s best represent the asymmetry in the experiments which explains the choice of an effective speed of sound $c_e \approx 500$m/s in figure 5.3.

As mentioned previously, the asymmetry is the result of Bjerknes forces during the expansion phase. The symmetry of the problem in $y - z$ plane implies that the secondary Bjerknes forces act only in $x$ direction hence it does not affect $\mathcal{A}_y$. Therefore, the primary Bjerknes forces remains to the main mechanism controlling $\mathcal{A}_y$ by the elimination process. The component of primary Bjerknes force in $y$ direction at an instant is

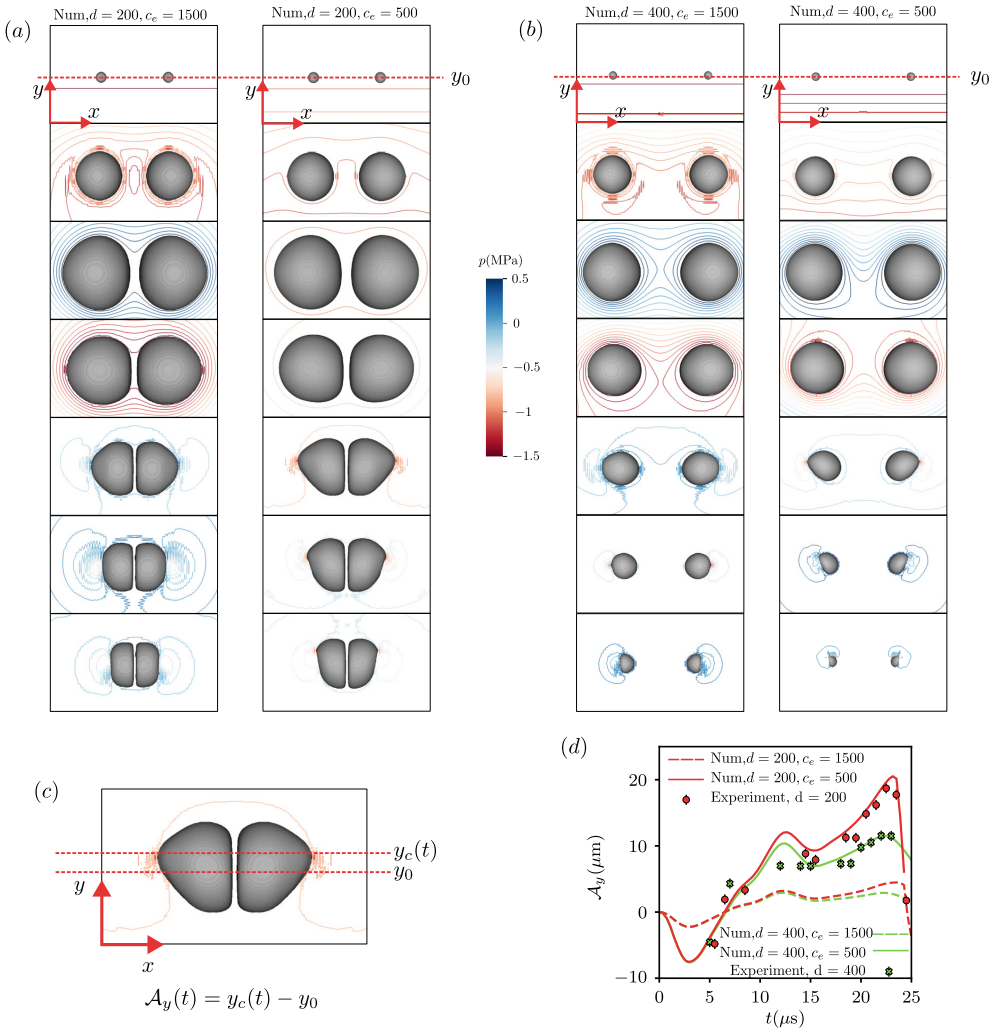


Figure 5.3: In this figure, we compare the numerical results for two different values of effective speed of sound i.e. $c_e = 1500$m/s and $c_e = 500$m/$s$. The bubble pair is evolving from hemispherical nuclei of size $20\mu$m and $\lambda_{num} = 5\mu$m. In panel $(a)$ and $(b)$, the top view of the bubble shape and pressure field are displayed subsequently from top to bottom at time, $t(\mu s) \in \{0, 3.5, 8.7, 13, 22, 23, 24\}$. $(a)$ When the separation distance between the nuclei equals to $200\mu$m with $c_e$ equal to 1500m/s on left and $c_e$ equal to 500m/s on right. $(b)$ When the separation distance between the nuclei equal to $400\mu$m with $c_e$ equal to 1500m/s on left and $c_e$ equal to 500m/s on right. $(c)$ A particular snapshot showing the definition of the asymmetry parameter $\mathcal{A}_y$ defined as shift of the bubble centroid in $y$ direction. $(d)$ The time-evolution of $\mathcal{A}_y$ obtained from the numerical simulations for all the cases discussed in figure 5.3 $a$ and $b$ is presented along with its comparison with experimental data, the error bars are equal to the one pixel size ($1.53\mu$m) in the experiment snapshots.

$$F_{b,y} = -V_b \frac{\partial p}{\partial y} \approx -2V_b \frac{\Delta p}{L_p}, \tag{5.2}$$

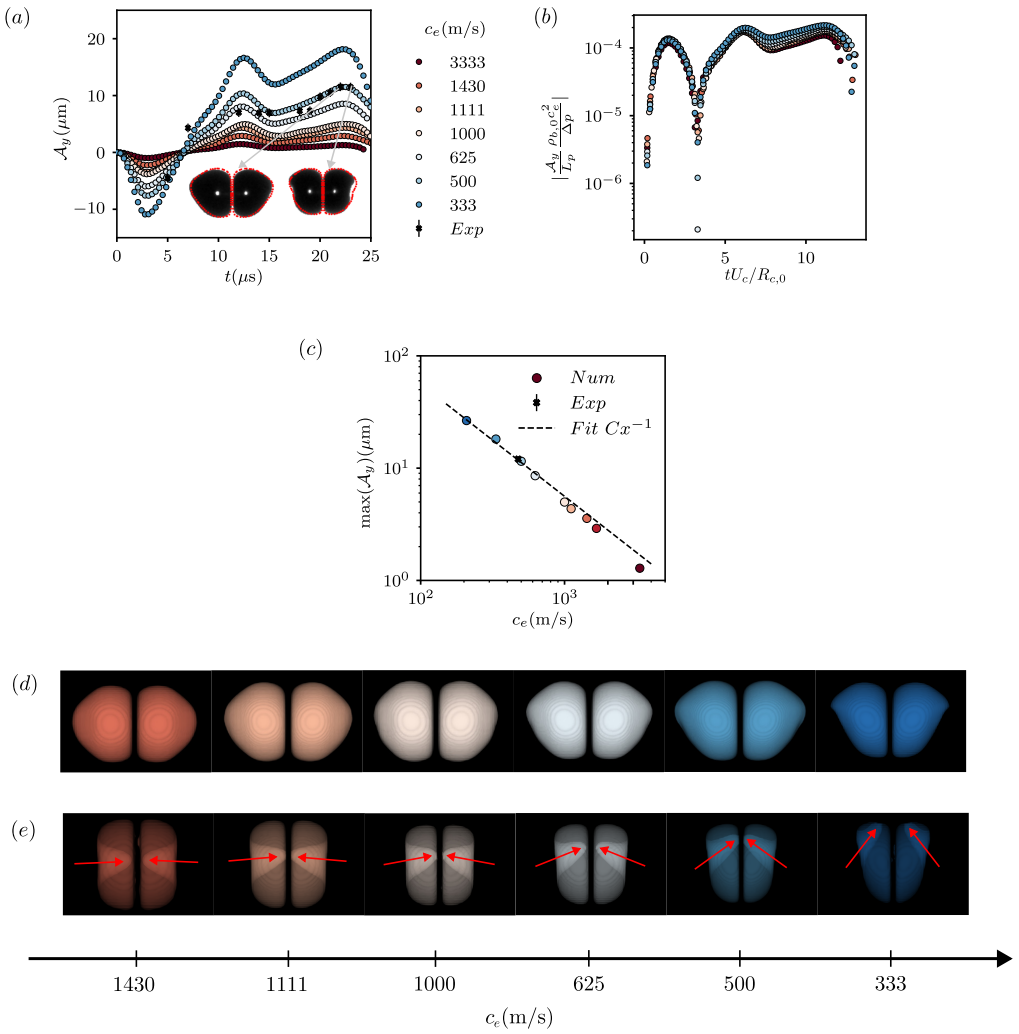


Figure 5.4: Effect of effective speed of sound on the asymmetry for a particular case where bubbles are evolving from a pair of hemispherical nuclei of size 20$\mu$m each, separated by a distance of 200$\mu$m and $\lambda_{num} = 5\mu$m. $(a)$ The time evolution of $\mathcal{A}_y$ is shown as a function of the effective speed of sound in liquid (colormap), alongside the experimentally obtained values (black crosses). The experimental bubble shapes overlaid with their numerical counterpart (red dots) at $t = 22\mu$s and 23$\mu$s are illustrated in the inset figure. $(b)$ The evolution of non-dimensional $\mathcal{A}_y$ obtained using the scaling predicted from equation 5.3 for different $c_e$ (color scale) $(c)$ The max value of the asymmetry parameter ($\max(\mathcal{A}_y)$) is plotted as function of the effective speed of sound along with the experimental point (black cross) where its $c_e$ is obtained by matching $\max(\mathcal{A}_y)$ with the numerical data. A fit of overall data (dashed line) is also plotted to show $\max(\mathcal{A}_y)$ decays like $c_e^{-1}$ as predicted by equation 5.3. $(d)$ The bubble shapes at the instant of $\max(\mathcal{A}_y)$ in figure are shown for different effective speed of sound in the liquid. $(e)$ The semi-transparent bubble shapes are shown to visualize the jet generated during the last stages of collapse whose direction is highlighted with red arrows.

where we approximate pressure induced by the pulse varies linearly in $y$ direction. A decrease in $L_p$ ($\propto c_e$) causes stronger gradients of pressure thus an increase of the Bjerknes force and asymmetry as seen in figure 5.4. Assuming that the bubble deformation scales with the Bjerknes force as $F_{b,y} \sim \rho_{b,0} V_{b,0}(y_c - y_0)/T_p^2$, we get a scaling for asymmetry parameter as

$$\mathcal{A}_y \sim -2\frac{T_p}{\rho_{b,0}}\frac{\Delta p}{c_e}. \tag{5.3}$$

In figure 5.4*b*, we show the evolution of non-dimensional $\mathcal{A}_y$ obtained using the scaling given by equation 5.3. Since, all curves for different $c_e$ overlap, the asymmetry scales well with the Bjerknes forces specially during the expansion phase ($tU_c/R_{c,0} < 6.5$). Some differences are detectable during the collapse phase ($tU_c/R_{c,0} > 6.5$) which can be an outcome of RT instability which is known to grow during when the interface accelerates during the collapse phase. As expected from equation 5.3, max($\mathcal{A}_y$) also scales well with $1/c_e$ (see figure 5.4*c*) with some differences due to RT instabilities. The bubble shape at the instant of maximal asymmetry in these cases (different $c_e$) also shown in figure 5.4*d*. The collapse of the pair of bubbles during the last stages is shown to form a liquid jet parallel to the wall in figure 5.4*e* (for similar reasons described in chapter 4). The direction of the jet changes as an outcome of the bubble asymmetry which is highlighted with the arrows. At sufficiently small values of the $A_y$, the jet is directed along the line joining the centroids of two bubbles. However, for large values of $\mathcal{A}_y$, this jet shifts in the direction of the propagation of pressure pulse.

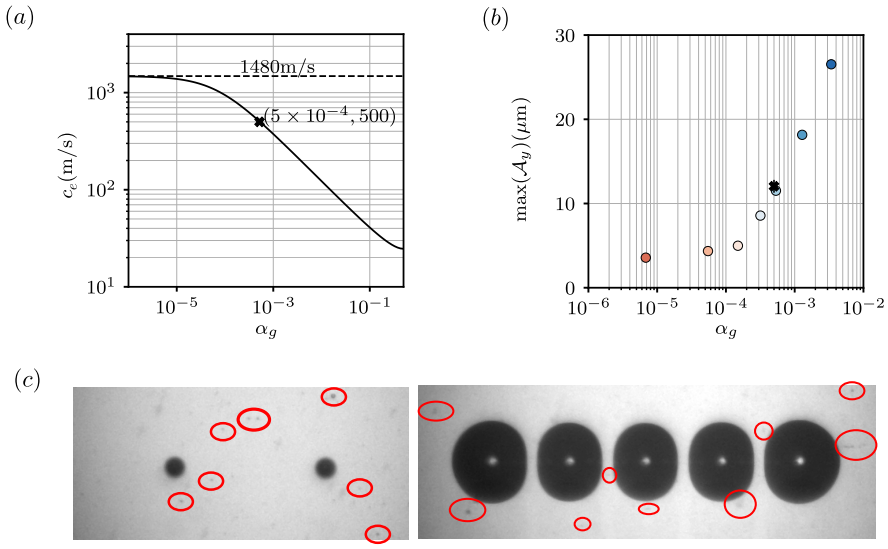


Figure 5.5: (*a*) The decrease in the effective speed of sound for a mixture of liquid and dispersed gas is shown as function of the volume fraction of the gas phase ($\alpha_g$ given by the equation 5.4), the point obtained by matching $\mathcal{A}_y$ from experiments and numerical simulations is also drawn with black cross. (*b*) The variation of max($\mathcal{A}_y$) with the volume fraction of the dispersed gas phase calculated from the effective speed of sound using equation 5.4. (*c*) The tiny fragmented bubbles seen during the cavitation experiments are highlighted with red circles along with the big bubbles nucleating from the pits for the case of two pits and five pits on left and right respectively.

Why do we need to set low values of $c_e$ to better reproduce the asymmetry effects from the experiments? It is well known that the presence of a small concentration of gas can dramatically decrease the speed of sound (see references [171, 183]). This can be predicted from the linear theory of wave propagation for homogeneous and mono-dispersed gas concentrations ($\alpha_g$) as

$$\frac{1}{c_e^2} = [\alpha_g c_g + (1-\alpha_g)c_l]\left[\frac{\alpha_g}{\rho_g c_g^2} + \frac{1-\alpha_g}{\rho_l c_l^2}\right] \tag{5.4}$$

In figure 5.5$a$, we plot the equation 5.4 in the log-log scale where the value $c_e = 500$m/s estimates an $\alpha_g = 5\times10^{-4}$. Such a small gas concentration can result from the fragmentation of the bubbles during the series of experiments carried out at very small intervals of time ($\sim 1\mu s$). Note that these experiments were repeated rapidly to capture the images of bubbles from consecutive experiments by means if stroboscopy technique (owing to repeatability). Extremely small bubbles of the order of $1\mu$m are observed to remain in the liquid media from the previous experiments (see figure 5.5$c$). Equation 5.4 is applicable when the pulse has small amplitude and the characteristic frequency of the pulse is much smaller the bubble resonance frequency ($\omega_p/\omega_b << 1$). In the experiments, the size of small bubbles is few microns and the characteristic time scale of the pressure pulse (or the duration of low pressure) is approximately $5\mu s$, and therefore the ratio of frequencies is small $\omega_p/\omega_b \approx 0.037$. It is also important to remark that the theory assumes an homogeneous mixture, while in experiments the gas concentration can vary locally. Both non-linear effects and gradient concentrations will certainly introduce some uncertainties in the use of the very simplified model used here.

Figure 5.5$b$ quantifies the influence of the gas concentration on the asymmetry of the bubble response. As we can see, most likely the experiments were done in a regime where the results were significantly influenced by presence of small amounts of the gas phase in the bulk phase.

### 5.2.3 Effect of the size of nuclei

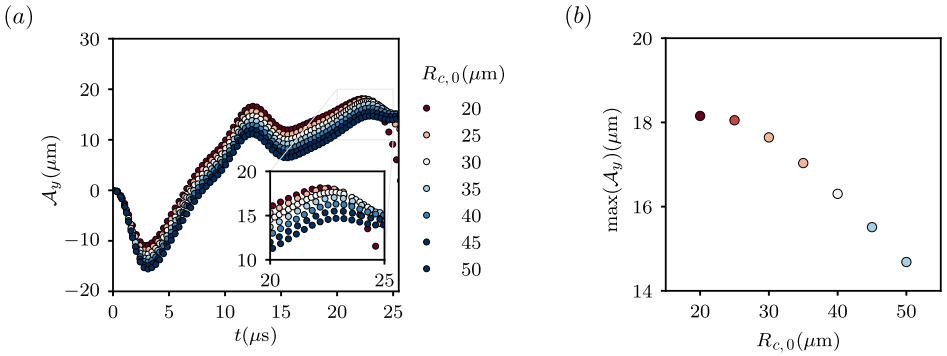


Figure 5.6: The numerical results for the particular case where the effective speed of sound is assumed to be 333m/s, $\lambda_{num} = 5\mu$m, $d = 200\mu$m and varying $R_{c,0}$. $(a)$ The time evolution of parameter $\mathcal{A}_y$ is shown for different size of initial nuclei depicted with the colormap. A zoomed-in view around the max$(\mathcal{A}_y)$ is also shown in the inset figure. $(b)$ The value of max$(\mathcal{A}_y)$ corresponding to the maximum in figure 5.6$a$ is plotted as a function of the size of the nuclei.

Bremond et. al. [55] showed that the bubble evolution is represented accurately by the Rayleigh–Plesset model and they calculated the equivalent radius of initial hemispherical nuclei (input for RP model) as $R_0 = (3HD^2/8)^{1/3}$, where $D$ is the pit diameter and $H$ is the pit height. This gives $R_0 = R_{c,0} \approx 5\mu$m, whereas in the current study we are limited by computational resources to resolve length scale smaller than $20\mu$m. In order to understand the effect of the initial nuclei size, we do a parametric study for the case where pair of nuclei is separated by $200\mu$m by fixing $c_e = 333$m/s, $\lambda_{num} = 5\mu$m, and vary $R_{c,0}$ in the range $(20, 50)\mu$m. The evolution of $\mathcal{A}_y$ and the max$(\mathcal{A}_y)$ are shown in figure 5.6 $a$ and $b$ respectively. In the range of $R_{c,0}$ considered the $\mathcal{A}_y$ varies little with the size of initial nuclei and its effect is secondary in comparison to the effect of $c_e$. Moreover, max$(\mathcal{A}_y)$ is increasing as the nuclei size decreases and further saturates for smaller $R_{c,0}$. The decrease in $\mathcal{A}_y$ upon increasing $R_{c,0}$ is probably due to the increased shielding effect caused by the neighboring bubble which is increasingly important for fixed inter-bubble distance $(d = 200\mu$m). Note that if these results for $\mathcal{A}_y$ were to be extrapolated to $5\mu$m nuclei, the previous estimates of $c_e$ would have been under-predicted, hence the $\mathcal{A}_y$ in the experiments could be explained from even smaller gas concentration. Another important outcome of changing the nuclei size is that the cavitation process lasts slightly longer for bigger nuclei in comparison to smaller ones. This is in agreement with the results of Bremond et. al. [55] (see figure 3 in their article) for single bubble and varying nuclei size. This effect is caused by the liquid inertia which increases in case of bigger nuclei.

## 5.3 Multiple bubbles setup

Now, we solve more challenging problems with multiple bubbles. Firstly, we solve for the problem of five bubbles in a line and secondly, a cluster of thirty seven bubbles in a hexagonal arrangement that are nucleating from the hemispherical nuclei. We repeat the the same procedure of varying the effective speed of sound to investigate the influence of $c_e$ on the asymmetry by fixing $R_{c,0} = 20\mu$m, $\lambda_{num} = 5\mu$m.

### 5.3.1 Five bubbles in a line

In the case of five bubble in a line, the best correspondences among the numerical and experimental results is observed for $c_e = 667$m/s. In figure 5.7$a$, we show the top view of the experimental and the numerical bubbles left and right panel respectively. A very similar dynamics is observed for both numerical and the experimental snapshots except for the $t = 4\mu$s, where the numerical bubbles are comparatively bigger. This effect is due to the difference in the size of initial bubble nuclei for the experiments and the numerical simulations. Similar to the bubble pair, the bubbles expand and collapse with a bias towards the $y < y_0$, and the jet generated during the last stages of collapse is also directed at an angle to the line joining the centroids of initial nuclei. We again use $\mathcal{A}_y$ i.e. shift of centroid of gas mass to quantify asymmetry (figure 5.7$b$) that matches well with the experiments.

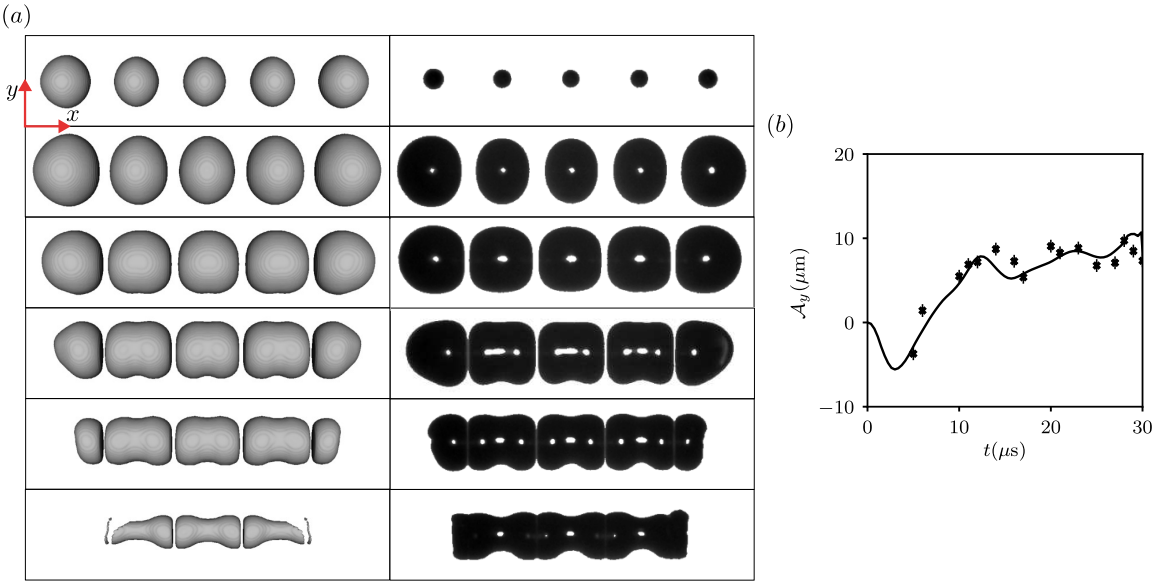


Figure 5.7: $(a)$ The top view of the five bubbles in straight line configuration, as discussed in reference [55]. The numerical results are shown in left panel, where the bubble expands from $20\mu$m hemispherical nuclei, $\lambda_{num} = 5\mu$m and the effective speed of sound is assumed to be $667\mathrm{m}/s$. The experimental bubble shapes are also shown in the right panel. In both columns, each row from from top to bottom correspond to time $t(\mu s) \in \{4, 9, 15, 21, 24, 28\}$. $(b)$ The evolution of asymmetry parameter obtained from the numerical simulations (solid line) and the experiments (cross), the error bar is equal to one pixel size (i.e. $1.53\mu$m) in the experiment snapshots.

### 5.3.2 Cluster of bubbles

Finally, we simulate the most challenging case of a cluster of thirty seven bubbles in a hexagonal arrangement where we repeat exactly same procedure of varying $c_e$ for $20\mu$m hemispherical nuclei and $\lambda_{num} = 5\mu$m in order to reproduce experimental measurements. Remarkably, the largest admissible value, 1480m/s, is found to better reproduce the experimental results. The corresponding numerical results are shown in figure 5.8. Similar to the previous case, the bubbles in the lower half domain($y < y_0$) nucleate earlier reaching larger negative values of $\mathcal{A}_y$ compared to all the previous cases. This effect is clearly seen in both the experimental and numerical results (Figure 5.1*b* and 5.8). Consistent with the previous observations, the numerical results predict the change in the sign of $\mathcal{A}_y$ which shift from negative to positive during the collapse phase. However, the numerical simulation results during the collapse phase differ significantly from experiments, where the collapse process is more chaotic (see figure 5.1*b*) and the the parameter $\mathcal{A}_y$ does not match as satisfactory as in previous cases (see figure 5.8*b*). The disparity in the numerical and experimental results during the collapse phase could be because of following reasons: In the experiments, the transducer creates a spherical pressure pulse which can lead to more complex interaction with the cluster as compared to the 1D wave assumed in the numerical study. Also the cavitation process for the cluster of bubbles lasts much longer and there might be some reflected waves from the walls of container that can promote the asymmetries in other directions causing chaotic bubble collapse.

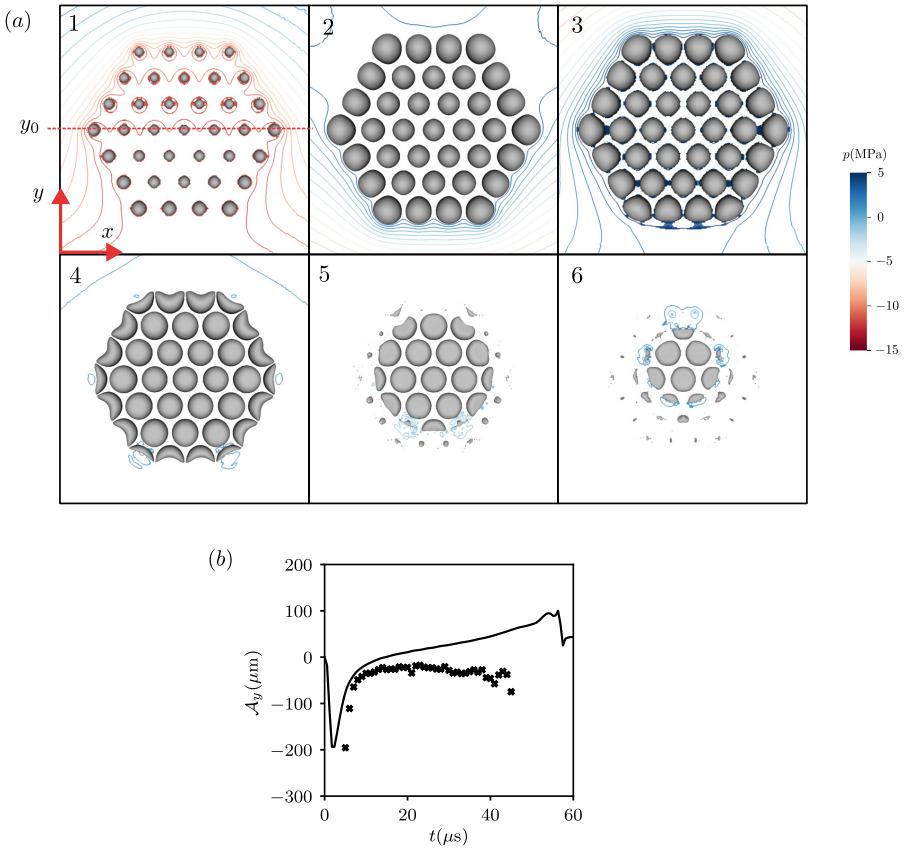


Figure 5.8: $(a)$ Top view of the cluster of 37 bubbles in hexagonal arrangement expanding from $20\mu$m hemispherical nuclei,$\lambda_{num} = 5\mu$m. Assumed effective speed of sound is $1480\text{m}/s$, isobars are shown with colormap and the panels are numbered $1-6$ at time $t(\mu s) \in \{3, 20, 28, 42, 52, 55\}$. $(b)$ The evolution of asymmetry parameter obtained from the numerical simulations (solid line) and the experiments (cross) are also shown.

Finally, it is also important to remark that the effective speed of sound required to reproduce the experiments with a small number of bubbles (500m/s for bubble pairs, 667m/s for five bubbles) was significantly smaller than in this case (1480m/s). One possible explanation for this behavior might be that while the large scale interactions between the bubble cluster and the pressure pulse are modified by the effective speed of sound in medium, the direct bubble-bubble interactions between bubbles take place almost instantaneously and we introduce errors when modifying the effective speed of sound of the medium. Thus, when the number of bubbles present in the system is large, direct bubble interactions become important, and the best fitted value of $c_e$ tends to the value of a pure liquid at expenses of representing less accurately the interaction between the overall bubble cluster and the external pulse. When the number of bubbles is reduced, the interaction between the bubble cluster and the external wave become increasingly important to determine the asymmetry which results in a decrease in the effective speed of sound of the medium. Nevertheless,

this case is extremely delicate and difficult to control, hence this discrepancies during the collapse phase are not surprising rather, the agreements during the expansion phase are remarkable.

## *Appendix A: Effect of numerical slip length*

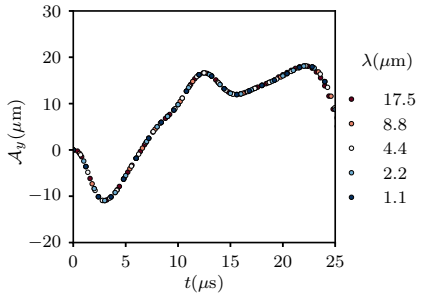


Figure 5.9: The time evolution of parameter $\mathcal{A}_y$ is shown for varying values of numerical slip length for the bubble pair case.

We also study the effect on slip-length on the asymmetry (see figure 5.9) for a particular case where the pair of initial nuclei is separated by $200\mu$m, $c_e = 333$m/s and $R_{c,0} = 20\mu$m and varying $\lambda_{num}$ in the range $(1.1, 17.5)\mu$m. As expected the slip length and the contact line motion does not influence the bubble shapes, similar to the results of chapter 3 and chapter 4. This is an indirect verification that the ideas discussed in this chapter are not sensitive to the modeling of contact line.

# 6 Conclusions and future perspectives

In this work, we focused on understanding the dynamics of cavitation bubbles attached to a rigid wall. The study is structured into in three problems attributed to different aspects of the cavitation bubbles: Single bubble heterogeneous nucleation, single bubble collapse and multi-bubble nucleation and collapse dynamics. Here, we discuss the conclusions and future perspectives of each one of these, the major takeaway messages from each chapter are highlighted with color boxes for a quick reference.

In chapter 3, we investigate the stability of spherical cap shaped gas nuclei attached to a rigid wall and subjected to a sudden pressure drop. Using the quasi-static theory and two limiting behaviors of the contact line i.e. freely moving contact line and the pinned contact line, we show that the response of bubble can result in one of the three situations (a) Bubble finds a new equilibrium size and oscillate near it (b) Bubble can become unstable and grows explosively (c) Bubble response is stable or unstable depending upon the mobility of contact line. The bubble response and the critical threshold for unstable expansion depends upon the size of nuclei and the amplitude of the pressure forcing. The direct numerical simulations of spherical bubbles subjected to a Gaussian pressure pulse reveal that the finite duration of the pressure pulse imposes an upper bound on bubble size available for explosive growth. Only specific bubble sizes in between these two criterion are active for nucleation. During the unstable bubble growth, the bubble interface and flow near the wall depends upon the complex interplay between the viscous and capillary stresses. We use the Navier-slip model to mimic the moving contact line and to resolve these effects. Upon fixing the Ohnesorge number at values much smaller than unity, we show that the transition to microlayer formation regimes is governed only by capillary numbers (similar to classical Landau–Levich flim experiments). When the capillary number is of the order unity or larger, a liquid microlayer is shown to grow at an asymptotic rate. This regime corresponds to large values of both Reynolds and Weber numbers. Interestingly, the asymptotic growth rate is shown to vary with the cube of equilibrium contact angle. Increasing the Ohnesorge number results in finite Reynolds and finite Weber number effects that suppress the microlayer formation. It form only when the capillary number is much larger then the critical capillary number for the explosive growth corresponding to the Ohnesorge number.

There are several interesting future perspectives of the study on heterogeneous nucleation:

- The finite pulse duration effects for the bubbles attached to wall could provide meaningful insights of the resonance frequencies of bubbles attached to wall, how the bubble shape influences this parameter and its importance on the process of bubble nucleation.
- Finite values of the Reynolds and Weber number significantly alter the microlayer formation dynamics. Although this work already presents some preliminary investigations of

these effects, further studies should be carried out to understand the relative importance of viscosity and surface tension on the process of microlayer formation. Eventually, the experiments reported by Hupfled et. al. [58] may be used for comparison.

- The motion of contact line is another interesting aspect which is not well understood. There are several sophisticated models proposed in the literature (eg. generalized Navier boundary condition, super slip) which can yield $C^2$ continuous velocity field. Changing the contact line modeling can provide interesting cues about the microlayer formation and can further clarify if the asymptotic growth observed in current study is a special case of Navier-slip model or it is a more general phenomenon.

**Heterogeneous bubble nucleation**

- The threshold for heterogeneous nucleation is influenced by the motion of contact line for small bubbles. In general, pinning effects increase the stability of bubbles to negative pressures, although this remains to be a secondary effect in comparison to the classical theory of heterogeneous nucleation.
- When a large negative pressure is imposed for sufficiently large time, numerical simulations with the Navier slip model for contact line indicates that a microlayer is formed and grows at an asymptotic velocity for capillary numbers of order unity and Ohnesorge numbers much smaller than unity.

In chapter 4, we show that the impulsive potential flow theory can be used to discuss the influence of the bubble shape on the dynamic response of collapsing bubbles for sufficiently large Reynolds and Weber numbers. This theory, can be used to discuss the influence of the initial bubble shape on the process of collapse in a general setup. As an example, we present the results obtained for the collapse of spherical cap bubbles. We show that the effective contact angle at the instant of maximum expansion controls the interface acceleration at the beginning of the collapse phase and the jetting direction observed in direct numerical simulations and experiments. When $\alpha > 90$ degrees the potential flow solution at short times shows the appearance of a singularity which causes extremely high accelerations close to the contact line and a change in vorticity direction with respect to the $\alpha \leq 90$ degrees case. In the former case, an unconventional jetting mechanism is observed which is shown to be responsible for the appearance of a vortex dipole traveling in the direction opposite to the wall. We also use direct numerical simulations and the energy conservation equation to characterize the strength of the jets. Particularly, we calculate the residual liquid kinetic energy that remains inside the liquid at the instant of minimum volume which penalizes the maximum gas pressures achieved during the collapse. This penalization effect is directly related to non-spherical effects and becomes increasingly important with increase in pressure driving the collapse. Therefore, the nature of interaction between the bubble and the surrounding medium is strongly influenced by the bubble shape at the instant before collapse, appearing as a critical parameter if one wants to control or model the physical phenomena triggered by the collapse of bubbles attached to a wall.

Some future perspectives of bubble collapse study include:

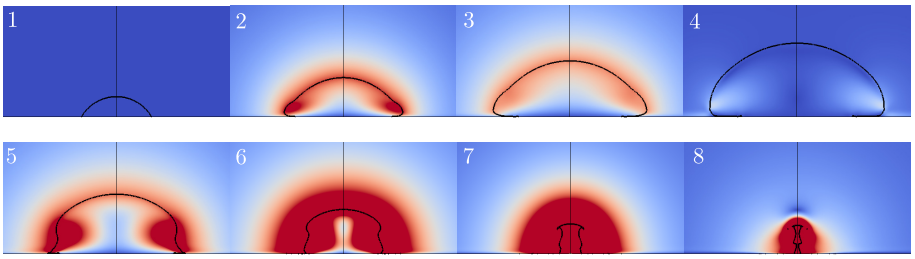


Figure 6.1: Expansion and collapse of bubble in contact with rigid wall. The snapshots 1-8 are numbered in increasing time.

- We have not completely understood the formation of the vortex-dipole from the collapse of bubble with $\alpha > 90$ degrees. This is relevant to understand the conditions of formation of this dipole and characterize its strength.
- The cavitation damage is expected to be linked with the strength of the liquid jets determined by the bubble shapes.
- It could be interesting to establish correlations among the bubble shape, the residual liquid kinetic energy and the peak pressures using the energy conservation equation, and eventually link it with the cavitation damage.
- It is well known that the moving contact line exhibits a force singularity because standard no-slip boundary condition predicts logarithmically diverging shear stresses [135]. Intuitively, there might be a relation between the singularity of potential flow and the force singularity which may inspire new ideas.
- The expansion process can result in bubble shapes that differ from a spherical cap. For instance, in chapter 3 we have shown that a liquid microlayer is formed (see chapter 3). Thus, it could be interesting to understand the effect of microlayer drainage on the jetting and bubble collapse dynamics. One such case is shown in figure 6.1.

**Bubble collapse**

- The bubble shape at the instant of maximum volume is a critical parameter that governs the collapse dynamics and direction of liquid jet.
- The impulse potential flow theory predicts infinite/singular contact line acceleration at short times after the beginning of the collapse for spherical cap bubbles with contact angle larger than 90 degrees. The first term of the series proposed is shown to provide an accurate representation of the full interface evolution.
- The kinetic energy accumulated inside the liquid and liquid compressibility effects penalize the maximum gas pressures during the collapse, being the former more important for low Mach number collapses of non-spherical bubbles.

In chapter 5, we revisit the problem of multiple bubble cavitation using the numerical simulations. In particular, we explain the asymmetry observed during the expansion and collapse of bubbles is related to primary Bjerknes forces induced by the finite length of pressure pulse (controlled by finite speed of sound) effects. The experimental results for the asymmetry are reproduced with numerical simulations at relatively lower values of speed of sounds compared to speed of sound in pure liquid. This can be attributed to the presence of tiny gas bubbles in the liquid bulk which are known to drastically influence the speed of sound in the gas-liquid mixture. These tiny bubbles are expected to be fragmented form the bigger bubbles in the subsequent cavitation experiments.

Some future perspectives of the multi-bubble cavitation studies are:

- The use of an effective medium theory has limitations. While the effective reduction of the speed of sound seems to be sufficient to capture the interactions between the wave and the bubble cluster for systems with a small number of bubbles, this model is probably not very accurate to model the direct interactions between bubbles inside the cluster. Further investigations to the applicability of simplified approaches to systems with clear distinct zones of different concentration seem compulsory.
- It is not clear if the non-linear effects related to the wave propagation are present in the experiments and how these can influence the asymmetry effects. It could be interesting to study the effect of multiple bubbles on the wave propagation to understand the mechanisms that result in lower effective speed of sound.
- One could also study the effect of the mass transfer and ratio of bubble frequency and the characteristic frequency of the pulse on wave propagation. The mass transfer effects and high frequency ratios are known to influence the the wave propagation speeds [184].

**Multibubble cavitaiton**

- The primary Bjerknes forces induced by finite speed of sound effects are responsible for the asymmetry in bubble shapes during the expansion of bubbles attached to wall.
- The asymmetry effects become more relevant when tiny fragments of bubbles remain inside the liquid bulk that can drastically influence speed of sound.

# Bibliography


[1] O. Supponen, D. Obreschkow, M. Tinguely, P. Kobel, N. Dorsaz, and M. Farhat. "Scaling laws for jets of single cavitation bubbles". In: *Journal of Fluid Mechanics* 802 (2016), pp. 263–293.

[2] O. Supponen. *Collapse phenomena of deformed cavitation bubbles*. Tech. rep. EPFL, 2017.

[3] L. A. Crum and R. A. Roy. "Sonoluminescence". In: *Science* 266.5183 (1994), pp. 233–234.

[4] M. P. Brenner, S. Hilgenfeldt, and D. Lohse. "Single-bubble sonoluminescence". In: *Reviews of modern physics* 74.2 (2002), p. 425.

[5] C. D. Ohl, T. Kurz, R. Geisler, O. Lindau, and W. Lauterborn. "Bubble dynamics, shock waves and sonoluminescence". In: *Philosophical Transactions of the Royal Society of London. Series A: Mathematical, Physical and Engineering Sciences* 357.1751 (1999), pp. 269–294.

[6] M. S. Plesset and A. Prosperetti. "Bubble dynamics and cavitation". In: *Annual review of fluid mechanics* 9 (1977), pp. 145–185.

[7] A. D. Maxwell, T.-Y. Wang, C. A. Cain, J. B. Fowlkes, O. A. Sapozhnikov, M. R. Bailey, and Z. Xu. "Cavitation clouds created by shock scattering from bubbles during histotripsy". In: *The Journal of the Acoustical Society of America* 130.4 (2011), pp. 1888–1898.

[8] E. Klaseboer, K. Hung, C. Wang, C. Wang, B. Khoo, P. Boyce, S. Debono, and H. Charlier. "Experimental and numerical investigation of the dynamics of an underwater explosion bubble near a resilient/rigid structure". In: *Journal of Fluid Mechanics* 537 (2005), pp. 387–413.

[9] R. H. Cole and R. Weller. "Underwater explosions". In: *Physics Today* 1.6 (1948), p. 35.

[10] V. Kedrinskii. "Surface effects from an underwater explosion". In: *Journal of Applied Mechanics and Technical Physics* 19.4 (1978), pp. 474–491.

[11] R. C. Gisiner. "Sound and marine seismic surveys". In: *Acoust. Today* 12.4 (2016), pp. 10–18.

[12] D. Lohse. "Bubble puzzles: from fundamentals to applications". In: *Physical review fluids* 3.11 (2018), p. 110504.

[13] S. Li, D. van der Meer, A.-M. Zhang, A. Prosperetti, and D. Lohse. "Modelling large scale airgun-bubble dynamics with highly non-spherical features". In: *International journal of multiphase flow* 122 (2020), p. 103143.

[14] Y. Savchenko. "Supercavitation-problems and perspectives". In: *http://resolver. caltech. edu/-cav2001: lecture. 003* (2001).

[15] X.-w. Zhang, Y.-j. Wei, J.-z. Zhang, W. Cong, and K.-p. Yu. "Experimental research on the shape characters of natural and ventilated supercavitation". In: *Journal of Hydrodynamics, Ser. B* 19.5 (2007), pp. 564–571.

[16] B. Vanek, J. Bokor, G. J. Balas, and R. E. Arndt. "Longitudinal motion control of a high-speed supercavitation vehicle". In: *Journal of Vibration and Control* 13.2 (2007), pp. 159–184.

[17] H. Soyama. "Cavitation peening: A review". In: *Metals* 10.2 (2020), p. 270.

[18] L. Ye, X. Zhu, X. Wei, et al. "Damage characteristics and surface description of near-wall materials subjected to ultrasonic cavitation". In: *Ultrasonics Sonochemistry* 67 (2020), p. 105175.

[19] C. D. Ohl, M. Arora, R. Dijkink, V. Janve, and D. Lohse. "Surface cleaning from laser-induced cavitation bubbles". In: *Applied physics letters* 89.7 (2006), p. 074102.

[20] G. L. Chahine, A. Kapahi, J.-K. Choi, and C.-T. Hsiao. "Modeling of surface cleaning by cavitation bubble dynamics and collapse". In: *Ultrasonics sonochemistry* 29 (2016), pp. 528–549.

[21] K. S. Suslick. "Sonochemistry". In: *science* 247.4949 (1990), pp. 1439–1445.

[22] L. H. Thompson and L. Doraiswamy. "Sonochemistry: science and engineering". In: *Industrial & Engineering Chemistry Research* 38.4 (1999), pp. 1215–1249.

[23] X. Escaler, M. Farhat, F. Avellan, and E. Egusquiza. "Cavitation erosion tests on a 2D hydrofoil using surface-mounted obstacles". In: *Wear* 254.5-6 (2003), pp. 441–449.

[24] M. Dular, B. Bachert, B. Stoffel, and B. Širok. "Relationship between cavitation structures and cavitation damage". In: *Wear* 257.11 (2004), pp. 1176–1184.

[25] M. Dular, B. Stoffel, and B. Širok. "Development of a cavitation erosion model". In: *Wear* 261.5-6 (2006), pp. 642–655.

[26] E. Goncalves and R. F. Patella. "Numerical simulation of cavitating flows with homogeneous models". In: *Computers & Fluids* 38.9 (2009), pp. 1682–1696.

[27] J. Decaix and E. Goncalves. "Compressible effects modeling in turbulent cavitating flows". In: *European Journal of Mechanics-B/Fluids* 39 (2013), pp. 11–31.

[28] E. Goncalves, M. Champagnac, and R. Fortes Patella. "Comparison of numerical solvers for cavitating flows". In: *International Journal of Computational Fluid Dynamics* 24.6 (2010), pp. 201–216.

[29] E. Goncalvès and B. Charrière. "Modelling for isothermal cavitation with a four-equation model". In: *International Journal of Multiphase Flow* 59 (2014), pp. 54–72.

[30] G. N. Kawchuk, J. Fryer, J. L. Jaremko, H. Zeng, L. Rowe, and R. Thompson. "Real-time visualization of joint cavitation". In: *PloS one* 10.4 (2015), e0119470.

[31] J. L. Marsh and S. A. Bentil. "Cerebrospinal fluid cavitation as a mechanism of blast-induced traumatic brain injury: a review of current debates, methods, and findings". In: *Frontiers in neurology* 12 (2021), p. 626393.

[32] K. Ferrara, R. Pollard, M. Borden, et al. "Ultrasound microbubble contrast agents: fundamentals and application to gene and drug delivery". In: *Annual review of biomedical engineering* 9.1 (2007), pp. 415–447.

[33] S. Roovers, T. Segers, G. Lajoinie, J. Deprez, M. Versluis, S. C. De Smedt, and I. Lentacker. "The role of ultrasound-driven microbubble dynamics in drug delivery: From microbubble fundamentals to clinical translation". In: *Langmuir* 35.31 (2019), pp. 10173–10191.

[34] M. Versluis, E. Stride, G. Lajoinie, B. Dollet, and T. Segers. "Ultrasound contrast agent modeling: a review". In: *Ultrasound in medicine & biology* 46.9 (2020), pp. 2117–2144.

[35] E. C. Unger, T. Porter, W. Culp, R. Labell, T. Matsunaga, and R. Zutshi. "Therapeutic applications of lipid-coated microbubbles". In: *Advanced drug delivery reviews* 56.9 (2004), pp. 1291–1314.

[36] P. Prentice, A. Cuschieri, K. Dholakia, M. Prausnitz, and P. Campbell. "Membrane disruption by optically controlled microbubble cavitation". In: *Nature physics* 1.2 (2005), pp. 107–110.

[37] M. Aryal, C. D. Arvanitis, P. M. Alexander, and N. McDannold. "Ultrasound-mediated blood–brain barrier disruption for targeted drug delivery in the central nervous system". In: *Advanced drug delivery reviews* 72 (2014), pp. 94–109.

[38] Y. Zhou, K. Yang, J. Cui, J. Ye, and C. Deng. "Controlled permeation of cell membrane by single bubble acoustic cavitation". In: *Journal of controlled release* 157.1 (2012), pp. 103–111.

[39] R. Illing, J. Kennedy, F. Wu, G. Ter Haar, A. Protheroe, P. Friend, F. Gleeson, D. Cranston, R. Phillips, and M. Middleton. "The safety and feasibility of extracorporeal high-intensity focused ultrasound (HIFU) for the treatment of liver and kidney tumours in a Western population". In: *British journal of cancer* 93.8 (2005), pp. 890–895.

[40] C. Coussios, C. Farny, G. Ter Haar, and R. Roy. "Role of acoustic cavitation in the delivery and monitoring of cancer treatment by high-intensity focused ultrasound (HIFU)". In: *International journal of hyperthermia* 23.2 (2007), pp. 105–120.

[41] V. A. Khokhlova, J. B. Fowlkes, W. W. Roberts, G. R. Schade, Z. Xu, T. D. Khokhlova, T. L. Hall, A. D. Maxwell, Y.-N. Wang, and C. A. Cain. "Histotripsy methods in mechanical disintegration of tissue: Towards clinical applications". In: *International journal of hyperthermia* 31.2 (2015), pp. 145–162.

[42] A. D. Maxwell, C. A. Cain, A. P. Duryea, L. Yuan, H. S. Gurm, and Z. Xu. "Noninvasive thrombolysis using pulsed ultrasound cavitation therapy–histotripsy". In: *Ultrasound in medicine & biology* 35.12 (2009), pp. 1982–1994.

[43] P. Wei, E. J. Cornel, and J. Du. "Ultrasound-responsive polymer-based drug delivery systems". In: *Drug Delivery and Translational Research* 11.4 (2021), pp. 1323–1339.

[44] N. S. Awad, V. Paul, N. M. AlSawaftah, G. Ter Haar, T. M. Allen, W. G. Pitt, and G. A. Husseini. "Ultrasound-responsive nanocarriers in cancer treatment: A review". In: *ACS Pharmacology & Translational Science* 4.2 (2021), pp. 589–612.

[45] A. A. Exner and M. C. Kolios. "Bursting microbubbles: How nanobubble contrast agents can enable the future of medical ultrasound molecular imaging and image-guided therapy". In: *Current Opinion in Colloid & Interface Science* 54 (2021), p. 101463.

[46] B. M. Borkent, S. M. Dammer, H. Schönherr, G. J. Vancso, and D. Lohse. "Superstability of surface nanobubbles". In: *Physical review letters* 98.20 (2007), p. 204502.

[47] J. H. Weijs and D. Lohse. "Why surface nanobubbles live for hours". In: *Physical review letters* 110.5 (2013), p. 054501.

[48] D. Lohse, X. Zhang, et al. "Surface nanobubbles and nanodroplets". In: *Reviews of modern physics* 87.3 (2015), p. 981.

[49] M. Zahiri, S. Taghavi, K. Abnous, S. M. Taghdisi, M. Ramezani, and M. Alibolandi. "Theranostic nanobubbles towards smart nanomedicines". In: *Journal of Controlled Release* 339 (2021), pp. 164–194.

[50] H. Lea-Banks and K. Hynynen. "Sub-millimetre precision of drug delivery in the brain from ultrasound-triggered nanodroplets". In: *Journal of Controlled Release* 338 (2021), pp. 731–741.

[51] F. Maoming, T. Daniel, R. Honaker, and L. Zhenfu. "Nanobubble generation and its application in froth flotation (part I): nanobubble generation and its effects on properties of microbubble and millimeter scale bubble solutions". In: *Mining Science and Technology (China)* 20.1 (2010), pp. 1–19.

[52] Z. Zhou, Z. Xu, J. Finch, J. Masliyah, and R. Chow. "On the role of cavitation in particle collection in flotation–A critical review. II". In: *Minerals Engineering* 22.5 (2009), pp. 419–433.

[53] T. Temesgen, T. T. Bui, M. Han, T.-i. Kim, and H. Park. "Micro and nanobubble technologies as a new horizon for water-treatment techniques: A review". In: *Advances in colloid and interface science* 246 (2017), pp. 40–51.

[54] W. Xiao, G. Xu, and G. Li. "Effect of nanobubble application on performance and structural characteristics of microbial aggregates". In: *Science of The Total Environment* 765 (2021), p. 142725.

[55] N. Bremond, M. Arora, S. M. Dammer, and D. Lohse. "Interaction of cavitation bubbles on a wall". In: *Physics of fluids* 18.12 (2006), p. 121505.

[56] O. Supponen, D. Obreschkow, P. Kobel, M. Tinguely, N. Dorsaz, and M. Farhat. "Shock waves from nonspherical cavitation bubbles". In: *Physical Review Fluids* 2.9 (2017), p. 093601.

[57] S. R. Gonzalez-Avila, F. Denner, and C.-D. Ohl. "The acoustic pressure generated by the cavitation bubble expansion and collapse near a rigid wall". In: *Physics of Fluids* 33.3 (2021), p. 032118.

[58] T. Hupfeld, G. Laurens, S. Merabia, S. Barcikowski, B. Gökce, and D. Amans. "Dynamics of laser-induced cavitation bubbles at a solid–liquid interface in high viscosity and high capillary number regimes". In: *Journal of Applied Physics* 127.4 (2020), p. 044306.

[59] F. Denner, F. Evrard, F. Reuter, S. R. Gonzalez-Avila, B. van Wachem, and C.-D. Ohl. "Predicting laser-induced cavitation near a solid substrate". In: *PAMM* 20.1 (2021), e202000007.

[60] Q. Wang. "Local energy of a bubble system and its loss due to acoustic radiation". In: *Journal of Fluid Mechanics* 797 (2016), pp. 201–230.

[61] R. Hickling and M. S. Plesset. "Collapse and rebound of a spherical bubble in water". In: *The Physics of Fluids* 7.1 (1964), pp. 7–14.

[62] D. Fuster, C. Dopazo, and G. Hauke. "Liquid compressibility effects during the collapse of a single cavitating bubble". In: *The Journal of the Acoustical Society of America* 129.1 (2011), pp. 122–131.

[63] D. F. Gaitan, L. A. Crum, C. C. Church, and R. A. Roy. "Sonoluminescence and bubble dynamics for a single, stable, cavitation bubble". In: *The Journal of the Acoustical Society of America* 91.6 (1992), pp. 3166–3183.

[64] O. Supponen, D. Obreschkow, P. Kobel, and M. Farhat. "Luminescence from cavitation bubbles deformed in uniform pressure gradients". In: *Physical Review E* 96.3 (2017), p. 033114.

[65] O. Supponen, D. Obreschkow, and M. Farhat. "Rebounds of deformed cavitation bubbles". In: *Physical Review Fluids* 3.10 (2018), p. 103604.

[66] J. Bourguille, L. Bergamasco, G. Tahan, D. Fuster, and M. Arrigoni. "Shock propagation effects in multilayer assembly including a liquid phase". In: *Key engineering materials*. Vol. 755. Trans Tech Publ. 2017, pp. 181–189.

[67] L. Rayleigh. "VIII. On the pressure developed in a liquid during the collapse of a spherical cavity". In: *The London, Edinburgh, and Dublin Philosophical Magazine and Journal of Science* 34.200 (1917), pp. 94–98.

[68] E. N. Harvey. "Decompression sickness and bubble formation in blood and tissues". In: *Bulletin of the New York Academy of Medicine* 21.10 (1945), p. 505.

[69] E. N. Harvey. "Decompression Sickness and Bubble Formation in Blood and Tissue, Bull". In: *Anesthesiology: The Journal of the American Society of Anesthesiologists* 7.4 (1946), pp. 457–457.

[70] W. J. Galloway. "An experimental study of acoustically induced cavitation in liquids". In: *The Journal of the Acoustical Society of America* 26.5 (1954), pp. 849–857.

[71] M. Strasberg. "Onset of ultrasonic cavitation in tap water". In: *The Journal of the Acoustical Society of America* 31.2 (1959), pp. 163–176.

[72] M. Greenspan and C. E. Tschiegg. "Radiation-induced acoustic cavitation; apparatus and some results". In: *J. Res. Natl. Bur. Stand., Sect. C* 71 (1967), p. 299.

[73] R. E. Apfel. "The role of impurities in cavitation-threshold determination". In: *The Journal of the Acoustical Society of America* 48.5B (1970), pp. 1179–1186.

[74] L. A. Crum. "Tensile strength of water". In: *Nature* 278.5700 (1979), pp. 148–149.

[75] A. A. Atchley and A. Prosperetti. "The crevice model of bubble nucleation". In: *The Journal of the Acoustical Society of America* 86.3 (1989), pp. 1065–1084.

[76] E. Neppiras and B. Noltingk. "Cavitation produced by ultrasonics: theoretical conditions for the onset of cavitation". In: *Proceedings of the Physical Society. Section B* 64.12 (1951), p. 1032.

[77] C. K. Holland and R. E. Apfel. "An improved theory for the prediction of microcavitation thresholds". In: *IEEE transactions on ultrasonics, ferroelectrics, and frequency control* 36.2 (1989), pp. 204–208.

[78] M. A. Chappell and S. J. Payne. "The effect of cavity geometry on the nucleation of bubbles from cavities". In: *The Journal of the Acoustical Society of America* 121.2 (2007), pp. 853–862.

[79] D. Fuster, K. Pham, and S. Zaleski. "Stability of bubbly liquids and its connection to the process of cavitation inception". In: *Physics of Fluids* 26.4 (2014), p. 042002.

[80] B. M. Borkent, S. Gekle, A. Prosperetti, and D. Lohse. "Nucleation threshold and deactivation mechanisms of nanoscopic cavitation nuclei". In: *Physics of fluids* 21.10 (2009), p. 102003.

[81] R. E. Apfel and C. K. Holland. "Gauging the likelihood of cavitation from short-pulse, low-duty cycle diagnostic ultrasound". In: *Ultrasound in Medicine and Biology* 17.2 (1991), pp. 179–185.

[82] C. K. Holland and R. E. Apfel. "Thresholds for transient cavitation produced by pulsed ultrasound in a controlled nuclei environment". In: *The Journal of the Acoustical Society of America* 88.5 (1990), pp. 2059–2069.

[83] Y. Kurosawa, K. Kato, S. Saito, M. Kubo, T. Uzuka, Y. Fujii, and H. Takahashi. "Basic study of brain injury mechanism caused by cavitation". In: *2009 Annual International Conference of the IEEE Engineering in Medicine and Biology Society*. IEEE. 2009, pp. 7224–7227.

[84] L. Braunstein, S. C. Brüningk, I. Rivens, J. Civale, and G. Ter Haar. "Characterization of Acoustic, Cavitation, and Thermal Properties of Poly (vinyl alcohol) Hydrogels for Use as Therapeutic Ultrasound Tissue Mimics". In: *Ultrasound in Medicine & Biology* 48.6 (2022), pp. 1095–1109.

[85] C. K. Holland, C. X. Deng, R. E. Apfel, J. L. Alderman, L. A. Fernandez, and K. J. Taylor. "Direct evidence of cavitation in vivo from diagnostic ultrasound". In: *Ultrasound in medicine & biology* 22.7 (1996), pp. 917–925.

[86] E. L. Carstensen, S. Gracewski, and D. Dalecki. "The search for cavitation in vivo". In: *Ultrasound in medicine & biology* 26.9 (2000), pp. 1377–1385.

[87] S. Popinet and S. Zaleski. "Bubble collapse near a solid boundary: a numerical study of the influence of viscosity". In: *Journal of fluid mechanics* 464 (2002), pp. 137–163.

[88] T. B. Benjamin and A. T. Ellis. "The Collapse of Cavitation Bubbles and the Pressures thereby Produced against Solid Boundaries". In: *Philosophical Transactions of the Royal Society of London. Series A, Mathematical and Physical Sciences* 260.1110 (1966), pp. 221–240. ISSN: 00804614. URL: http://www.jstor.org/stable/73553.

[89] J. R. Blake. "The Kelvin impulse: application to cavitation bubble dynamics". In: *The ANZIAM Journal* 30.2 (1988), pp. 127–146.

[90] J. R. Blake, D. M. Leppinen, and Q. Wang. "Cavitation and bubble dynamics: the Kelvin impulse and its applications". In: *Interface focus* 5.5 (2015), p. 20150017.

[91] C. F. Naude´ and A. T. Ellis. "On the Mechanism of Cavitation Damage by Nonhemispherical Cavities Collapsing in Contact With a Solid Boundary". In: *Journal of Basic Engineering* 83.4 (Dec. 1961), pp. 648–656. ISSN: 0021-9223.

[92] S. Li, A.-M. Zhang, S. Wang, and R. Han. "Transient interaction between a particle and an attached bubble with an application to cavitation in silt-laden flow". In: *Physics of Fluids* 30.8 (2018), p. 082111.

[93] C. Lechner, W. Lauterborn, M. Koch, and R. Mettin. "Jet formation from bubbles near a solid boundary in a compressible liquid: Numerical study of distance dependence". In: *Physical Review Fluids* 5.9 (2020), p. 093604.

[94] E. Lauer, X. Hu, S. Hickel, and N. A. Adams. "Numerical modelling and investigation of symmetric and asymmetric cavitation bubble dynamics". In: *Computers & Fluids* 69 (2012), pp. 1–19.

[95] P. Koukouvinis, M. Gavaises, A. Georgoulas, and M. Marengo. "Compressible simulations of bubble dynamics with central-upwind schemes". In: *International Journal of Computational Fluid Dynamics* 30.2 (2016), pp. 129–140.

[96] F. Reuter, S. R. Gonzalez-Avila, R. Mettin, and C.-D. Ohl. "Flow fields and vortex dynamics of bubbles collapsing near a solid boundary". In: *Physical Review Fluids* 2.6 (2017), p. 064202.

[97] M. Saini, E. Tanne, M. Arrigoni, S. Zaleski, and D. Fuster. "On the dynamics of a collapsing bubble in contact with a rigid wall". In: *Journal of Fluid Mechanics* 948 (2022), A45.

[98] M. Saini, S. Zaleski, and D. Fuster. "Direct numerical simulation of heterogeneous bubble nucleation". In: *11th International Cavitation Symposium (CAV2021), 2021.* Daejeon, South Korea, May 2021. URL: https://hal.archives-ouvertes.fr/hal-03418953.

[99] D. Fuster and S. Popinet. "An all-Mach method for the simulation of bubble dynamics problems in the presence of surface tension". In: *Journal of Computational Physics* 374 (2018), pp. 752–768.

[100] S. Popinet. "Basilisk". In: *URl: http://basilisk. fr.(accessed: 10.21. 2019)* (2014).

[101] S. Popinet. "A quadtree-adaptive multigrid solver for the Serre–Green–Naghdi equations". In: *Journal of Computational Physics* 302 (2015), pp. 336–358.

[102] C. W. Hirt and B. D. Nichols. "Volume of fluid (VOF) method for the dynamics of free boundaries". In: *Journal of computational physics* 39.1 (1981), pp. 201–225.

[103] Y. Fan, H. Li, and D. Fuster. "Time-delayed interactions on acoustically driven bubbly screens". In: *The Journal of the Acoustical Society of America* 150.6 (2021), pp. 4219–4231.

[104] Y. Saade, M. Jalaal, A. Prosperetti, and D. Lohse. "Crown formation from a cavitating bubble close to a free surface". In: *Journal of fluid mechanics* 926 (2021).

[105] E. Johnsen and T. Colonius. "Implementation of WENO schemes in compressible multicomponent flow problems". In: *Journal of Computational Physics* 219.2 (2006), pp. 715–732.

[106] J. Cocchi, R. Saurel, and J. Loraud. "Treatment of interface problems with Godunov-type schemes". In: *Shock waves* 5.6 (1996), pp. 347–357.

[107] O. Le Métayer and R. Saurel. "The Noble-Abel stiffened-gas equation of state". In: *Physics of Fluids* 28.4 (2016), p. 046102.

[108] F. Denner. "The Gilmore-NASG model to predict single-bubble cavitation in compressible liquids". In: *Ultrasonics Sonochemistry* 70 (2021), p. 105307.

[109] Y. Saade, D. Lohse, and D. Fuster. "A multigrid solver for the coupled pressure-temperature equations in an all-Mach solver with VoF". In: *arXiv preprint arXiv:2206.11294* (2022).

[110] G. Tryggvason, R. Scardovelli, and S. Zaleski. *Direct numerical simulations of gas–liquid multiphase flows*. Cambridge University Press, 2011.

[111] N. Kwatra, J. Su, J. T. Grétarsson, and R. Fedkiw. "A method for avoiding the acoustic time step restriction in compressible flow". In: *Journal of Computational Physics* 228.11 (2009), pp. 4146–4161.

[112] R. Saurel and R. Abgrall. "A multiphase Godunov method for compressible multifluid and multiphase flows". In: *Journal of Computational Physics* 150.2 (1999), pp. 425–467.

[113] F. Denner and B. G. van Wachem. "Numerical modelling of shock-bubble interactions using a pressure-based algorithm without Riemann solvers". In: *Experimental and Computational Multiphase Flow* 1.4 (2019), pp. 271–285.

[114] F. Denner, F. Evrard, and B. van Wachem. "Modeling acoustic cavitation using a pressure-based algorithm for polytropic fluids". In: *Fluids* 5.2 (2020), p. 69.

[115] A. J. Chorin. "Numerical solution of the Navier-Stokes equations". In: *Mathematics of computation* 22.104 (1968), pp. 745–762.

[116] J. B. Bell, P. Colella, and H. M. Glaz. "A second-order projection method for the incompressible Navier-Stokes equations". In: *Journal of computational physics* 85.2 (1989), pp. 257–283.

[117] G. D. Weymouth and D. K.-P. Yue. "Conservative volume-of-fluid method for free-surface simulations on cartesian-grids". In: *Journal of Computational Physics* 229.8 (2010), pp. 2853–2865.

[118] M. Rudman. "A volume-tracking method for incompressible multifluid flows with large density variations". In: *International Journal for numerical methods in fluids* 28.2 (1998), pp. 357–378.

[119] V. Le Chenadec and H. Pitsch. "A monotonicity preserving conservative sharp interface flow solver for high density ratio two-phase flows". In: *Journal of Computational Physics* 249 (2013), pp. 185–203.

[120] J. K. Patel and G. Natarajan. "A novel consistent and well-balanced algorithm for simulations of multiphase flows on unstructured grids". In: *Journal of computational physics* 350 (2017), pp. 207–236.

[121] T. Arrufat, M. Crialesi-Esposito, D. Fuster, Y. Ling, L. Malan, S. Pal, R. Scardovelli, G. Tryggvason, and S. Zaleski. "A mass-momentum consistent, Volume-of-Fluid method for incompressible flow on staggered grids". In: *Computers & Fluids* 215 (2021), p. 104785.

[122] S. Popinet. "Numerical models of surface tension". In: *Annual Review of Fluid Mechanics* 50 (2018), pp. 49–75.

[123] J. U. Brackbill, D. B. Kothe, and C. Zemach. "A continuum method for modeling surface tension". In: *Journal of computational physics* 100.2 (1992), pp. 335–354.

[124] S. J. Cummins, M. M. Francois, and D. B. Kothe. "Estimating curvature from volume fractions". In: *Computers & structures* 83.6-7 (2005), pp. 425–434.

[125] F. Evrard, F. Denner, and B. van Wachem. "Height-function curvature estimation with arbitrary order on non-uniform Cartesian grids". In: *Journal of Computational Physics: X* 7 (2020), p. 100060.

[126] F. Denner and B. G. van Wachem. "Numerical time-step restrictions as a result of capillary waves". In: *Journal of Computational Physics* 285 (2015), pp. 24–40.

[127] F. Denner, F. Evrard, and B. van Wachem. "Breaching the capillary time-step constraint using a coupled VOF method with implicit surface tension". In: *Journal of Computational Physics* 459 (2022), p. 111128.

[128] F. Xiao, R. Akoh, and S. Ii. "Unified formulation for compressible and incompressible flows by using multi-integrated moments II: Multi-dimensional version for compressible and incompressible flows". In: *Journal of Computational Physics* 213.1 (2006), pp. 31–56.

[129] T. Young. "III. An essay on the cohesion of fluids". In: *Philosophical transactions of the royal society of London* 95 (1805), pp. 65–87.

[130] P.-G. De Gennes. "Wetting: statics and dynamics". In: *Reviews of modern physics* 57.3 (1985), p. 827.

[131] D. Bonn, J. Eggers, J. Indekeu, J. Meunier, and E. Rolley. "Wetting and spreading". In: *Reviews of modern physics* 81.2 (2009), p. 739.

[132] J. H. Snoeijer and B. Andreotti. "Moving contact lines: scales, regimes, and dynamical transitions". In: *Annual review of fluid mechanics* 45.1 (2013), pp. 269–292.

[133] O. Voinov. "Hydrodynamics of wetting". In: *Fluid dynamics* 11.5 (1976), pp. 714–721.

[134] T. D. Blake. "The physics of moving wetting lines". In: *Journal of colloid and interface science* 299.1 (2006), pp. 1–13.

[135] C. Huh and L. E. Scriven. "Hydrodynamic model of steady movement of a solid/liquid/fluid contact line". In: *Journal of colloid and interface science* 35.1 (1971), pp. 85–101.

[136] C. Navier. "Mémoire sur les lois du mouvement des fluides". In: *Mémoires de l'Académie Royale des Sciences de l'Institut de France* 6.1823 (1823), pp. 389–440.

[137] A. Guion, S. Afkhami, S. Zaleski, and J. Buongiorno. "Simulations of microlayer formation in nucleate boiling". In: *International Journal of Heat and Mass Transfer* 127 (2018), pp. 1271–1284.

[138] S. Afkhami, J. Buongiorno, A. Guion, S. Popinet, Y. Saade, R. Scardovelli, and S. Zaleski. "Transition in a numerical model of contact line dynamics and forced dewetting". In: *Journal of Computational Physics* 374 (2018), pp. 1061–1093.

[139] C. Kamal, J. E. Sprittles, J. H. Snoeijer, and J. Eggers. "Dynamic drying transition via free-surface cusps". In: *Journal of fluid mechanics* 858 (2019), pp. 760–786.

[140] U. Lācis, P. Johansson, T. Fullana, B. Hess, G. Amberg, S. Bagheri, and S. Zaleski. "Steady moving contact line of water over a no-slip substrate". In: *The European Physical Journal Special Topics* 229.10 (2020), pp. 1897–1921.

[141] S. Afkhami and M. Bussmann. "Height functions for applying contact angles to 2D VOF simulations". In: *International journal for numerical methods in fluids* 57.4 (2008), pp. 453–472.

[142] L. D. Landau and E. Lifshitz. *Fluid Mechanics*. Vol. 6. Pergamon Press, 1959.

[143] N. Committee et al. *Illustrated experiments in fluid mechanics: the NCFMF book of film notes*. Mit Press, 1972.

[144] J.-P. Franc. "The Rayleigh-Plesset equation: a simple and powerful tool to understand various aspects of cavitation". In: *Fluid dynamics of cavitation and cavitating turbopumps*. Springer, 2007, pp. 1–41.

[145] P.-G. De Gennes, F. Brochard-Wyart, D. Quéré, et al. *Capillarity and wetting phenomena: drops, bubbles, pearls, waves*. Vol. 315. Springer, 2004.

[146] A. Urbano, S. Tanguy, G. Huber, and C. Colin. "Direct numerical simulation of nucleate boiling in micro-layer regime". In: *International Journal of Heat and Mass Transfer* 123 (2018), pp. 1128–1137.

[147] G. K. Sinha, S. Narayan, and A. Srivastava. "Microlayer dynamics during the growth process of a single vapour bubble under subcooled flow boiling conditions". In: *Journal of Fluid Mechanics* 931 (2022).

[148] M. Fricke, M. Köhne, and D. Bothe. "On the kinematics of contact line motion". In: *PAMM* 18.1 (2018), e201800451.

[149] M. Fricke, M. Köhne, and D. Bothe. "A kinematic evolution equation for the dynamic contact angle and some consequences". In: *Physica D: Nonlinear Phenomena* 394 (2019), pp. 26–43.

[150] U. Lācis, M. Pellegrino, J. Sundin, G. Amberg, S. Zaleski, B. Hess, and S. Bagheri. "Nanoscale sheared droplet: volume-of-fluid, phase-field and no-slip molecular dynamics". In: *Journal of Fluid Mechanics* 940 (2022).

[151] S. D. Wilson. "The drag-out problem in film coating theory". In: *Journal of Engineering Mathematics* 16.3 (1982), pp. 209–221.

[152] L. Hocking. "The spreading of a thin drop by gravity and capillarity". In: *The Quarterly Journal of Mechanics and Applied Mathematics* 36.1 (1983), pp. 55–69.

[153] H. Schlichting and K. Gersten. *Boundary-layer theory*. Springer, 2016.

[154] M. Cooper and A. Lloyd. "The microlayer in nucleate pool boiling". In: *International Journal of Heat and Mass Transfer* 12.8 (1969), pp. 895–913.

[155] L. Landau and B. Levich. "Dragging of a liquid by a moving plate". In: *Dynamics of curved fronts*. Elsevier, 1988, pp. 141–153.

[156] B. Derjaguin. "On the thickness of a layer of liquid remaining on the walls of vessels after their emptying, and the theory of the application of photoemulsion after coating on the cine film (presented by academician AN Frumkin on July 28, 1942)". In: *Progress in Surface Science* 43.1-4 (1993), pp. 129–133.

[157] J. Eggers. "Hydrodynamic theory of forced dewetting". In: *Physical review letters* 93.9 (2004), p. 094502.

[158] L. Bureš and Y. Sato. "Comprehensive simulations of boiling with a resolved microlayer: validation and sensitivity study". In: *Journal of Fluid Mechanics* 933 (2022).

[159] A. N. Guion. "Modeling and simulation of liquid microlayer formation and evaporation in nucleate boiling using computational fluid dynamics". PhD thesis. Massachusetts Institute of Technology, 2017.

[160] C. K. Batchelor and G. Batchelor. *An introduction to fluid dynamics*. Cambridge university press, 2000.

[161] A. Antkowiak, N. Bremond, S. Le Dizes, and E. Villermaux. "Short-term dynamics of a density interface following an impact". In: *Journal of Fluid Mechanics* 577 (2007), pp. 241–250.

[162] P. G. Saffman. *Vortex dynamics*. Cambridge university press, 1995.

[163] S. B. Pope. *Turbulent flows*. 2001.

[164] M. Dauge. *Elliptic boundary value problems on corner domains: smoothness and asymptotics of solutions*. Vol. 1341. Springer, 2006.

[165] H. Blum and M. Dobrowolski. "On finite element methods for elliptic equations on domains with corners". In: *Computing* 28.1 (1982), pp. 53–63.

[166] K. Steger. "Corner singularities of solutions of the potential equation in three dimensions". In: *Mathematical Modelling and Simulation of Electrical Circuits and Semiconductor Devices*. Springer, 1990, pp. 283–297.

[167] R. D. Deegan, O. Bakajin, T. F. Dupont, G. Huber, S. R. Nagel, and T. A. Witten. "Capillary flow as the cause of ring stains from dried liquid drops". In: *Nature* 389.6653 (1997), pp. 827–829.

[168] Z. C. Li and T. T. Lu. "Singularities and treatments of elliptic boundary value problems". In: *Mathematical and Computer Modelling* 31.8-9 (2000), pp. 97–145.

[169] J. Philippi, A. Antkowiak, and P.-Y. Lagrée. "A pressure impulse theory for hemispherical liquid impact problems". In: *European Journal of Mechanics-B/Fluids* 67 (2018), pp. 417–426.

[170] Z. Yosibash, S. Shannon, M. Dauge, and M. Costabel. "Circular edge singularities for the Laplace equation and the elasticity system in 3-D domains". In: *International journal of fracture* 168.1 (2011), pp. 31–52.

[171] C. E. Brennen. *Cavitation and bubble dynamics*. Cambridge University Press, 2014.

[172] M. Brøns, M. C. Thompson, T. Leweke, and K. Hourigan. "Vorticity generation and conservation for two-dimensional interfaces and boundaries". In: *Journal of fluid mechanics* 758 (2014), pp. 63–93.

[173] D. Fuster and M. Rossi. "Vortex-interface interactions in two-dimensional flows". In: *International Journal of Multiphase Flow* 143 (2021), p. 103757.

[174] F. Reuter, Q. Zeng, and C.-D. Ohl. "The Rayleigh prolongation factor at small bubble to wall stand-off distances". In: *Journal of Fluid Mechanics* 944 (2022).

[175] G. Tahan, M. Arrigoni, P. Bidaud, L. Videau, and D. Thévenet. "Evolution of failure pattern by laser induced shockwave within an adhesive bond". In: *Optics & Laser Technology* 129 (2020), p. 106224.

[176] N. Bremond, M. Arora, C.-D. Ohl, and D. Lohse. "Controlled Multibubble Surface Cavitation". In: *Phys. Rev. Lett.* 96 (22 June 2006), p. 224501. DOI: 10.1103/PhysRevLett.96.224501. URL: https://link.aps.org/doi/10.1103/PhysRevLett.96.224501.

[177] V. Bjerknes. *Fields of force: supplementary lectures, applications to meteorology; a course of lectures in mathematical physics delivered December 1 to 23, 1905*. 1. Columbia University Press, 1906.

[178] T. Leighton, A. Walton, and M. Pickworth. "Primary bjerknes forces". In: *European Journal of Physics* 11.1 (1990), p. 47.

[179] U. Parlitz, R. Mettin, S. Luther, I. Akhatov, M. Voss, and W. Lauterborn. "Spatio–temporal dynamics of acoustic cavitation bubble clouds". In: *Philosophical Transactions of the Royal Society of London. Series A: Mathematical, Physical and Engineering Sciences* 357.1751 (1999), pp. 313–334.

[180] T. Leighton. *The acoustic bubble*. Academic press, 2012.

[181] A. A. Doinikov. "Bjerknes forces and translational bubble dynamics". In: *Bubble and particle dynamics in acoustic fields: modern trends and applications* 661 (2005), pp. 95–143.

[182] M. S. Plesset and T. Mitchell. "On the stability of the spherical shape of a vapor cavity in a liquid". In: *Quarterly of Applied Mathematics* 13.4 (1956), pp. 419–430.

[183] G. Costigan and P. Whalley. "Measurements of the speed of sound in air-water flows". In: *Chemical Engineering Journal* 66.2 (1997), pp. 131–135.

[184] D. Fuster and F. Montel. "Mass transfer effects on linear wave propagation in diluted bubbly liquids". In: *Journal of Fluid Mechanics* 779 (2015), pp. 598–621.